Cratonic Upper-mantle Beneath the Central Slave Province

by

Jason Millard MacKenzie
B.Sc., Acadia University, 1996

A Thesis Submitted in Partial Fulfillment of the
Requirements for the Degree of

MASTER OF SCIENCE

in the School of Earth and Ocean Sciences

We accept this thesis as conforming
to the required standard

[redacted]

Dr. D. Canil, Supervisor (School of Earth and Ocean Sciences)

[redacted]

Dr. K. Gillis, Internal Member (School of Earth and Ocean Sciences)

[redacted]

Dr. G. Spence, Internal Member (School of Earth and Ocean Sciences)

[redacted]

Dr. R. Hyndman, Outside Member (Pacific Geoscience Centre, Geological Survey of Canada and Department of Physics and Astronomy)

[redacted]

Dr. J.K. Russell, External Examiner (Dept. of Earth and Ocean Sciences, University of British Columbia)

University of Victoria

Supervisor: Dr. Dante Canil

ABSTRACT

The composition of the upper mantle lithosphere beneath the Archean Slave Province has been estimated by combining mineral chemical and petrographic data from mantle xenoliths entrained in the Torrie kimberlite pipe located in the central Slave Province. Coarse- and granuloblastic-, and porphyroclastic- textured peridotite xenoliths are the dominate rock type and yield equilibration temperatures ranging between 850-1350°C. Thermobarometry requires a minimum lithospheric thickness of approximately 180 km during the late Cretaceous-early Paleocene. The distribution of pressures and temperatures of equilibration for the xenoliths lie on a calculated 42 mWm^{-2} paleogeotherm, ~11 mWm^{-2} lower than the present heat flow measured at Yellowknife. Some samples show a complex thermal evolution. The higher heat flow measured at Yellowknife is a result of highly radiogenic rocks near the surface. The Mg# [Mg/(Mg+Fe)] of olivine in peridotites varies from 0.906-0.938 with an average of 0.920. The Torrie xenolith suite show variable degrees of serpentinization and/or carbonation with the rim compositions of many clinopyroxene grains showing Ca enrichment although overall, the xenoliths are homogeneous at all scales. The Torrie xenoliths are rich in orthopyroxene similar to other low temperature (<1100°C) peridotites from southern Africa. Estimates of bulk rock composition based on mineral chemical and modal data reveal a negative correlation between Si and Fe, similar to peridotite xenoliths from Udachnaya (Boyd et al., 1997). Similarities between xenoliths from the Torrie kimberlite and comparable xenoliths from locations around the globe suggest that the lithosphere beneath the Slave craton has experienced a evolution similar to other cratons globally.

Examiners:

[redacted]

Dr. D. Canil, Supervisor (School of Earth and Ocean Sciences)

[redacted]

Dr. K. Gillis, Internal Member (School of Earth and Ocean Sciences)

[redacted]

Dr. G. Spence, Internal Member (School of Earth and Ocean Sciences)

[redacted]

Dr. R. Hyndman, Outside Member (Pacific Geoscience Centre, Geological Survey of Canada and Department of Physics and Astronomy)

[redacted]

Dr. J.K. Russell, External Examiner (Dept. Of Earth and Ocean Sciences, University of British Columbia)

TABLE OF CONTENTS

Abstract....................ii

Table of Contents....................iv

List of Tables....................vii

List of Figures.................... viii

Acknowledgements....................x

CHAPTER 1 INTRODUCTION

1.1 Xenoliths.................... 1

1.2 Kimberlites.................... 2

1.3 Cratons.................... 3

1.4 The Slave craton.................... 6

1.5 Kimberlites and diamond exploration in the Slave craton.................... 6

1.6 Thesis outline.................... 9

CHAPTER 2 XENOLITH PETROGRAPHY

2.1 Host kimberlite....................10

2.2 Xenolith Petrography....................11

2.3 Alteration.................... 19

2.4 Modal analysis....................19

2.5 Summary.................... 25

CHAPTER 3 MINERAL CHEMISTRY

3.1 Analytical methods....................26

3.2 Mineral chemistry.................... 27

  3.2.1 Olivine.................... 27

3.2.2 Garnet 29

3.2.3 Orthopyroxene 30

3.2.4 Clinopyroxene 30

3.2.5 Spinel 30

3.3 Summary 33

CHAPTER 4 GEOTHERMOBAROMETRY

4.1 Geothermobarometry 34

4.2 Methods 35

4.3 Pressures and temperatures 39

4.4 Summary 51

CHAPTER 5 THERMAL STRUCTURE

5.1 Geotherms and surface heat flow 54

5.2 Paleogeotherm for the central Slave 57

5.3 Lithospheric thickness of the central Slave 64

5.4 Summary 65

CHAPTER 6 ORIGIN OF THE SLAVE MANTLE ROOT

6.1 Existing models 67

6.2 Evidence from the Torrie suite 71

6.3 Shallow subduction in the Slave craton 77

6.4 Summary 79

CHAPTER 7 CONCLUSIONS

7.1 Thermal state 80

7.2 Craton development 81

7.3 Future work 83

REFERENCES 84

APPENDIX 1 XENOLITH PETROGRAPHY...................................... 91

APPENDIX 2 MINERAL CHEMISTRY.. 94

APPENDIX 3 CALCULATED P-T SOLUTIONS................................ 107

LIST OF TABLES

Table 2.1 Calculated modes for the Torrie xenoliths................................. 22

Table 2.2 Comparison of modes from Torrie, Southern Africa, and Siberia...... 25

Table 4.1 Error estimates for geobarometers...38

Table 4.2 Summary of P-T estimates for the Torrie peridotites.................... 49

LIST OF FIGURES

Figure 1.1 Tectonic map of the Slave Province.................................... 7
Figure 1.2 Distribution of kimberlites in the Slave Province........................ 8
Figure 2.1 Coarse peridotite in crossed polars.................................... 13
Figure 2.2 Porphyroclastic peridotite in plane polarized light....................... 14
Figure 2.3 Kelyphite rim inplane polarized light.................................... 15
Figure 2.4 Olivine inclusion in garnet in crossed polars............................ 16
Figure 2.5 Coarse phlogopite in crossed polars.................................... 18
Figure 2.6 Serpentine replacing primary orthopyroxene in crossed polars..........21
Figure 2.7 Modal olivine and orthopyroxene vs. % alteration...................... 23
Figure 2.8 Modal garnet vs. pyroxene.. 24
Figure 3.1 Olivine Mg# histogram.. 28
Figure 3.2 CaO vs. Cr_2O_3 for garnets from Torrie.................................. 29
Figure 3.3 Orthopyroxene Ca/Ca+Mg histogram.................................... 31
Figure 3.4 Clinopyroxene Ca/Ca+Mg histogram....................................32
Figure 4.1 Example calculation for P_{INT}..40
Figure 4.2 ΔT_{ONEILL} vs. T_{BKN}..41
Figure 4.3 ΔT_{KROGH} vs. T_{BKN}.. 42
Figure 4.4 ΔT_{HARLEY} vs. T_{BKN}... 43
Figure 4.5 $\Delta T_{Ca\ in\ opx}$ vs. T_{BKN}... 44
Figure 4.6 $\Delta T_{core\text{-}rim}$ vs. T_{BKN}...46
Figure 4.7 $\Delta P_{core\text{-}rim}$ vs. P_{BKN}...47
Figure 4.8 Histogram of calculated temperatures.....................................50
Figure 4.9 P-T plot for the Torrie peridotites.. 52
Figure 4.10 P-T plot using different geothermobarometers...........................53
Figure 5.1 Torrie P-T plot and the 40 mWm^{-2} geotherm........................... 56

Figure 5.2 Torrie P-T plot and 42 mWm^{-2} calculated geotherms.................... 59

Figure 5.3 Torrie P-T plot and 53 mWm^{-2} calculated geotherms......................61

Figure 5.4 P-T plot for xenolith suites from the Slave craton........................ 63

Figure 6.1 Plume model..69

Figure 6.2 Shallow subduction model..70

Figure 6.3 Olivine Mg# vs. Modal olivine...72

Figure 6.4 Bulk FeO vs. SiO_2 for the Torrie peridotites.............................. 74

Figure 6.5 NiO (olivine) vs. modal orthopyroxene....................................76

Figure 6.6 Schematic cross section of Slave and younger terranes to west..........78

Figure 7.1 Tectonic development of the Slave craton..................................82

ACKNOWLEDGEMENTS

First and foremost I must thank Dr. Dante Canil for his continued support, patience and guidence throughout the course of this work. He has not only been an emmense source of information and inspiration but a great friend as well; Thank you Dante. I would also like to thank Lithoprobe for funding this project and Tanqueray Resources for providing samples. Much appreciated analytical asistance was provided by Dr. Mati Raudsepp at UBC and Paul Wagner at UofA. Thanks to Pa and Mary and all my friends in Vancouver who put me up while I was analyzing samples at UBC. Thanks to Jody and Sheldon for helping me make sense of thermodynamics. Thanks to Dr. A. Fanning (Gus) who helped me see what I was capable of while remembering where I came from. Thanks to Mark for his help with the intergration of e^x, and Neil, Brent and Scott for help with everything from computers to golf. Finally, I especially would like to thank Samantha Hatfield who gave up everything for us to come to Victoria and for her unconditional love and confindence in me the value of which are priceless.

CHAPTER 1

INTRODUCTION

1.1 Xenoliths

Xenoliths are accidental fragments of wall rock that become incorporated into magma. Depending on the nature of the xenolith and host magma, xenoliths in an ascending magma are transported to the surface preserving the characteristics of the source region from which they were derived. In particular, xenoliths hosted in alkaline magmas are especially useful samples parts of the Earth's crust and deep mantle. Xenoliths provide information regarding the composition, thickness, lithostratigraphy and physical properties of the crust and upper mantle lithosphere through which the host magma has risen. In some cases, xenolith studies also can provide information with which seismological studies can be compared.

The nature and architecture of the Earth's lithosphere can be delineated using several methods which reflect differing scales of observation inherent to each technique. They include: 1) continental and oceanic deep drilling, 2) studies of deep-seated rocks exhumed to the surface by tectonic processes , 3) xenolith studies and 4) seismic studies. All of these methods have their limitations but, collectively, give us a more complete picture of the Earth's internal structure and composition. Studies of deep-seated rocks and deep drilling initiatives have greatly expanded our understanding of the composition and structure of both oceanic and continental crust but these studies are restricted to depths approaching < 40 and 9 km respectively (Rudnick, 1990; www.icdp.gfz.potsdam.de).

Seismic studies have promoted our understanding of Earth's internal structure at scales ranging from <1 to thousands of kilometers. The most detailed observations on the Earth's lithosphere are preserved in xenoliths. For this reason, xenolith studies are essential in understanding details and processes pertaining to lithospheric growth, stabilization and destruction.

1.2 Kimberlites

A major source of crustal and mantle xenoliths are kimberlites. Kimberlites are "a clan of volatile-rich (dominantly CO_2) potassic ultrabasic rocks commonly exhibiting an inequigranular texture resulting in the presence of macro- and megacrysts set in a fine-grained matrix" (Mitchell, 1995). The macro/megacryst assemblage consists of rounded grains of ilmenite, pyrope, olivine, diopside, enstatite, and chromite whereas the matrix assemblage consists of primary olivine and/or phlogopite, perovskite, spinel, diopside, monticellite, apatite, calcite, and late stage serpentine (Mitchell, 1995). Kimberlites can be sub-divided, based on the modal proportion of mica, into "basaltic" (< 5% mica in the phenocryst assemblage, <50 % mica in groundmass) and "lamprophyric" (> 5% mica phenocrysts in a groundmass containing >50 % mica) varieties , but Mitchell (1995) advocates a classification scheme using mineralogical "qualifiers" for the term kimberlite based on the modal proportions of phlogopite, serpentine, calcite, monticellite, and diopside.

Kimberlites occur in diverse tectonic environments from Archean cratonic areas (on-craton) to Phanerozoic mobile belts (off-craton) (Mitchell, 1995). Generally, diamondiferous kimberlites occur in on-craton settings, an observation known as "Clifford's rule" (Mitchell, 1995). The ages of kimberlite magmatism vary globally. Mitchell (1995) noted that while the majority of on-craton kimberlites in southern Africa range in emplacement age from 100-80 Ma, three other significantly older periods of kimberlite magmatism exist including 1600, 1200 and 500 Ma. Additionally, Mitchell

(1995) noted that many kimberlites occurring in mobile belts surrounding the Kaapvaal craton yield consistently younger ages from 54-72 Ma. Kimberlites (on-craton) from the Slave Province located in Canada's Northwest Territories range in age from Cambrian to Early Paleocene (Heaman et al., 1997; Nassichuk and McIntyre, 1995).

The exact composition of the kimberlite source region is ambiguous and there may very well not be a unique solution. The petrogenesis of kimberlites is currently thought to be attributable to partial melting of metasomatized, carbonated, lherzolitic asthenospheric mantle at pressures of 5-7 GPa (150-200 km) (Mitchell, 1995). Other models of kimberlite petrogenesis include: 1) volatile fluxing, 2) partial melting of a magnesite peridotite source, 3) transition zone melting, 4) redox melting, 5) partial melting of lithosphere, and 6) hot-spot melting (Mitchell,1995)

Because of their deep-seated origin, kimberlites act as natural ‘boreholes' which randomly sample parts of the mantle and crust during ascent and emplacement. Alkaline basalts and nephelinites are also a source for mantle and crustal xenoliths which sample a depth extent much shallower than that of kimberlites. As such, kimberlite-hosted xenoliths provide direct evidence pertaining to the composition of the deeper mantle, in particular, deep cratonic mantle. Kimberlites are also the primary host rock for diamonds which are carried to the surface as xenocrysts in much the same manner as xenoliths are sampled.

1.3 Cratons

Cratons are continental areas which have not been significantly stretched or shortened for a prolonged period of time, typically since the Archean (Hoffman, 1990). Pollack (1986) indicates that the stability of cratons is displayed in at least three ways: 1) resistance to internal deformation, 2) a paucity of magmatism and 3) maintenance of freeboard above sea level. Seismic studies show that many Archean cratons, including the North American craton (Hoffman, 1990), have anomalous “root zones” characterized by anomalously fast seismic shear velocities extending to depths greater than 200 km

(Hoffman, 1990). These “root zones" underlie Archean continental crust and represent the part of the lithosphere hereafter referred to as cratonic mantle. Oceanic crust is also underlain by mantle lithosphere (hereafter called oceanic mantle) but the thickness of this layer is ~100 km less in the oldest oceanic lithosphere than that which is observed in most Archean cratons (Kearey and Vine, 1990). For the purposes of this paper, the term "lithosphere" is defined as the crust and the portion of upper mantle mechanically coupled to the crust through which heat is transferred conductively (Rudnick et al., 1998).

Most kimberlite-hosted mantle samples occur as macro/mega xenocrysts of olivine (ol), orthopyroxene (opx), clinopyroxene (cpx), garnet (gt) and spinel (sp). Alternatively, mantle xenoliths are dominated by peridotite (ol ± opx ± cpx ± gt ± sp) and, to a much lesser extent , eclogite (gt+ opx ± cpx), pyroxenite (opx ± cpx) and dunite (>90 % ol). Estimated proportions of kimberlite-borne mantle xenoliths from southern Africa and Siberia indicate that more than 80% of the xenoliths are peridotitic which include both spinel and/or garnet bearing harzburgites and lherzolites (Boyd et al., 1997).

Primitive (fertile) upper-mantle is approximated by the composition of the hypothetical model lithology termed “pyrolite” (Ringwood, 1991), consisting of ~45 % SiO_2 with a bulk Mg # (Mg/Mg+Fe) = 0.89. Mineralogically, “pyrolite” may crystallize in four distinct mineral assemblages depending on the pressure, temperature (P-T) and oxidation (f_{H2O}) conditions during crystallization (Ringwood, 1991). Recently, Angel (1997) has suggested that that a pyrolitic upper mantle would contain ~60 % olivine. Cratonic mantle xenoliths are unlike “pyrolite” in that they are depleted in magmaphile elements (Fe, Al, Na, and Ca) reflecting removal of a melt component, and are also enriched in modal orthopyroxene (Boyd, 1987).

The origin of cratonic upper mantle has been a topic of debate for several years and current hypotheses have mostly been based on studies of kimberlite-hosted xenoliths from traditional diamond producing areas in southern Africa and Siberia (Boyd, 1989; Boyd et al., 1997), with limited studies of peridotite xenoliths from other kimberlite provinces elsewhere in Canada (i.e. Kjarsgaard and Peterson, 1992; Kopylova et al., 1997; Schmidberger and Francis, submitted), Wyoming (i.e. Eggler et al., 1987), India (Ganguly, 1995), Tanzania (Rudnick et al., 1994) and Botswana (Stiefenhofer et al., 1997). Seismic (ie. Grand, 1987) and experimental studies (i.e. Canil, 1991; Walter, 1998) have also been important in developing models examining the origins of cratonic peridotite.

There are essentially two models proposed for the origin of cratonic upper mantle. One model views cratonic mantle as the high-pressure residues remaining after the extraction of komatiitic and basaltic liquids from the primitive Archean mantle. This model is supported by peridotite melting experiments (Walter, 1998). This process is expected to have been more prevalent during the Archean when lithospheric temperatures were likely higher (Hoffman, 1990). This is because the average half lives of heat producing elements (U, Th, K) are such that these elements would produce approximately twice as much heat during the Archean at their current concentrations (R. Hyndman, pers. comm. 1998). In this model, eclogites are expected to represent either high-pressure cumulates or metamorphosed oceanic crust that has since been accreted to the base of the existing lithosphere (Richardson et al., 1990). The second model is based on the idea that peridotites and eclogites are products of recycled, metamorphosed oceanic lithosphere, and that cratonic mantle grew through tectonic stacking of both metaperidotite and metabasalt (eclogite) (Hart et al., 1997). This model is mainly supported by trace element data which demonstrate overlap of some trace element fields between cratonic peridotites and eclogites with fields characteristic of mid-ocean ridge basalts (MORB's) (i.e. Hart et al., 1997).

The depth extent, age and thermal state of cratonic lithosphere can also be understood through xenolith studies. Using equilibrium thermobarometry, pressures and temperatures (P-T's) of equilibration for the xenoliths can be derived from which lithospheric thickness, stratigraphy, and thermal state may be interpreted. Additionally, zoning and disequilibrium in the mineral assemblages within the xenoliths may record thermal perturbations and mantle metasomatism. Characterizing the composition, thickness, thermal structure and age of cratonic upper mantle is essential in understanding the processes involved in the formation and stabilization of cratonic lithosphere.

1.4 The Slave craton

The Slave Province is an Archean craton located in the Northwest Territories, Canada (fig. 1.1) and contains the oldest rocks known on Earth; the 3.96 Ga Acasta gneiss (Bowring et al., 1990). In comparison with other Archean cratons, the surface area of the Slave craton is small ,~210 000 km^2 (Isachsen and Bowring, 1994). Additionally, the Slave Province contains a high proportion of supracrustal metasedimentary and felsic volcanic rocks, as well as a higher proportion of more evolved K-rich granitoids, and a limited occurrence of ultramafic igneous rocks (Padgham and Fyson, 1992). The geology of the Slave craton contains parts of three major lithotectonic units composed of: 1) recrystallized, migmatitic and granitoid rocks, 2) metamorphosed greywacke/mudstone divided by thin, discontinuous volcanic belts (Padgham and Fyson, 1992; Thompson et al., 1996) and 3) late, post-tectonic, K-rich plutonic rocks (Padgham and Fyson, 1992). The unique crustal features that distinguish the Slave craton from other Archean cratons may indicate that the Slave craton has evolved somewhat differently from other Archean cratons, and that the underlying mantle may also have shared a unique evolution.

1.5 Kimberlites and diamond exploration in the Slave craton

The discovery of diamondiferous kimberlites in the Slave craton in 1991 sparked the largest staking rush in North American history. Presently, more than 80 % of the craton is staked and more than 150 kimberlites have been discovered that range in age from Cambrian to Tertiary (Pell, 1997; Kopylova et al., 1998) (fig 1.2).

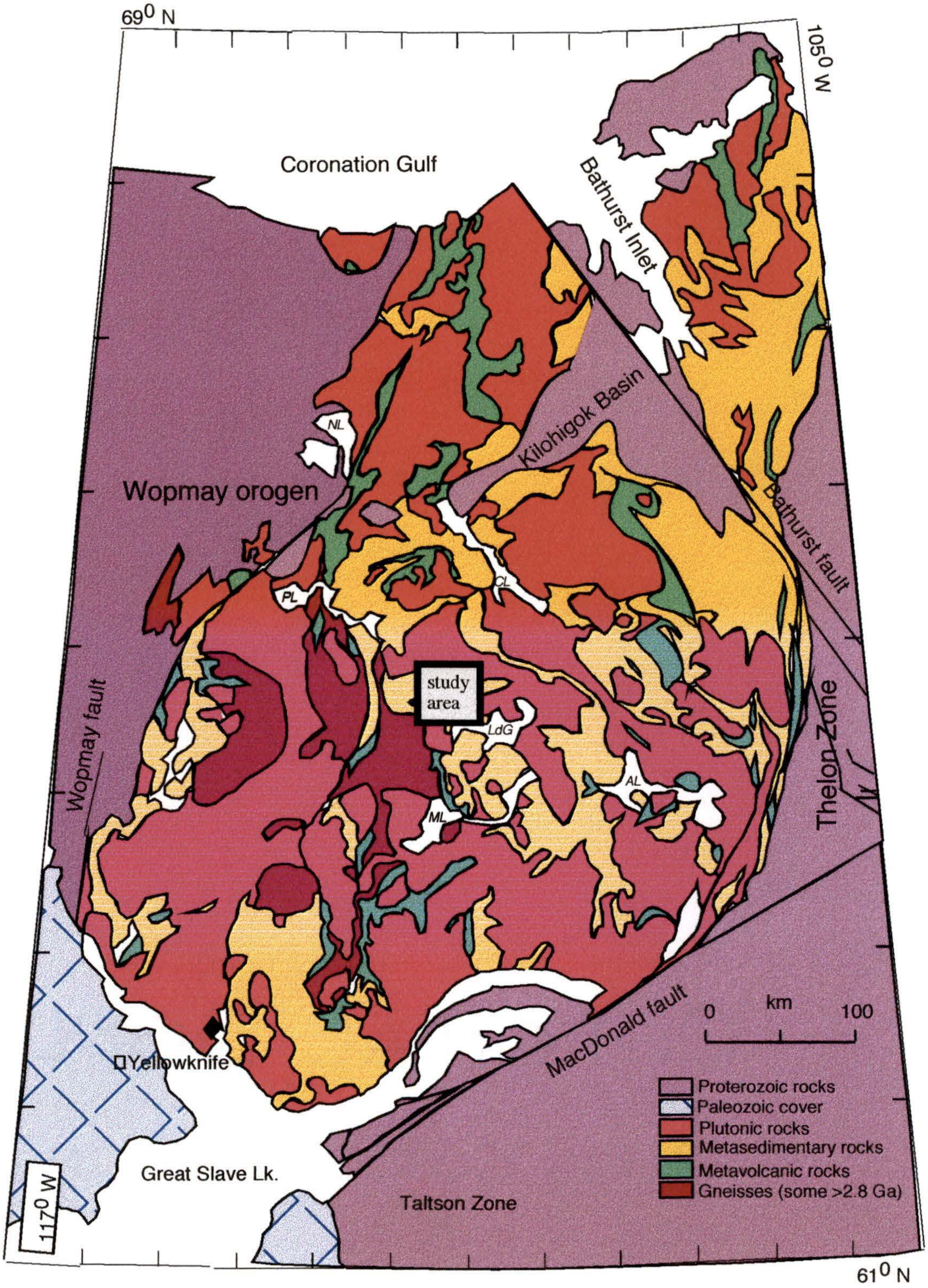

Figure 1.1: Tectonic map of the Archean Slave Province located in the Northwest Territories Canada (after Pell, 1997). LdG - Lac de Gras, Al - Aylmer Lk., ML - McKay Lk., PL - Point Lk.

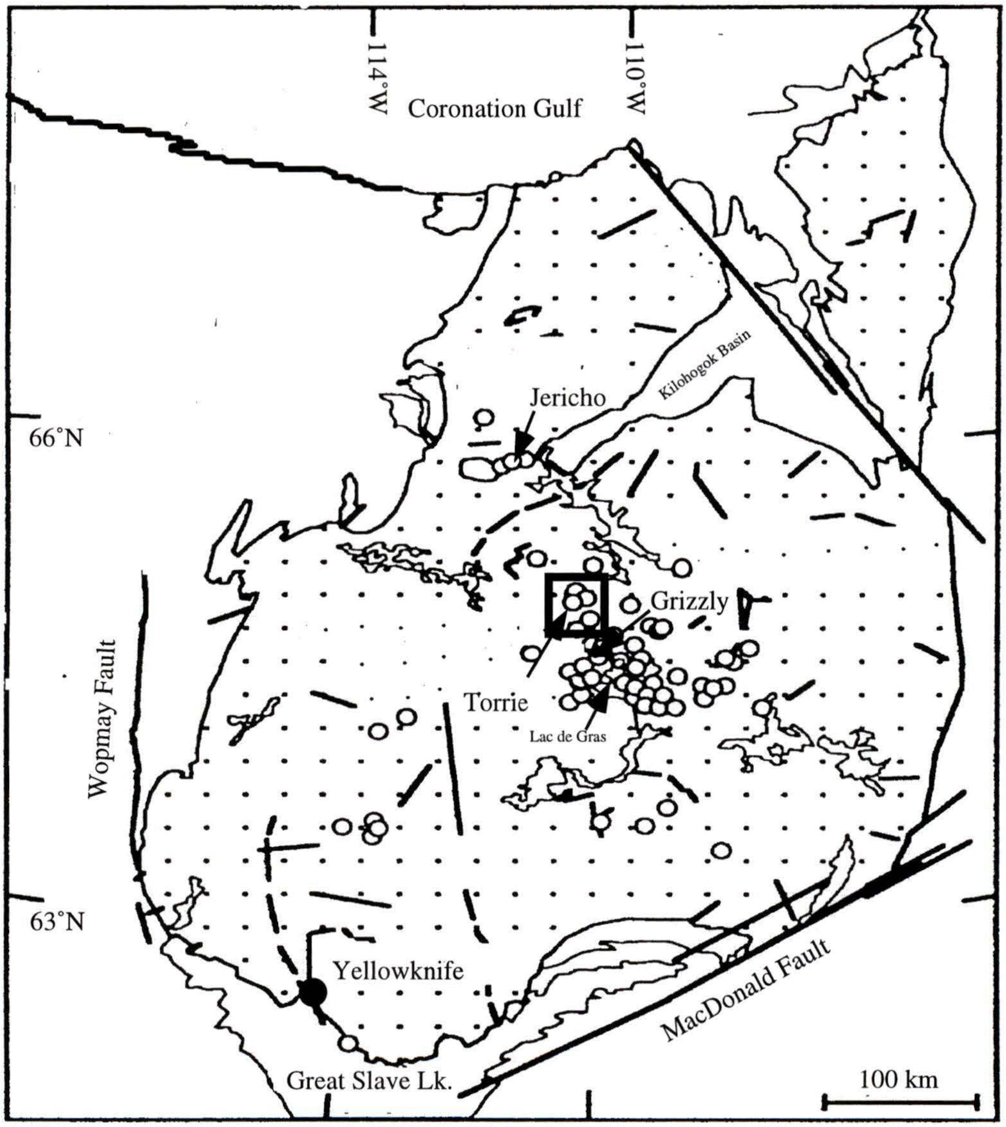

Figure 1.2: Distribution of kimberlites (open circles) across the Archean Slave Province (after Kopylova et al., 1998; Pell, 1997)

Canada's first diamond mine (operated by BHP) is expected to go into production in late 1998 and another (operated by Diavik) is in the final stages of feasibility and environmental evaluation. Scientific investigation into Slave kimberlites and their xenoliths is in its infancy although as work continues, their petrology, ages, and diamond potential will become better characterized.

1.6 Thesis outline

This thesis describes mantle xenoliths from the Torrie kimberlite pipe, located in the central Slave craton (figs 1.1, 1.2). The Torrie pipe intrudes a late Archean, K-rich, granitoid pluton and is dated by palynology as late Cretaceous-early Paleocene (W.W. Nassichuk, pers. comm., 1998; Nassichuk and McIntyre, 1995), similar to other pipes in the Lac de Gras cluster (Davis and Kjarsgaard, 1997). The goals of the thesis are to 1) characterize the mineralogical and chemical nature of the mantle lithosphere underlying the central Slave craton. 2) Using the xenoliths we are also able to model the thermal state and thickness of the Slave lithosphere and identify thermal and/or metasomatic perturbations and 3) compare the results to mantle lithosphere from other cratons globally.

CHAPTER 2

XENOLITH PETROGRAPHY

2.1 Host kimberlite

The samples used in this study were recovered from drill core from the Torrie kimberlite pipe (65°00'N, 110°59'W), located ~60 km northwest of Lac De Gras (LdG) in the Slave Province, Northwest Territories, Canada (figure 1.2). This pipe is a fresh, diamondiferous, organic-rich, basaltic kimberlite containing both authogenic and xenocrystic olivine, clinopyroxene, garnet, orthopyroxene and ilmenite in a fine grained matrix of optically unresolvable material rich in organic matter. The Torrie pipe also contains abundant xenoliths of both mantle and crustal affinities. More than 1250 meters of 4.5 cm diameter drill core were examined and sampled in the summer of 1996 from Tanqueray's drill core storage area in Calgary, Alberta. Sampling yielded approximately 35 peridotite, 20 granulite and 15 eclogite xenoliths ranging in size from <1-4 cm. Unfortunately, the friable nature of some of the drill core and extensive serpentinization of many of the xenoliths limited the number of mantle samples (ie. peridotites) available for detailed petrologic study to 14.

2.2 Xenolith Petrography

The Torrie xenolith suite consists of 1-4 cm diameter peridotites, websterites and harzburgites. Using the nomenclature of Harte (1977), peridotite xenoliths are coarse-equant (figure 2.1), porphyroclastic (figure 2.2) and granuloblastic. Complete petrographic descriptions for each sample are listed in Appendix 1.

Coarse-equant and granuloblastic peridotites consist of olivine (41-73 %), clinopyroxene (3-13 %), orthopyroxene (14-47 %), garnet (< 5 %), and spinel (<2 %). Texturally, coarse and granuloblastic samples differ with respect to grain size where the average grain size of coarse samples is > 2 mm and granuloblastic samples is < 2 mm (Harte, 1977). The relative grain sizes among constituient minerals in both coarse and granuloblastic samples remains constant where olivine, orthopyroxene and garnet are notably coarser than coexisting clinopyroxene and spinel. Additionally, texturally equilibrated phlogopite is present in both coarse and granuloblastic textured samples. The source of this mineral is enigmatic but may signal mantle metasomatism (Kopylova et al., in press).

Porphyroclastic samples exibit a bimodal distribution of grain sizes consisting of >4 mm olivine porphyroclasts, <1 mm olivine neoblasts, orthopyroxene (avg. ~ 1 mm), clinopyroxene (avg. ~ 0.4 mm) and garnet (avg. ~1.3 mm).The porphyroclastic texture results from dynamic recryatallization of olivine in response a unknown stress. Olivine neoblasts surround olivine porphyroclasts and exibit polygonal equant textures. Generally, porphyroclasts show serrated grain margins where in contact with neoblasts further documenting the dynamic recrystallization responsible for this texture. It should be noted that although porphyroclastic textures reflect textural disequilibrium, this does not necessarily correspond with chemical disequilibrium which will be noted later.

Olivines present in the peridotite samples have straight (polygonal) grain boundaries in most cases although slightly curved boundaries exist. Grain sizes vary from 0.1 mm olivine neoblasts in porphyroclastic samples TQY94-17-15A and TQ9513B to >4 mm porphyroclasts in the same samples (figure 2.2). On average the grain size is considerably less than equivalent samples from southern Africa, Siberia and Botswana (Boyd and Nixon, 1978; Boyd et al., 1997; Stiefenhofer et al., 1997). Many olivines show strain-induced undulose extinction which is best observed in porphyroclastic samples TQY94-17-15A and TQ9513B. Olivine has been extensively replaced by serpentine in many of the Torrie samples. The serpentine is present along fractures and as veinlets.

Garnets from the Torrie suite are colourless to very pale pink and vary from subhedral to anhedral grains that range in size from 0.1-<3.0 mm with average grain sizes of approximately 1.3 mm. Garnets occur as discrete grains and may contain <100 μm inclusions of olivine, orthopyroxene, clinopyroxene and mica (figure 2.4).

One sample (a garnet macrocryst TANQ93-2-45A), is ~ 1 cm in diameter and contains all the above mentioned inclusions and with some inclusion grain sizes in excess of 1 mm. In some instances secondary orthopyroxene and carbonate are observed infilling fractures throughout this macrocryst. The source of this orthopyroxene and carbonate is thought to be from reaction of the host kimberlite with garnet.

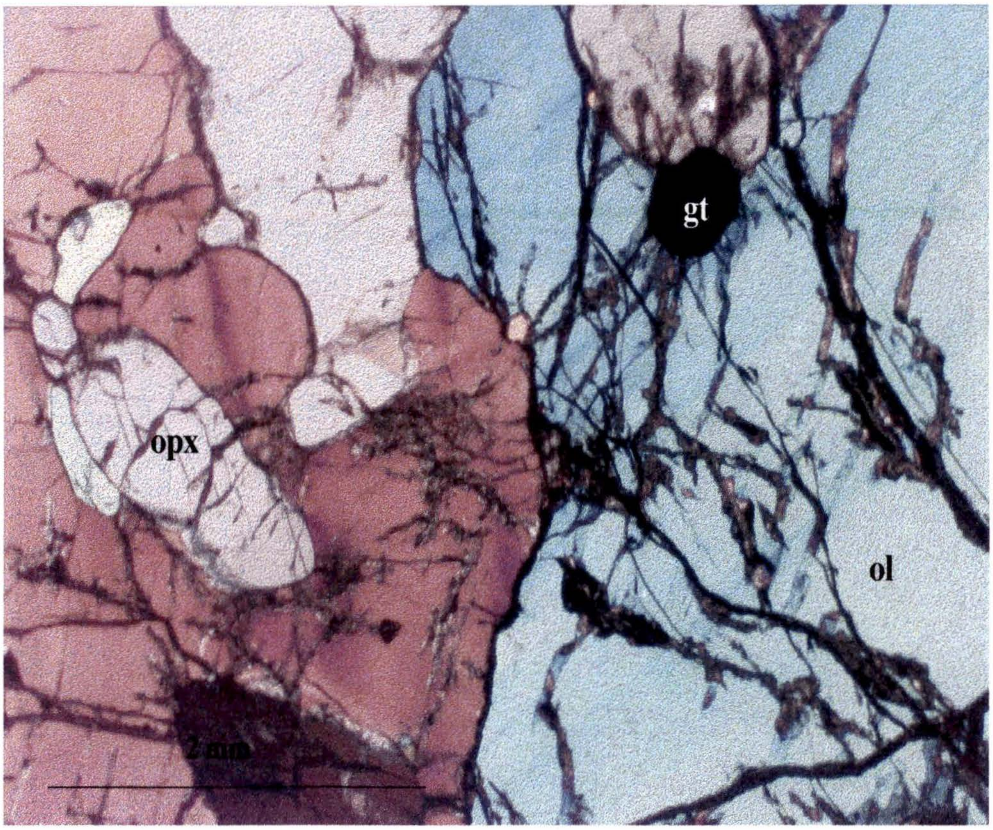

Figure 2.1: Photomicrograph of coarse grained garnet peridotite from the Torrie kimberlite (TANQ93-1-39, crossed polars).

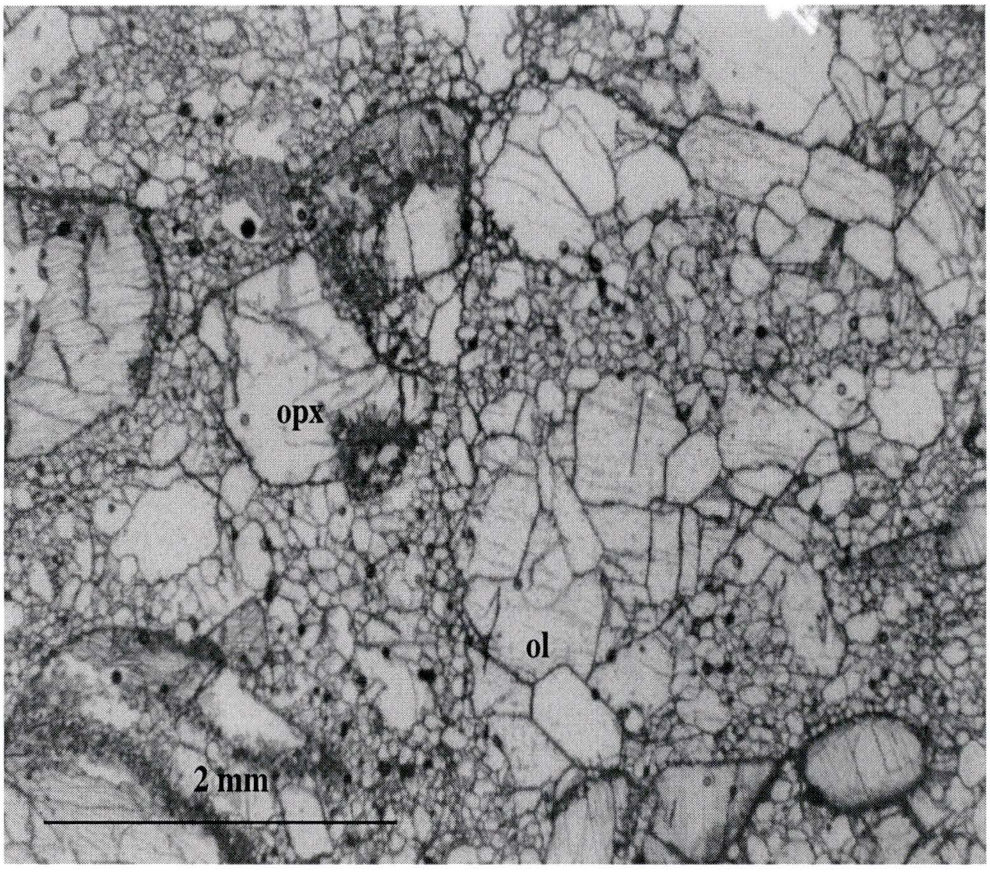

Figure 2.2: Photomicrograph of porphyroclastic sample from the Torrie kimberlite (TQ9513B, plane polarized light).

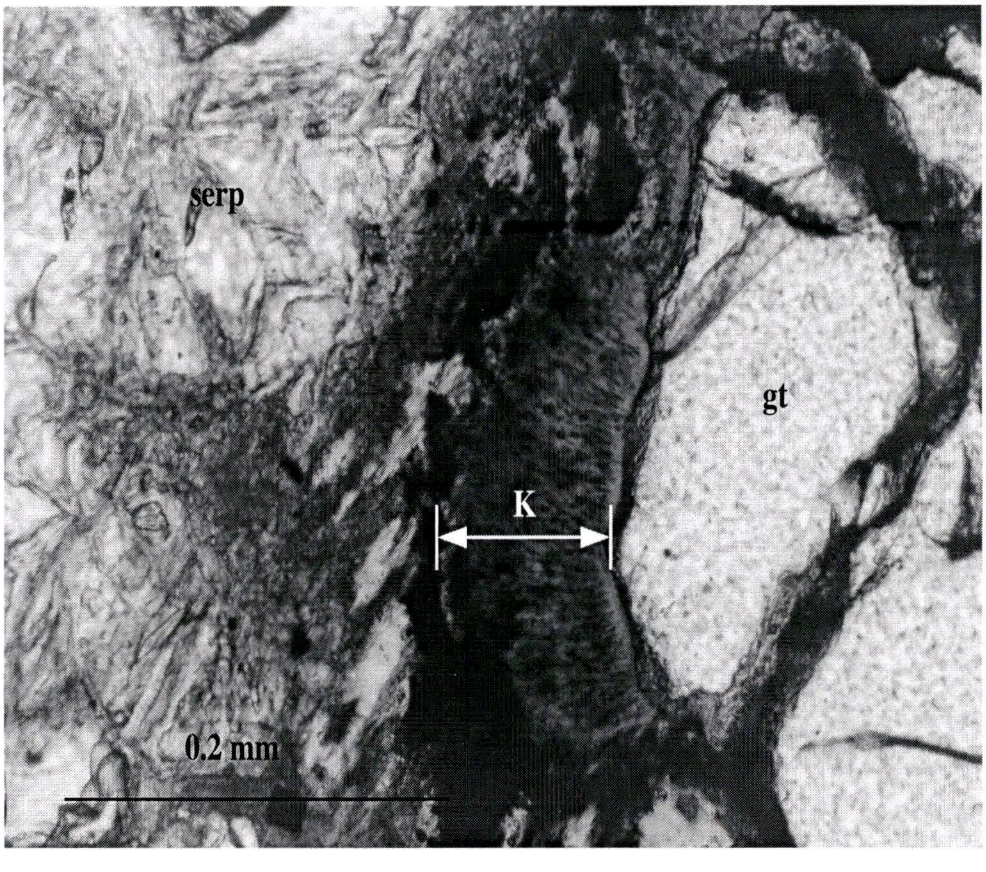

Figure 2.3: Photomicrograph of typical kelyphite rim (K) from the Torrie kimberlite (X9501A, plane polarized light).

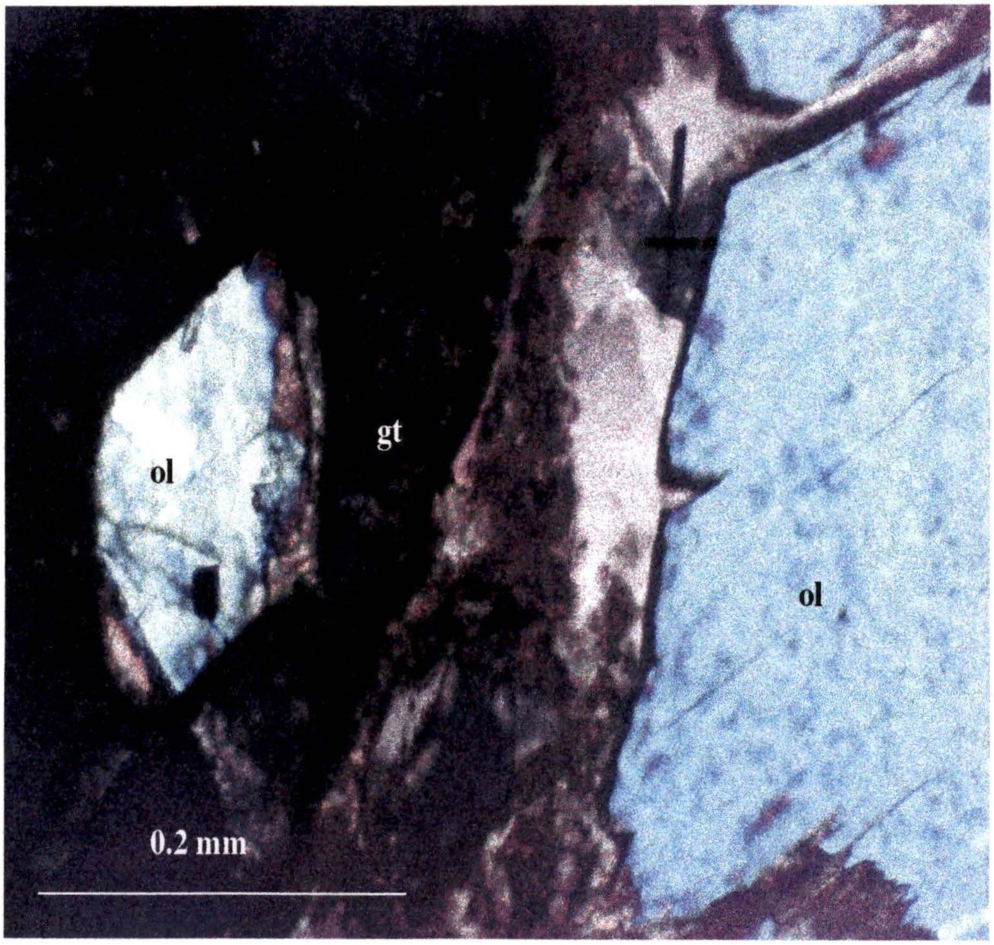

Figure 2.4: Photomicrograph of olivine (ol) inclusion in garnet (gt) in sample TANQ93-1-13 (crossed polars).

Orthopyroxenes occur as anhedral colourless grains with polygonal to slightly curved grain boundaries and have a grain size ranging from 0.2-3 mm. The average grain size of orthopyroxene is 1 mm.

Clinopyroxenes occur as sub-euhedral, mildly pleochroic pale green grains with polygonal to slightly curved grain boundaries. Clinopyroxenes have grain sizes from 0.2-2 mm, with an average of 0.3 mm.

Brown to dark red spinels occur as irregular anhedral grains ranging in size from 0.1-1 mm. Spinels are distributed irregularly throughout spinel peridotite (Sp peridotite) samples. Colourless to pale brown phlogopite is present as both texturally equilibrated coarse grains and mantling kelyphite rims on garnet, in both cases showing strain induced undulose extinction (figure 2.5). Pyrite, millerite, as well as other very minor sulphide phases (< 0.5 modal %) are also present as inclusions in garnet and interstitial to other grains but were not analyzed.

Compared to mantle xenoliths from the Kaapvaal and Siberian cratons (Boyd and Nixon 1978, Boyd et al., 1997) the mantle xenoliths from the Torrie suite generally show an overall smaller grain size, a lower abundance of coarse-equant textured samples and a distinct lack of deformed xenoliths although this discrepancy may be partially a function of the fewer xenoliths sampled by the Torrie kimberlite. Similarities with the Kaapvaal suite include the lack of dunites, the presence of coarse textures, texturally equilibrated phlogopite in many samples and the general orthopyroxene-rich modal character evident in the Torrie xenoliths as well as the relative proportions of eclogite and peridotite.

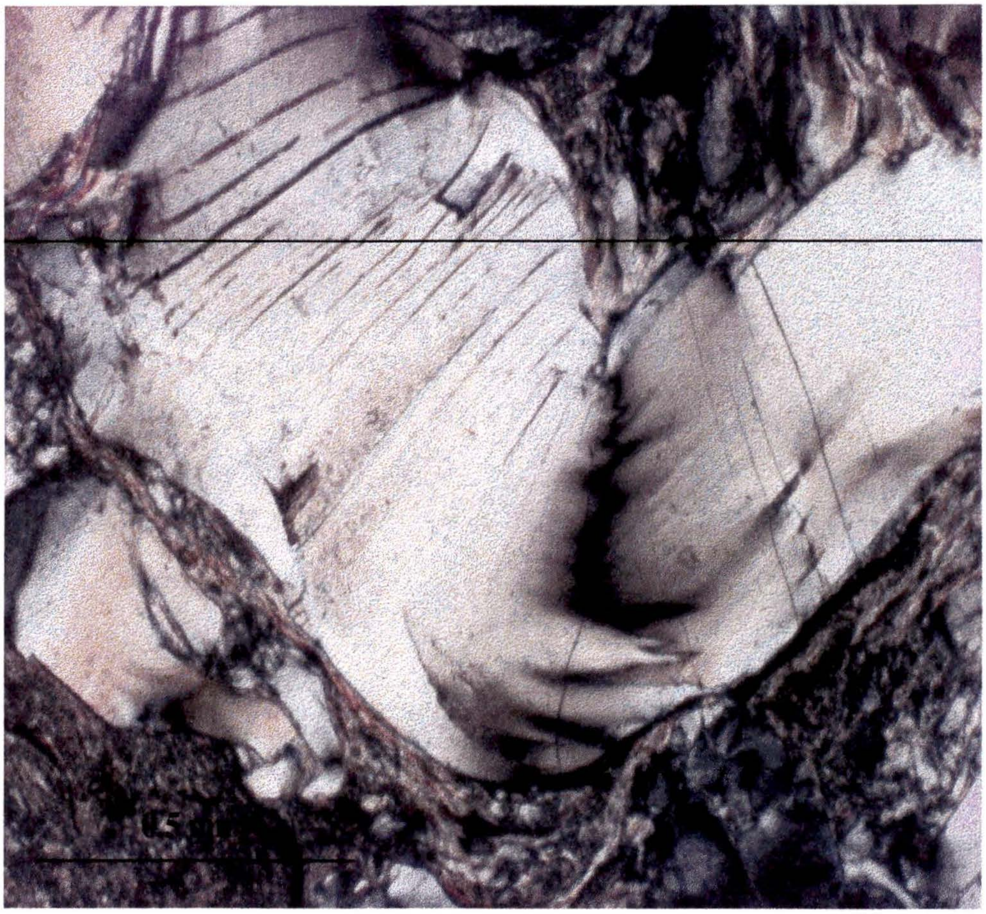

Figure 2.5: Photomicrograph of coarse phlogopite showing undulatory extinction in sample X9501A (crossed polars).

2.3 Alteration

Xenoliths from the Torrie suite are variably altered. Serpentine is observed pseudomorphing primary olivine and orthopyroxene (fig. 2.6) and interstitially along grain boundaries. Interstitial carbonate is also observed in some samples. The cause of this alteration is likely attributable to fluid-rock interaction during kimberlite emplacement resulting in partial replacement of olivine and orthopyroxene. The presence of carbonate in the Torrie suite also suggests post emplacement metasomatism, whereas mantle derived carbonate has been shown to be unstable and degrade during ascent of kimberlites (Canil, 1990). Additionally, secondary orthopyroxene present in sample TANQ93-2-45A is also interpreted as originating from reaction of garnet with the host kimberlite melt.

Clinopyroxene is variably altered to chlorite, clay minerals, and uralite. Garnet is, in many cases, mantled by secondary kelyphite with metasomatic phlogopite mantling some of these rims as well as occurring at the interface between the garnet and surrounding mineral assemblage. Phlogopite mantling kelyphite rims has also been observed in xenoliths from southern Africa (Boyd and Nixon, 1987). The origin of kelyphite [consisting of altered pyroxene and spinel (Reid and Dawson, 1972)] may be due to interaction of garnet and olivine which may have been subsequently altered by kimberlite derived fluids (Reid and Dawson, 1972).

2.4 Modal analysis

Modal data on peridotite samples was obtained by point counting thin sections under a petrographic microscope. Between 2000-6000 points/xenolith were counted with an automatic point counter at a variable grid spacing chosen to minimize counting errors as outlined in Solomon (1963). Errors associated with point counting were estimated using the formula:

$$\sigma^2(p_x) \leq \frac{0.44pa^3}{RA}[1+5.8(\frac{R}{a})^3] \quad (1)$$

where $\sigma^2(p_x)$ is the theoretical variance for phase (x), p is the fraction of phase (x), (A) is the measurement area (mm^2), (a) is the grid spacing (mm), and (R) is the grain radius (mm). Solomon (1963) indicates that in order to maintain a useful variance (a) should be at least (R/2) which was satisfied by the methods employed here. Modes were converted from volume % to weight % by multiplying volume modes by mineral densities.

In this study, particular attention was given to olivine-orthopyroxene ratios as these ratios provide important constraints on genetic models concerning the origin of cratonic mantle. Persuant to this, alteration minerals were counted simply as alteration and neither olivine nor orthopyroxene (or any other phase). If pervasive alteration selectively replaced olivine or orthopyroxene then there should be a correlation between degree of alteration and modal olivine or orthopyroxene. The Torrie xenoliths do not show such a correlation ($R^2 \sim 0.4$) (fig 2.7) and thus olivine/orthopyroxene ratios are concluded to be preserved in these samples.

The results show varying degrees of alteration (serpentinization/carbonation) from 20-70%. In garnet (Gt) and spinel (Sp) peridotites, modal olivine ranges from 41-73 wt.% with an average of 55 wt.%. Orthopyroxene ranges from 14-47 wt.% with an average value of 32 wt.%. Clinopyroxene ranges from 3-13 wt.% with an average value of 7 wt.%. Garnets range from 2-11 wt.% and average 5 wt.% and spinel modal abundances are between 2-15 wt.%. The large error evident in the spinel modes (Table 2.1) is due to the large grain size of the rock compared to the small grain size of the spinels combined with their relatively low abundance (Solomon, 1963).

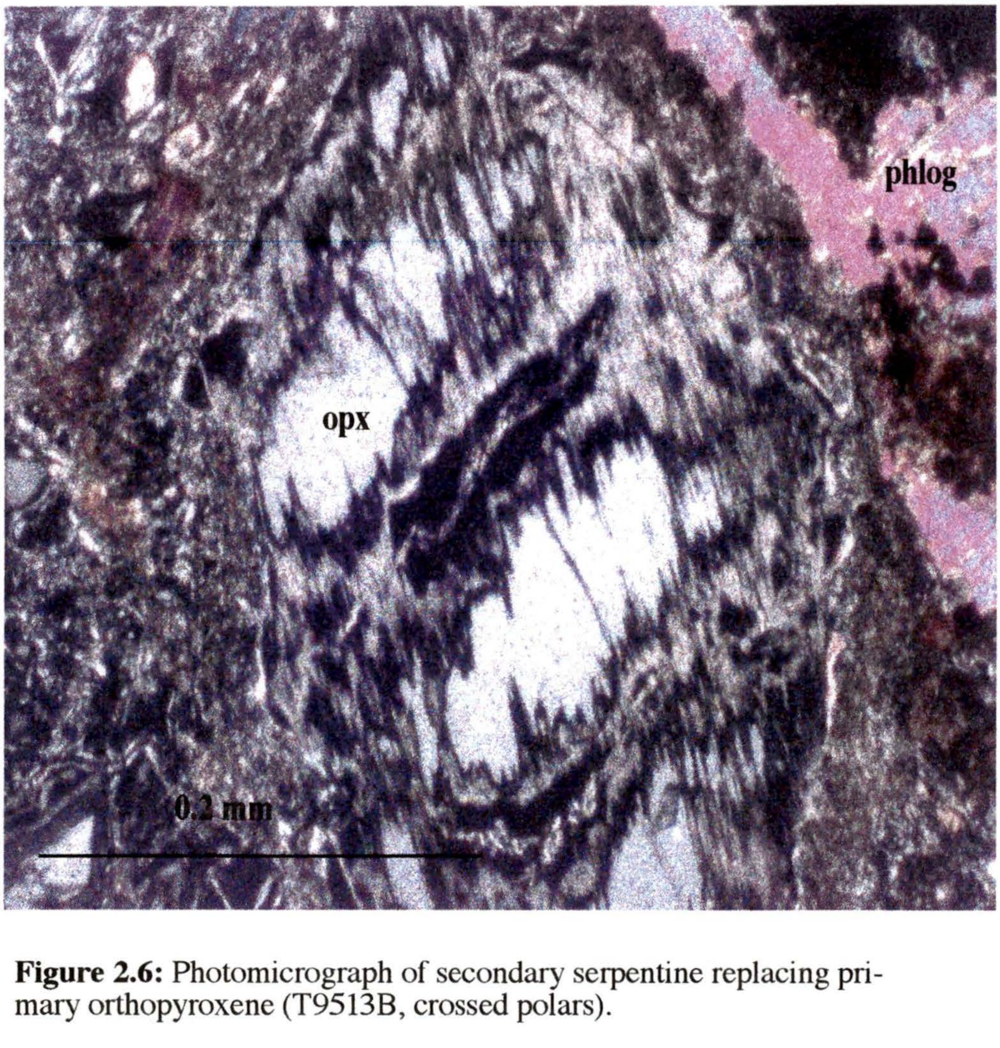

Figure 2.6: Photomicrograph of secondary serpentine replacing primary orthopyroxene (T9513B, crossed polars).

Table 2.1 Calculated modes (wt %) for Torrie xenoliths

Sample	type	texture	size(cm)	ol	opx	cpx	gt	spin	altn
TANQ93-1-39	GL	C	3	68 (4)	14 (1)	13 (2)	2 (4)	0	22%
TANQ93-1-13	GH	C	2	73 (3)	19 (2)	3 (8)	4 (5)	0	40%
TQ9513B	GL	P	3.8	54 (2)	35 (2)	6 (2)	3 (8)	0	19%
TQY94-17-15A	GL	P	1	51 (2)	32 (7)	13 (5)	3 (5)	0	26%
TANQ93-2-45A	GM	n.a	1.1**			n.a			
TQY94-17-22B1	GL	C	1*			n.a			
TQY94-17-11	GH	G	1.5**			n.a			
X9501A	GH	C	3	41 (2)	47 (1)	0	11 (4)	0	64%
X9501B	GH	C	1.2	10 (6)	56 (4)	<1	34 (9)	0	56%
TANQ93-2-35A	OW	C	2.3	26 (5)	66 (3)	8 (7)	0	0	68%
TQY94-17-22B2	SL	G	0.4*			n.a			
TQY94-17-22F	SL	C	2.1	44 (4)	47 (5)	5 (2)	0	2 (20)	34%
TANQ93-2-44B	OW	G	3.5	29 (8)	41 (8)	15 (5)	0	15 (11)	75%
TANQ93-2-45	SL	C	1**			n.a			

Modal data unavailable for samples TQY94-17-22B1, B2 (*broken thin section), (** epoxy plugs are optically non-transparent). Rock types include garnet and spinel lherzolite (GL, SL respectively), garnet harzburgite (GH), olivine websterite (OW) and a garnet macrocryst (GM). Textures include coarse (C), porphyroclastic (P), and granuloblastic (G) (textural nomenclature after Harte 1977).() indicate absolute error at 2σ.

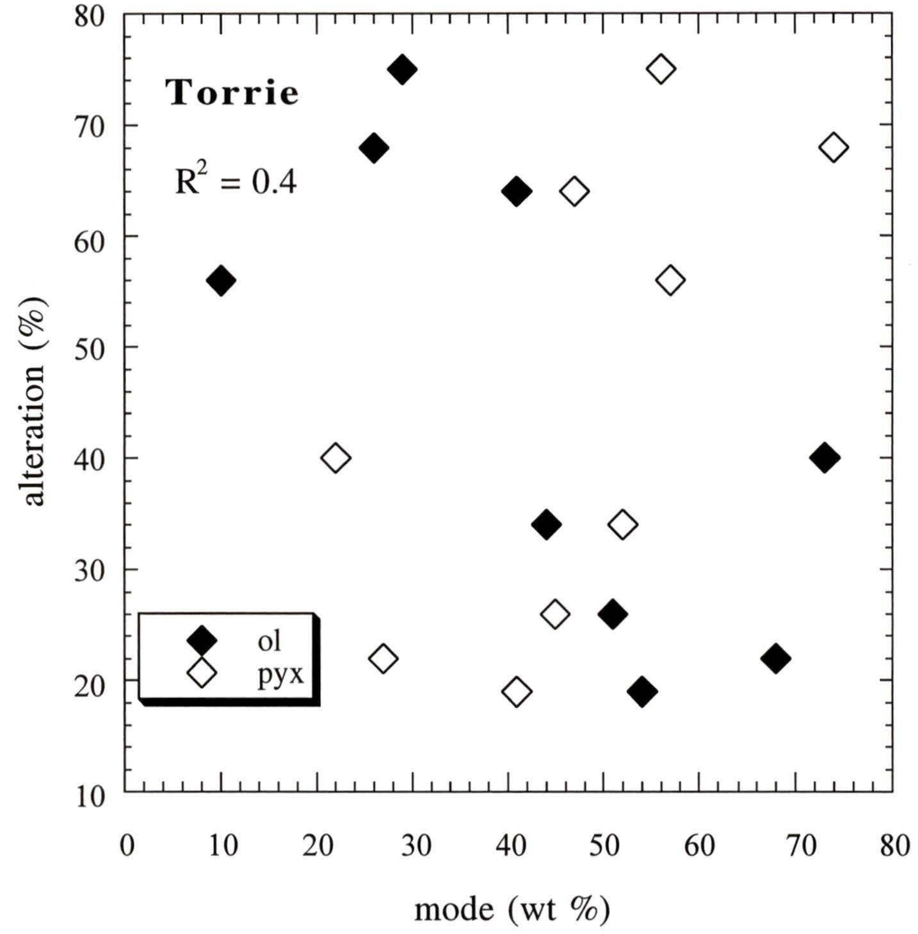

Figure 2.7: Plot of modal olivine (ol) and pyroxene [opx+cpx (pyx)] vs. percent alteration for the Torrie suite.

Cox et al. (1987) have observed a spatial relationship between orthopyroxene, garnet and clinopyroxene at centimeter scales in mantle xenoliths from southern Africa possibly attributable to an exsolution origin for garnet and clinopyroxene at the expense of orthopyroxene (Canil, 1991). With the small samples available for this study ($< 4\ cm^2$), we can neither confirm nor deny this effect although inspection of figure 2.8 indicates that there is a poor correlation between modal garnet and pyroxene (opx+cpx).

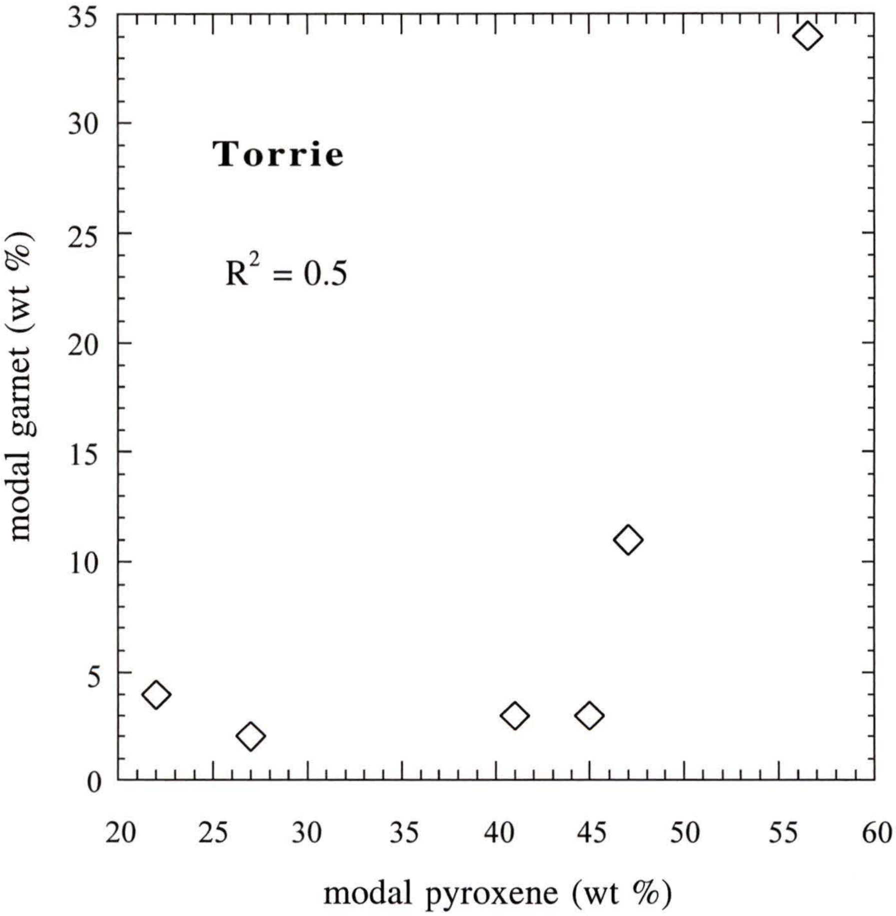

Figure 2.8: Plot of modal garnet vs. modal pyroxene (opx + cpx) for the Torrie suite. The results show no correlation between the two minerals indicating the they may not be spatially related.

2.5 Summary

The modes calculated in this study (Tables 2.1, 2.2) are most similar to the coarse, low temperature (<1100°C), Gt peridotites from the Kaapvaal craton (Boyd and Mertzman, 1987) and, on average, contain more orthopyroxene than peridotites from Udachnaya (Boyd et al., 1997) (Table 2.2). Cratonic xenoliths hosted in the Grizzly pipe, located in the Lac de Gras region, have average values for olivine and orthopyroxene of 86% and 10%, respectively and are unlike the modes calculated for the Torrie pipe (FR Boyd, pers. comm. 1998).

Table 2.2 Comparison of average modes for peridotites from high (>1100°C) and low (<1100°C) temperature garnet peridotites (GP) from South Africa (Kaapvaal, Boyd and Mertzman, 1987)), Siberia (Udachnaya, Boyd et al 1997) and Canada (Torrie pipe, Slave craton, this study)

	Kaapvaal	Kaapvaal	Udachnaya	Udachnaya	Torrie
	GP	GP	GP	GP	GP
	low T	high T	low T	high T	
ol	62	75	72	71	58
opx	31	16	21	20	30
cpx	2	3	2	4	7
gt	5	6	5	5	5

CHAPTER 3

MINERAL CHEMISTRY

3.1 Analytical methods

Samples were analyzed using a CAMECA SX50 electron microprobe at the University of British Columbia (UBC) and a JEOL JXA 8900 microprobe at the University of Alberta (UofA) in wavelength dispersive mode. Major and minor elements were determined at 15.0 kV acceleration voltage and a beam current of 20.1 nA (UBC) and 15 nA (UofA) with peak counting times of 20 seconds for Na, Mg, Al, Si, Ca, K, Ti, Cr, Mn and Fe for all phases. Al in orthopyroxene was counted for 40 seconds at the same operating conditions. Ca in olivine was measured at 15.0 kV acceleration voltage and 30.2 nA beam current for 100 seconds following the method of Dalton and Lane (1996). Ni in olivine was counted for 300 seconds at 15 kV acceleration voltage and a beam current of 50nA. Standards included natural albite (Na,Al,Si), pyrope (Ca,Si,Mg, Fe), rutile (Ti) wollastonite (Ca) anorthite (Ca,Si,Al), orthoclase (K,Al) diopside (Ca,Mg,Si,Mn), grossular (Ca,Al,Si), scapolite (Al, Si) as well as synthetic magnesio-chromite (Cr,Fe) forsterite (Mg,Si), fayalite (Fe,Si), rhodonite (Mn) and spinel (Mg,Al). Standard ZAF corrections were applied to all analyses. Mineral chemical analyses obtained for a single sample analyzed using electron microprobes at both UBC and UofA differ by less than 5% in all the phases anaylzed.

In each sample, between two and four grains of each mineral were analyzed. Two to six points on cores and rims of each grain were analyzed to evaluate compositional heterogeneity on a mineral and xenolith scale. Special care was taken during the analysis of Ca in olivine to avoid effects of secondary fluorescence, as described in Dalton and Lane (1996). Overall, xenoliths were chemically homogeneous at all scales with a few exceptions that will be described in chapter 5. Mineral chemical analyses are listed in Appendix 2. Uncertainties originate from: 1) counting statistics and 2) grain heterogeneity. In all cases, the latter error is largest yielding a maximum uncertainty of less than 2% of the measured value.

3.2 Mineral Chemistry

3.2.1 Olivine

Olivines from the Torrie suite have a range in Mg # (Mg/Mg+Fe) of 0.91-0.94 and an average value of 0.92 (fig 3.1). An olivine inclusion in garnet macrocryst TANQ93-2-45A has a distinctly lower Mg# of 0.89 due to the large volume of garnet encasing the olivine inclusion, effectively buffering its Mg# to lower values. This buffering effect is also observed in the pyroxene inclusions in the same sample which are more Fe-rich. Excluding the olivine inclusion, the range in olivine Mg# is consistent with other olivines in cratonic mantle peridotites from southern Africa (avg. Mg#=0.93, Boyd et al., 1997), Siberia (avg. Mg#=0.93, Boyd et al., 1997), Somerset Island (avg. Mg#=0.92, Schmidberger and Francis, 1998) and the nearby Grizzly pipe (avg. Mg#=0.93, Boyd and Canil, 1997) in the central Slave Province. NiO in olivine averages 0.38wt.% ± 0.02 (2σ). The NiO content of olivine in peridotites from the Grizzly pipe (~0.35 wt%, F.R. Boyd, pers. comm., 1997) is somewhat lower than Torrie, whereas olivine from Siberia and southern Africa have marginally higher NiO contents (~ 0.39 and 0.41 respectively) (F.R. Boyd, pers. comm., 1997). Olivines have low concentrations of trace elements CaO, TiO_2, Al_2O_3, and Cr_2O_3.

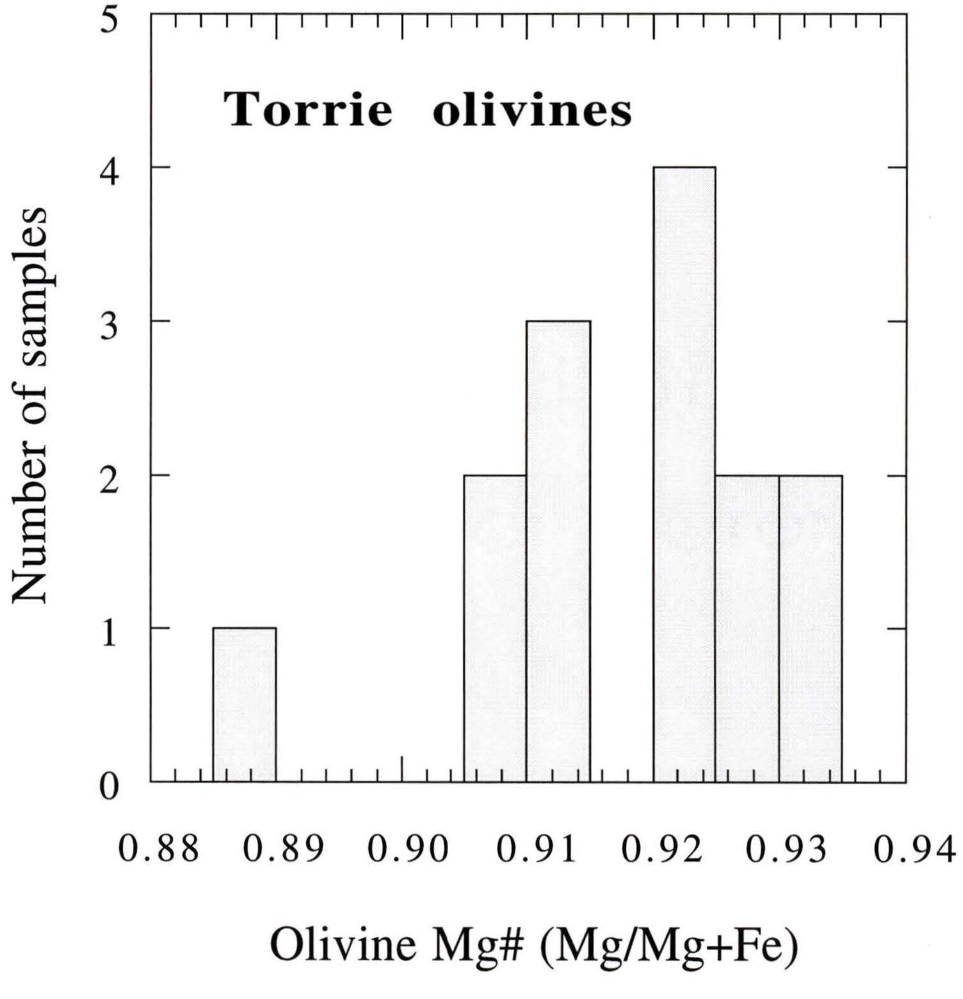

Figure 3.1: Distribution of olivine Mg#'s for the Torrie peridotites.

Reported values taken from average analyses of cores of olivines.

3.2.2 Garnet

Garnets range from $Gr_5Py_{78}Alm_{17}$ to $Gr_{22}Py_{59}Alm_{19}$ and are largely of the lherzolitic variety with garnets from two samples plotting in the harzburgitic field based on CaO vs. Cr_2O_3 systematics (Sobolev et al., 1973) (fig 3.2). Lherzolitic garnets are calcium enriched and formed in rocks containing clinopyroxene whereas harzburgitic garnet formed in the absence of clinopyroxene and subsequently calcium undersaturated conditions (Gurney, 1984). Garnets have Mg#'s ranging from 0.75-0.85. The Cr_2O_3 contents range from 4.5-6.5 wt% and TiO_2 contents are generally low (<1 wt%) (Appendix 2). The garnets are not chemically zoned and are homogeneous at the thin section scale.

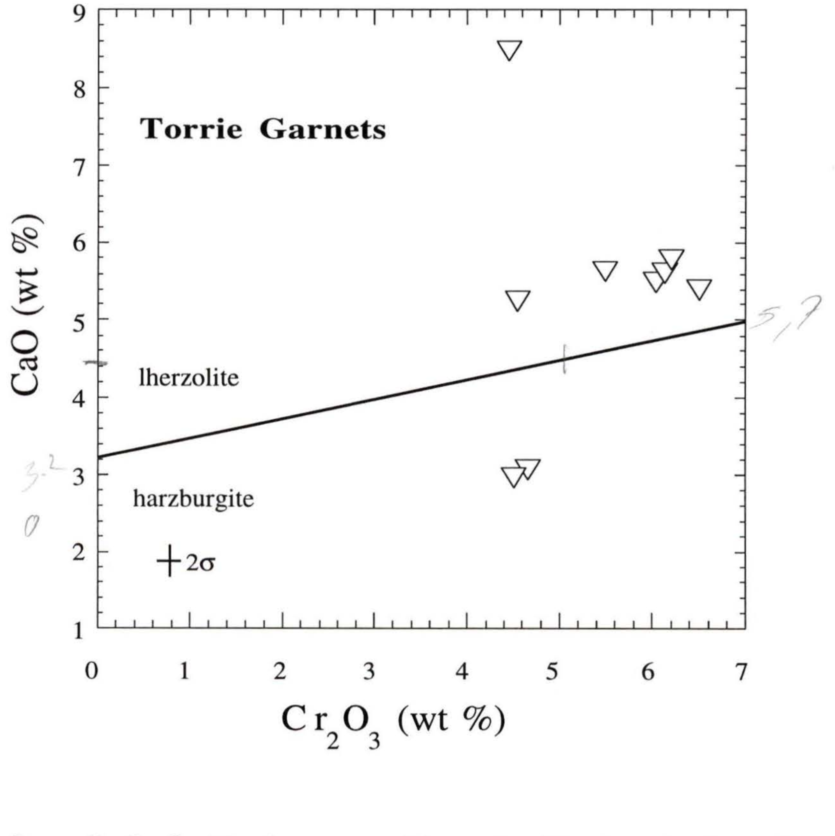

Figure 3.2: CaO vs. Cr_2O_3 for Torrie garnets. Lherzolite-Harzburgite line after Sobolev et al., (1973).

3.2.3 Orthopyroxene

Orthopyroxenes are all aluminous enstatites (En_{91}-En_{94}) with Al_2O_3 contents from 0.5-3.6 wt% and a range of in (Ca/Ca+Mg)*100 from 0.45-2.29 (fig 3.3). The most aluminous enstatites (1.5-3.6 wt% Al_2O_3) occur in the spinel lherzolites (Appendix 2), similar to comparable samples from Siberia (Boyd et al., 1997), Canada (Kopylova et al., 1998; Schmidberger and Francis, 1998, submitted; and southern Africa (Boyd and Nixon, 1987). Orthopyroxenes are relatively rich in Cr_2O_3 (0.27-0.60 wt% Cr_2O_3) and poor in Na_2O (0.01-0.13 wt% Na_2O) and TiO_2 (<0.15 wt% TiO_2) similar to comparable samples from the Kaapvaal craton in southern Africa (Boyd and Nixon, 1978), Siberia (Boyd et al., 1997) and Canada (Kopylova et al., 1997; Schmidberger and Francis, 1998, submitted).

3.2.4 Clinopyroxene

Clinopyroxenes are all Cr-diopsides with a range in (Ca/Ca+Mg) from 0.37-0.51 (fig 3.4) also similar to comparable samples from the Kaapvaal craton in southern Africa (Boyd and Nixon, 1978). Cr_2O_3 and Na_2O contents are generally low, ranging from 0.32-1.5 wt% and 0.26-1.6 wt% respectively (Appendix 2) . TiO_2 contents are also low (0.3 wt% TiO_2). Three samples, TQY94-17-15A, TANQ93-1-39 and TANQ93-1-13, have clinopyroxenes which show an increase in CaO, and a decrease of MgO and Na_2O from core to rim, reflecting either growth at a lower temperature or Ca-metasomatism possibly precursory to kimberlite magmatism (Appendix 2).

3.2.5 Spinel

Spinels in the Torrie suite are dominantly magnesiochromites (Appendix 2) with Mg#'s (Mg/Mg+Fe) ranging from 0.67-0.78 and Cr#'s ($Cr/Cr+Fe^{3+}+Al$) between 0.14-0.35, similar to spinel samples from southern Africa and Siberia (Boyd and Nixon, 1978; Boyd et al., 1997).

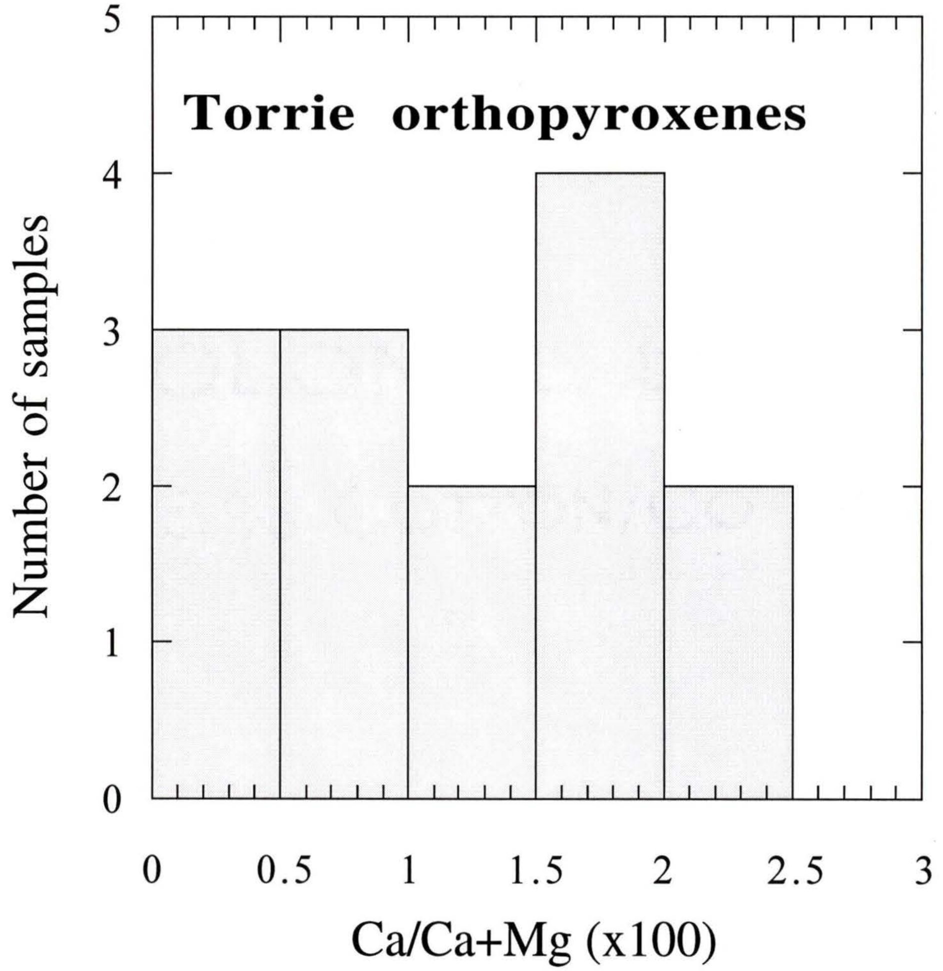

Figure 3.3: Distribution of orthopyroxene Ca/Ca+Mg x100 for the Torrie Peridotites.

Reported values taken from average analyses of cores of orthopyroxenes.

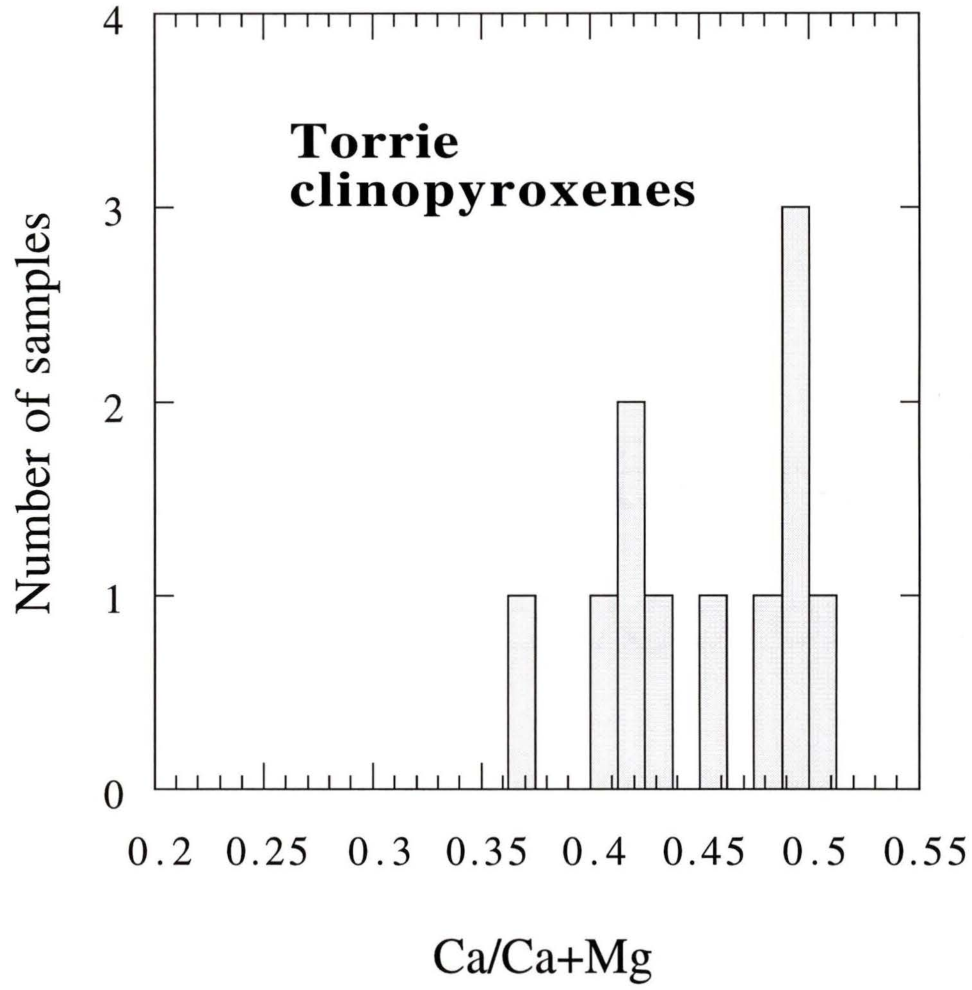

Figure 3.4: Distribution of clinopyroxene Ca/Ca+Mg for the Torrie peridotites

Reported values taken from average analyses of cores of clinopyroxenes.

3.3 Summary

Generally, xenoliths from the Torrie kimberlite pipe are homogeneous at both the thin section and grain scales with the exception of a few samples which will be discussed in chapter 5. The chemical homogeneity evident in these samples indicates that they have resided under ambient mantle conditions for a sufficient period of time for chemical equilibrium to be attained. Equilibrium is an essential assumption in applying the equilibrium geothermobarometry which will be discussed in Chapter 4.

CHAPTER 4

GEOTHERMOBAROMETRY

4.1 Geothermobarometry

Geothermobarometry refers to pressure and temperature (P-T) estimations based on the chemical or physical state of one or more minerals in a particular rock (Bohlen and Lindsley, 1987). Geothermometers and geobarometers are based on the temperature or pressure dependence, respectively, of various mineral equilibria within a given assemblage.

Thermodynamically, equilibria that are well suited for geothermometry have large values of ΔH^{o}_{rxn} (change in enthalpy). For example, the larger the value of ΔH^{o}_{rxn}, the larger the equilibrium constant (K) changes with temperature (Wood and Fraser, 1977). If ΔH^{o}_{rxn} is large, an error in ΔH^{o}_{rxn} or in the activity-composition relationships of the phases involved will produce a relatively small error in calculated temperature (Wood and Fraser, 1977). Equilibria well suited for geobarometry have large values of ΔV^{o}_{rxn} (change in volume) associated with their equilibrium and so K changes with pressure (Wood and Fraser, 1977).

Most geothermometers applicable to mantle rocks are based on equilibria between some combination of co-existing olivine, orthopyroxene, clinopyroxene, garnet and spinel. The geothermometers used in this study broadly fall into two categories: 1) exchange geothermometers based on the temperature dependence of various cation exchange equilibria in a given assemblage, for example, the exchange of Fe and Mg between coexisting olivine and garnet:

$$\underset{(Fa)}{Fe_2SiO_4} + \underset{(Pyrope)}{Mg_3Al_2Si_3O_{12}} \Leftrightarrow \underset{(Fo)}{Mg_2SiO_4} + \underset{(Alm)}{Fe_3Al_2Si_3O_{12}} \qquad (2)$$

where Fa and Fo are the fayalite (Fe) and forsterite (Mg) components in olivine and Pyrope, Alm are the pyrope (Mg) and almandine (Fe) components in garnet, respectively. 2) solvus geothermometers based on the temperature dependence of the solubility of a component in a phase in the rock. As an example, consider the two-pyroxene solvus geothermometer:

$$\underset{(opx)}{En\ (Mg_2Si_2O_6\ )} \Leftrightarrow \underset{(cpx)}{En\ (Mg_2Si_2O_6)} \qquad (3)$$

where En is the enstatite ($Mg_2Si_2O_6$) component in opx and cpx.

There are notably fewer geobarometers applicable to mantle assemblages and these may be designated into similar categories as those noted above. An example of an exchange geobarometer is the Al in opx geobarometer based on the following reaction:

$$\underset{(En)}{Mg_2Si_2O_6} + \underset{(Mg\text{-}Ts)}{MgAl_2SiO_6} \Leftrightarrow \underset{(Pyrope)}{Mg_3Al_2Si_3O_{12}} \qquad (4)$$

where (Mg-Ts) is the Mg-Tschermacks component in opx (En) and garnet (Pyrope)

4.2 Methods

Pressures and temperatures of equilibration for the Torrie suite were obtained using a number of published combinations of geothermometers and geobarometers in an iterative procedure (Brey and Köhler, 1990). The geothermobarometers used in this study are given the following notations:

1)T_{BKN} [Two-pyroxene thermometer - Brey and Köhler (1990)]

2)T_{ONEILL} [Fe-Mg exchange between Ol and Gt thermometer - O'Neill and Wood (1979)]

3)T_{HARLEY} [Fe-Mg exchange between Opx and Gt thermometer - Harley (1984)]

4)$T_{Ca\ in\ opx}$ [Ca in Opx thermometer - Brey and Köhler (1990)]

5)T_{KROGH} [Fe-Mg exchange between Cpx and Gt thermometer - Krogh (1989)]

6)P_{KB} [Ca exchange between Ol and Cpx barometer - Köhler and Brey (1990)]

7)P_{BKN} [Al-in-Opx barometer - Brey and Köhler (1990)]

8)P_{NG85} [Al-in-Opx barometer - Nickel and Green (1985)]

9)P_{INT} [intersection of P-T gradient with geotherm, after Fung and Haggerty (1995)]

Brey and Köhler (1990) assessed the ability of available geothermometers and geobarometers applicable to mantle assemblages to reproduce experimental P-T conditions. The results of their study are summarized in Table 4.1. T_{HARLEY} was found by Brey and Köhler (1990) to overestimate and underestimate at low and high temperatures, respectively, by as much as 120°C (1σ). Brey and Köhler (1990) also found P_{NG85} to overestimate and underestimate at low and high pressures, respectively, by as much as 0.5 GPa.

In addition to the above geothermometers and geobarometers, Brey and Köhler (1990) found that the following combinations, when solved for in an iterative procedure, were best suited for estimating equilibrium pressure and temperature conditions: 1) T_{BKN}-P_{BKN}, 2) T_{BKN}-P_{KB}, 3) T_{KROGH}-P_{BKN} and 4) T_{ONEILL}-P_{BKN}. The uncertainties associated with these combinations are listed in Table 4.1

The presence of Fe^{3+} in minerals presents problems when estimating equilibrium P-T's. Routine electron microprobe analyses report all Fe as total Fe (ΣFe) and do not distinguish the amount of Fe^{3+} relative to Fe^{2+} present in a given mineral. The latter quantities are only attainable by calculation assuming stoichiometry for the mineral in the absence of other techniques such as wet chemistry of ^{57}Fe Mössbauer spectroscopy. Canil and O'Neill (1996) show that calculated Fe^{3+} in clinopyroxene and garnet using stoichiometry is too imprecise to be "petrologically useful" whereas calculated Fe^{3+} in spinel can provide a reasonable estimate of Fe^{3+} contents. Canil and O'Neill (1996) also note that Fe^{3+} in olivine is essentially zero.

Calculating the amount of Fe^{3+} in phases, rather than analysing for it independently, directly affects the Mg/Fe^{2+} ratio used to estimate temperatures using Fe^{2+}-Mg exchange thermometers (Canil and O'Neill, 1996). Two-pyroxene solvus equilibria (T_{BKN}) do not directly involve Fe-Mg exchange, thus they are relatively unaffected by the presence of Fe^{3+} on calculated temperatures. Canil and O'Neill (1996) showed that calculated T_{BKN} temperatures changed by less than ± 30°C when Fe^{3+} was considered compared to when it was not. Thus T_{BKN} yields the most robust estimate of equilibrium temperatures.

Canil and O'Neill (1996) show that better agreement between calculated temperatures using T_{BKN} and Fe^{2+}-Mg exchange thermometers is attained if Fe^{3+} is ignored in their calculation. This observation may indicate that Fe^{3+} in the natural samples were similar to those in the experiments used to calibrate the Fe-Mg exchange geothermometer but this may not always be the case. This particular type of uncertainty associated with Fe^{2+}-Mg exchange thermometers cannot be quantified and hence calculated temperatures using this approach are more prone to error and uncertainty (Canil and O'Neill, 1996).

In the absence of available geobarometers, equilibrium pressures (P_{INT}) may be estimated by calculating T (Fung and Haggerty, 1995) and projected to a geothermal gradient described by the remainder of the Torrie samples which will be discussed later. For samples TQY94-17-22F and TANQ93-2-44B, temperatures were calculated using T_{BKN} at assumed pressures of 1-6 GPa, and the equilibrium P-T condition was then estimated where the calculated P-T gradient intersects the geothermal gradient (fig 4.1). Pressures were calculated using this method for samples in which P_{KB} yielded geologically unreasonable values (ie. negative pressures). Pressure estimates were converted to depths using the relationship:

$$P=\rho gz \tag{5}$$

where P is pressure (Pa), ρ is density (crust= 2800 kg m^{-3}, mantle= 3200 kg m^{-3}), g is acceleration of gravity (9.8 m s^{-2}) and z is the depth (m).

Table 4.1: Error estimates for the geothermobarometers used in this study (from Brey and Köhler, 1990).

Thermometer (T)	error (T- ±°C)	Barometer (P)	error (P- ±GPa)	combination (P-T)	error (P- ±GPa, T- ±°C)
T_{BKN}	15	P_{BKN}	0.22	P_{BKN}- T_{BKN}	0.3, 20
$T_{Ca\ in\ opx}$	19	P_{KB}	0.44	P_{KB}- T_{BKN}	0.44, 23
T_{KROGH}	62	P_{NG85}	0.5	P_{BKN}- T_{KROGH}	0.52, 62
T_{ONEILL}	113			P_{BKN}- T_{ONEILL}	0.71, 113
T_{HARLEY}	120				

Errors are reported at 1σ.

4.3 Pressures and temperatures

Chemical homogeneity of minerals and agreement among calculated temperatures using different thermometers is an indication that equilibrium has been achieved in a sample. Most minerals in the Torrie xenoliths are chemically homogeneous. Calculated equilibrium P-T solutions for several geothermobarometer combinations applied to the Torrie suite are listed in Appendix 3. Figures 4.2-4.5 are plots of temperatures calculated with different thermometers relative to T_{BKN} (ΔT) at an assumed pressure for peridotites from the Torrie suite for which T_{BKN} is available.

Temperatures were calculated at a constant pressure to remove any pressure effect in estimating temperatures. The data in figures 4.2-4.4 show that all geothermometers underestimate T compared to T_{BKN} but they all agree with this temperature within their quoted errors (at 2σ). The exception is $T_{\text{Ca in opx}}$ (fig 4.5) which both over- and underestimates temperatures calculated using T_{BKN}. The source of the discrepancy between T_{BKN} and $T_{\text{Ca in opx}}$ is not known but may be a consequence of analytical uncertainty for Ca in orthopyroxene or is related to interaction with Ca-rich fluids which overprinted the primary orthopyroxene composition and thus affected calculated temperatures. Curiously, Brey and Köhler (1990) found the same discrepancy when they applied $T_{\text{Ca in opx}}$ to a suite of mantle xenoliths from the Kaapvaal craton. Brey and Köhler (1990) attributed the difference to the influence of Na in opx which may have affected the activity-composition relationships used in the application of this geothermometer. This interpretation may also explain the differences between T_{BKN} and $T_{\text{Ca in opx}}$ for the Torrie suite.

In addition to solving P and T simultaneously, geothermometers were applied at a constant pressure and geobarometers at a constant temperature in order to critically evaluate P-T's obtained using the core and rim compositions as input parameters.

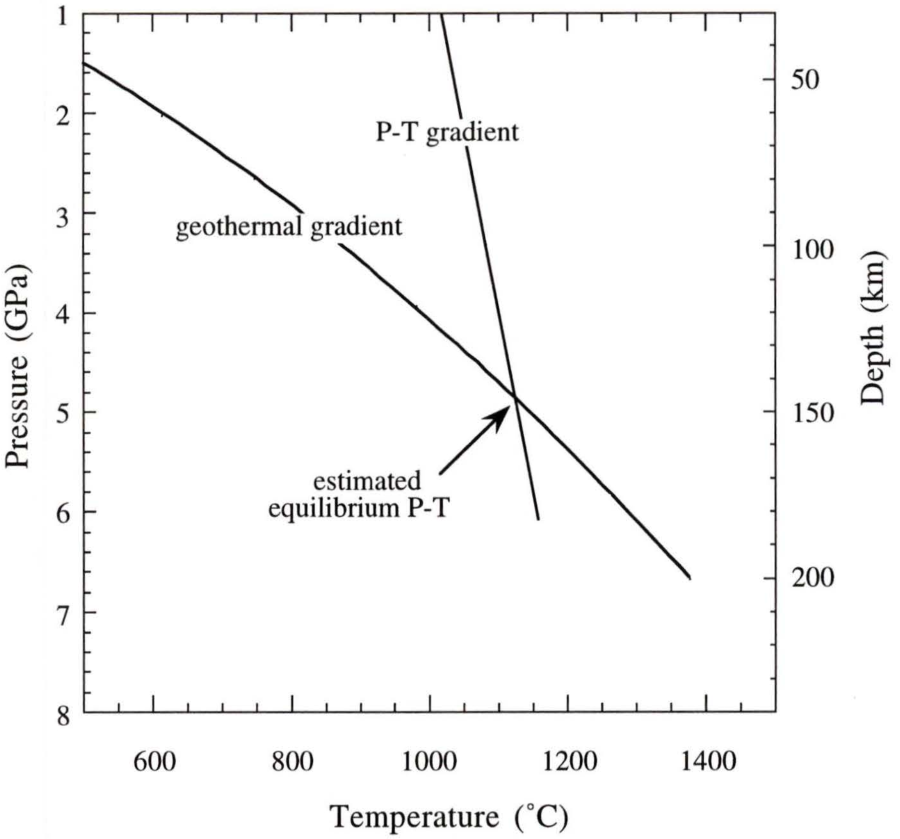

Figure 4.1: Example calculation of P-T condition for peridotite samples for which no geobarometer is available (P_{INT}) calculated after the methods of Fung and Haggerty (1995). Intersection of P-T gradient with geothermal gradient provides an estimate of equilibrium P-T.

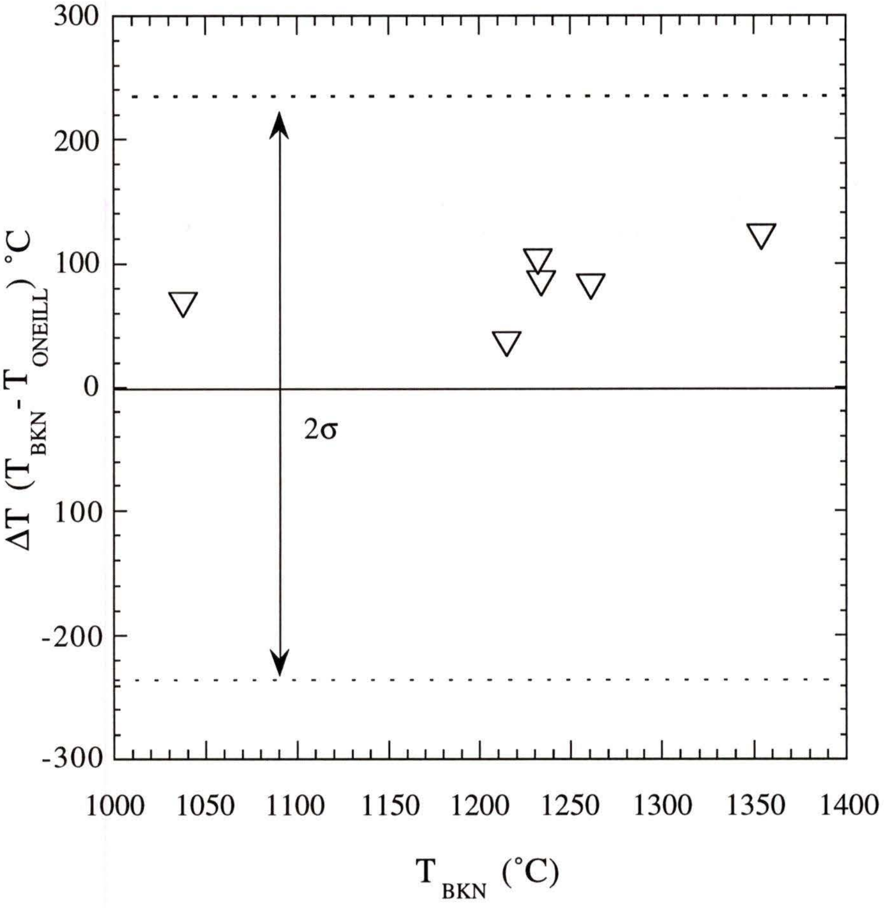

Figure 4.2: ΔT (T_{BKN} - T_{ONEILL}) at an assumed pressure of 5 GPa vs. T_{BKN} calculated with P_{BKN} for samples where garnet, olivine (T_{ONEILL}), orthopyroxene and clinopyroxene (T_{BKN}) are present. 2σ uncertainty level for T_{ONEILL}.

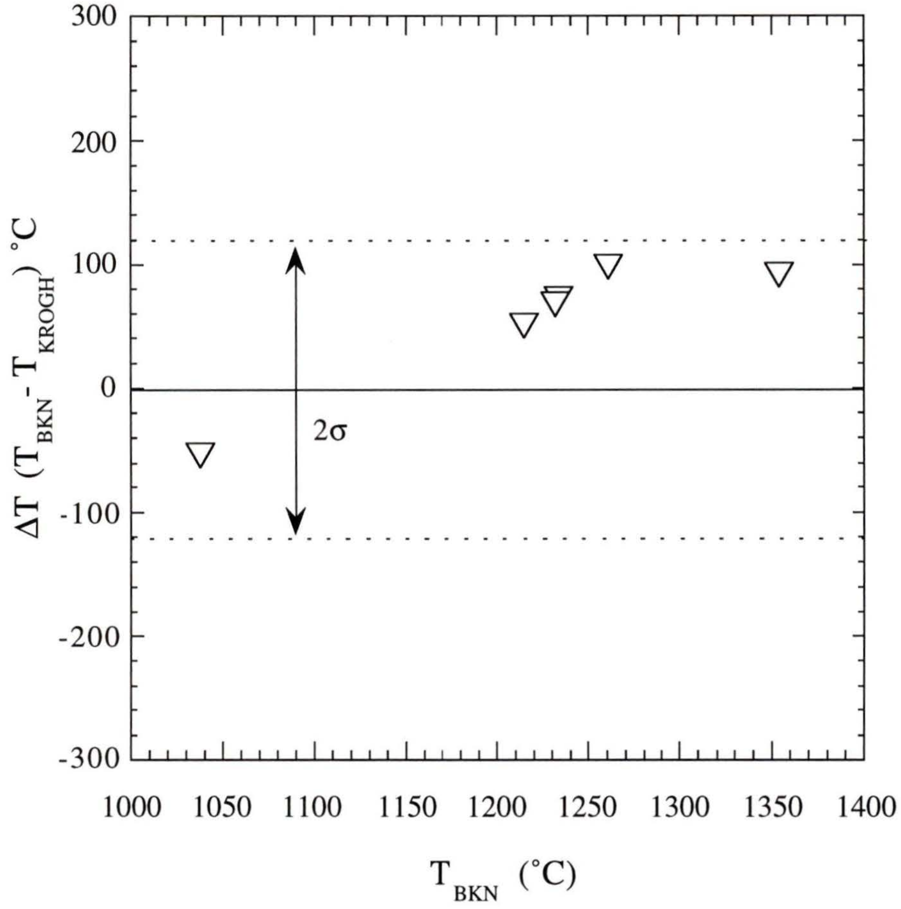

Figure 4.3: ΔT (T_{BKN} - T_{KROGH}) at an assumed pressure of 5 GPa vs. T_{BKN} calculated with P_{BKN} for samples where garnet, olivine, orthopyroxene and clinopyroxene (T_{BKN}) are present. 2σ uncertainty level for T_{KROGH}.

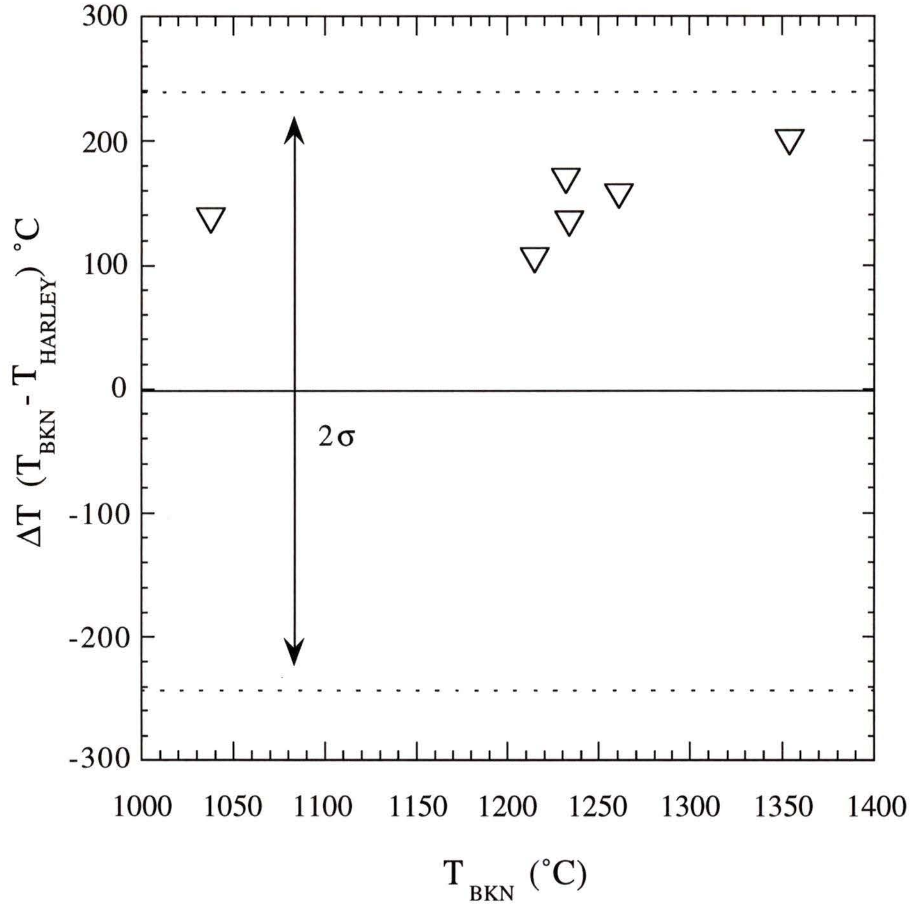

Figure 4.4: ΔT (T_{BKN} - T_{HARLEY}) at an assumed pressure of 5 GPa vs. T_{BKN} calculated with P_{BKN} for samples where garnet, olivine, orthopyroxene and clinopyroxene (T_{BKN}) are present. 2σ uncertainty level for T_{HARLEY}.

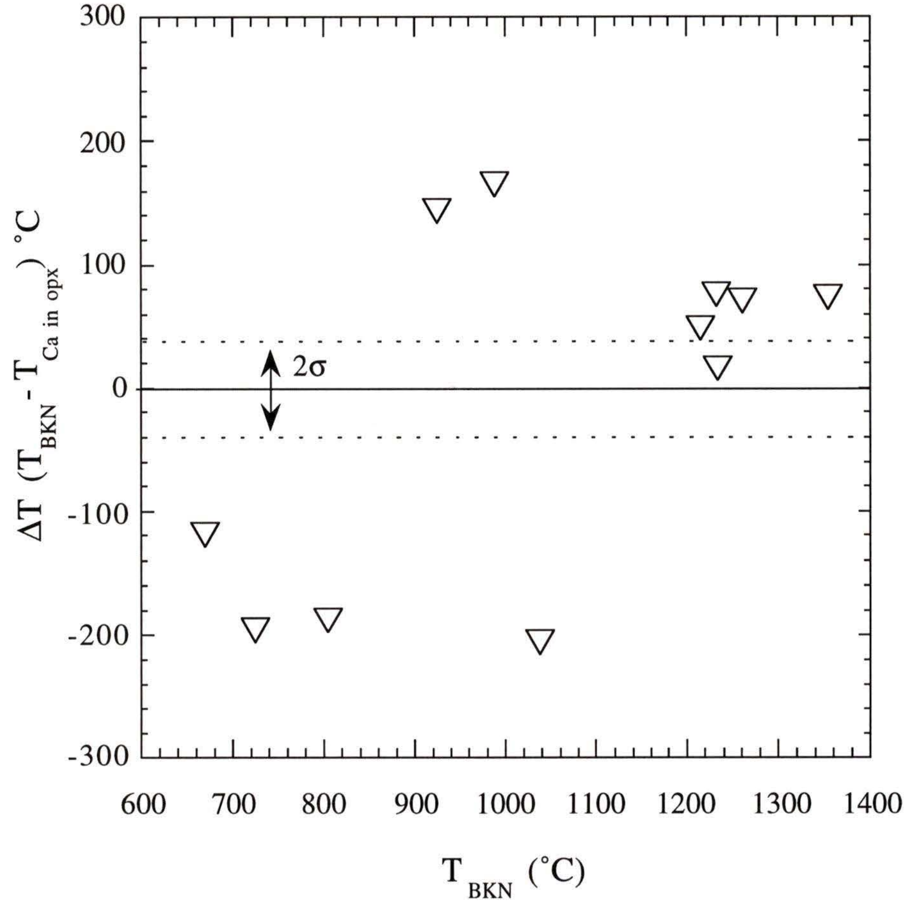

Figure 4.5: ΔT (T_{BKN} - $T_{Ca\ in\ opx}$) at assumed pressures of 5 and 2 GPa for garnet and spinel bearing samples, respectively vs. T_{BKN} calculated with P_{BKN} for garnet bearing samples and P_{KB}, P_{INT} for spinel bearing samples. 2σ uncertainty level for $T_{Ca\ in\ opx}$.

Again, pressure or temperature were held constant to circumvent any effects caused by these variables. Recognizing differences in calculated P-T's using the core and rim compositions is essential in understanding the thermal history of the Torrie samples because transient thermal conditions may be recorded in the rim compositions that are not recorded by the core compositions.

This procedure showed that only four samples, TQY94-17-15A (15A), TQY94-17-22B2 (22B2), TANQ93-2-44B (44B) and TANQ93-1-39 (39) yield significant deviations in calculated temperatures using the core and rim data as input parameters (fig 4.6). Clinopyroxene rims in these four samples are enriched in Ca relative to the core compositions. The source of this chemical heterogeneity is unknown but may be due to interaction of clinopyroxene with melt at a late stage in the mantle, prior to entrainment in the host kimberlite. The increased Ca content of clinopyroxene rims lead to lower calculated temperatures. Thus the "rim" temperatures may be artificially lowered by metasomatic processes rather than representing real thermal perturbations. Sample 15A is a porphyroclastic sample that will be discussed in more detail in chapter 5.

The procedure described above also reveals that there are no significant variations in estimated pressures ($\Delta P_{BKN} = P_{core} - P_{rim}$) using the core and rim data as input parameters (fig 4.7). There are, however, rather large discrepancies in estimated pressures using P_{KB}. These discrepancies are most likely attributable to analytical uncertainty for Ca in olivine (± 8 ppm, 1σ) which exists in only trace amounts (i.e. < 30 ppm), and the strong temperature dependence associated with this geobarometer (Brey and Köhler, 1990).

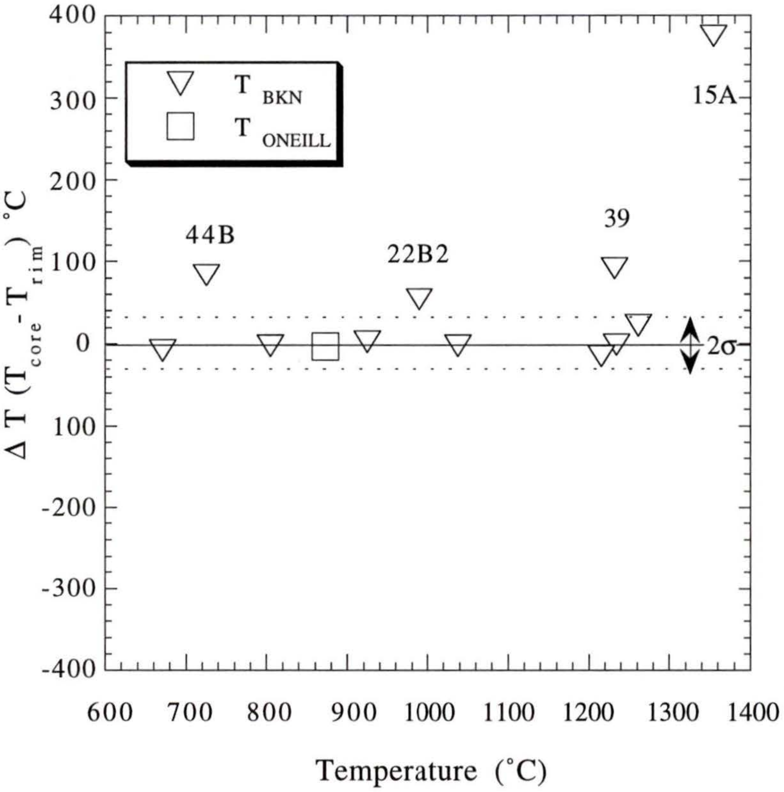

Figure 4.6: Differences in calculated temperatures using the core and rim compositions as input parameters (core-rim) at a constant pressure (5 GPa and 2 GPa at P_{BKN} for gt-bearing samples and T_{BKN} at P_{KB} and T_{BKN} at P_{INT} for spinel-bearing samples, respectively) plotted against temperature calculated iteratively using T_{BKN} (triangles) and T_{ONEILL} (square). Note variations in calculated temperatures in samples TQY94-17-15A (15A), TQY94-17-22B2 (22B2), TANQ93-2-44B (44B) and TANQ93-1-39 (39). 2σ uncertainty level for T_{BKN}.

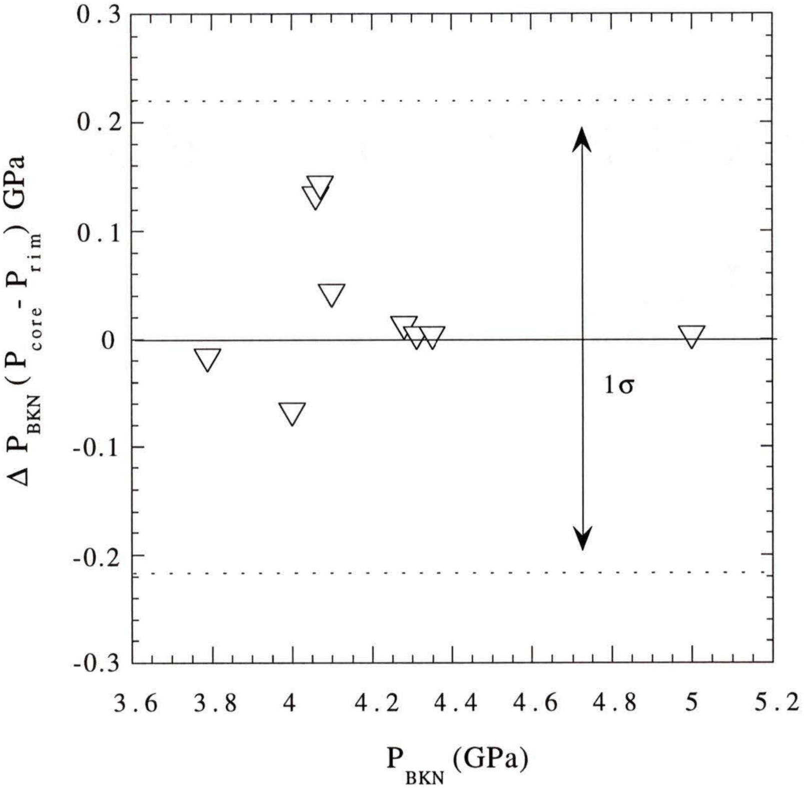

Figure 4.7: Differences in calculated pressures (ΔP_{BKN}) using the core and rim compositions as input parameters (core-rim) at a constant temperature of 1000°C and 800 °C for gt- and sp-bearing samples where orthopyroxene and clinopyroxene are present , respectively, plotted against P_{BKN} calculated for the core compositions. The results indicate no significant deviation in calculated pressures using the core and rim compositions as input parameters.

Table 4.2 summarizes the calculated P-T's for the Torrie xenolith suite which best represent ambient P-T conditions of equilibration. Boyd (1987) noted that suites of garnet peridotite xenoliths from southern Africa tend to form in two distinct groups that differ with respect to equilibration temperatures. "Low temperature" samples have equilibration temperatures < 1100 °C whereas "high temperature" samples have equilibration temperatures in excess of 1100 °C. Low temperature xenoliths are the most abundant of these two groups and Boyd (1987) notes that there is commonly a gap in P-T space between these two groups, a phenomenon which is also observed in the Torrie suite (fig 4.8).

There are also compositional, modal and textural differences between the two suites (Boyd, 1987). Typically, low temperature xenoliths are coarse grained, contain coarse phlogopite and are more depleted in basaltic components (Fe, Al, Ti). Conversely, high temperature xenoliths are finer grained, often porphyroclastic and are less depleted in basaltic components relative to the low temperature samples (Boyd, 1987).

The Torrie xenolith suite contains both low and high temperature coarse grained xenoliths although porphyroclastic xenoliths are exclusively high temperature. These porphyroclastic samples are also less depleted (as reflected in lower olivine Mg#) generally, than the coarse grained counterparts. Also, coarse phlogopite is restricted to low temperature xenoliths in the Torrie suite. Overall, the Torrie suite is similar in these regards to comparable cratonic xenolith suites from southern Africa. This observation suggests that cratonic mantle lithosphere is similar texturally and thermally on a global scale.

Figure 4.9 is a plot showing the array of calculated equilibrium P-T conditions recorded by the Torrie xenolith suite in Table 4.2. The P-T array define a geothermal gradient of ~ 6°C/km. Also shown is the position of the diamond graphite transition of Kennedy and Kennedy (1976). The combination of T_{BKN}-P_{BKN} was used for the garnet

Table 4.2: Summary of best P-T estimates for the Torrie xenoliths.

Sample	type	T (° C)	P (GPa)	P-T method
TQY94-17-15A	GL	1354	5.9	1
TANQ93-1-13	GH	1261	5.8	1
TQ9513B	GL	1234	5.7	1
TANQ93-1-39	GL	1232	5.5	1
TQY94-17-22B1	GL	1215	5.4	1
X9501B	GH	1065	4.8	2
TANQ93-2-45A	GM	1038	4.3	1
TQY94-17-22B2	SL	989	3.0	3
TANQ93-2-45	SL	925	3.4	4
X9501A	GH	911	3.8	2
TQY94-17-11	GH	873	3.5	2
TQY94-17-22F	SL	805	2.8	4
TANQ93-2-44B	OW	725	2.3	4
TANQ93-2-35A	OW	670	2.7	3

Rock types include garnet lherzolites (GL), garnet harzburgites (GH), spinel lherzolites (SL), garnet macrocryst (GM) and olivine websterites (OW). P-T methods include: T_{BKN}-P_{BKN} (1), T_{ONeill}- P_{BKN} (2), T_{BKN}-P_{KB} (3), T_{BKN}-P_{INT} (4)

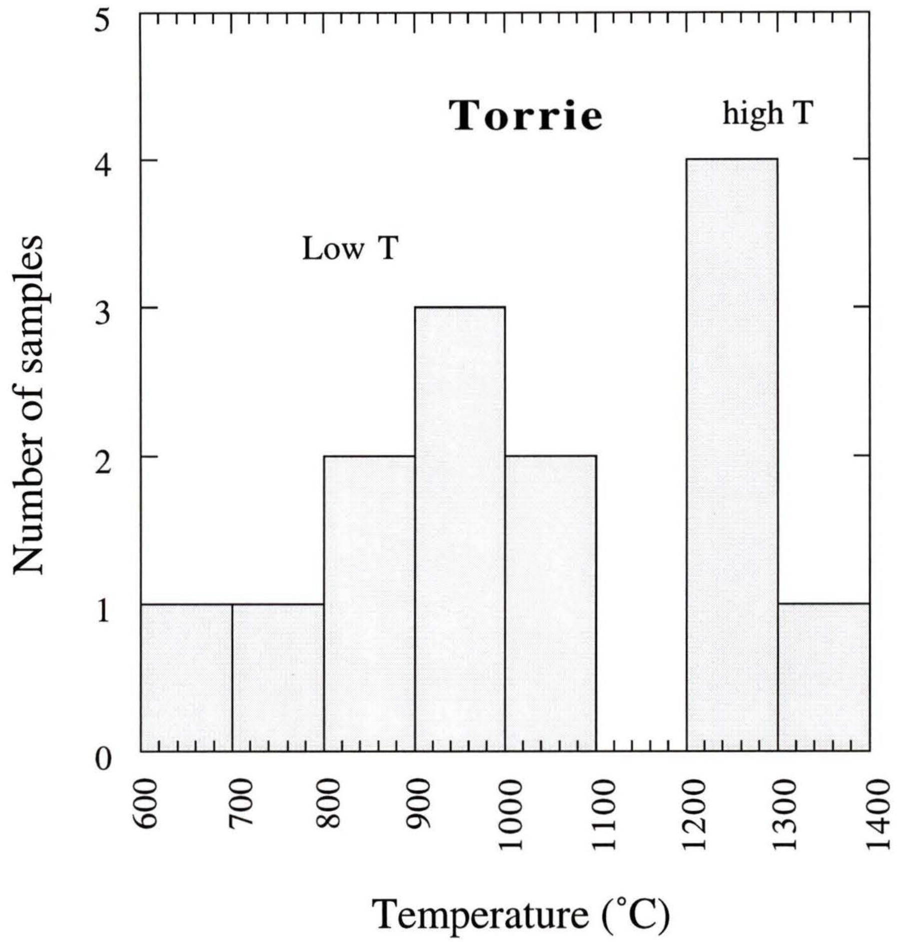

Figure 4.8: Distribution of calculated temperatures for the Torrie peridotite suite. Note the gap between low- and high temperature samples.

lherzolites, T_{ONeill}- P_{BKN} for garnet harzburgites,T_{BKN}-P_{KB} for spinel peridotites and T_{BKN}-P_{INT} for spinel peridotites where an appropriate geobarometer was not available (fig 4.1, table 4.2). A comparison of the P-T distribution for the Torrie samples calculated using different thermometers with P_{BKN} (and P_{KB} for spinel bearing samples) shows that although the absolute P-T values are dependent on the choice of thermobarometers used, the array of P-T conditions remains constant (fig 4.10). The lower temperatures recorded by Fe-Mg exchange thermometry between coexisting garnet and pyroxene (T_{KROGH}, T_{HARLEY}) may be indicative of cooling in the mantle (Smith and Barron, 1991) although calculated temperatures and pressures agree within error (2σ) to that calculated using T_{BKN}-P_{BKN}.

4.4 Summary

Based on the results of applied thermobarometry, the Torrie peridotites can be classified as both high temperature (> 1100°C) and low temperature (<1100°C) samples (Boyd, 1987). Similarities between low and high temperature xenoliths globally with the Torrie suite suggest that cratonic mantle is comparable in physical and thermal character in most cratonic areas. Additionally, calculated pressures indicate that the Torrie kimberlite sampled over 100 km of lithosphere beneath the central Slave craton. Convergence of different combinations of geothermobarometers indicate that the Torrie samples are homogeneous and represent chemical equilibrium under ambient mantle conditions, prior to entrainment and eruption to the surface. Calculated temperatures using core and rim compositions as input parameters show that four samples record lower temperatures in the rim compositions, of which three are attributable to metasomatism which artifially lowered calculated temperatures in the rim compositions. Additionally, the calculated P-T array for the Torrie suite provides an estimate of ~6°C/km for the geothermal gradient at the time of kimberlite magmatism.

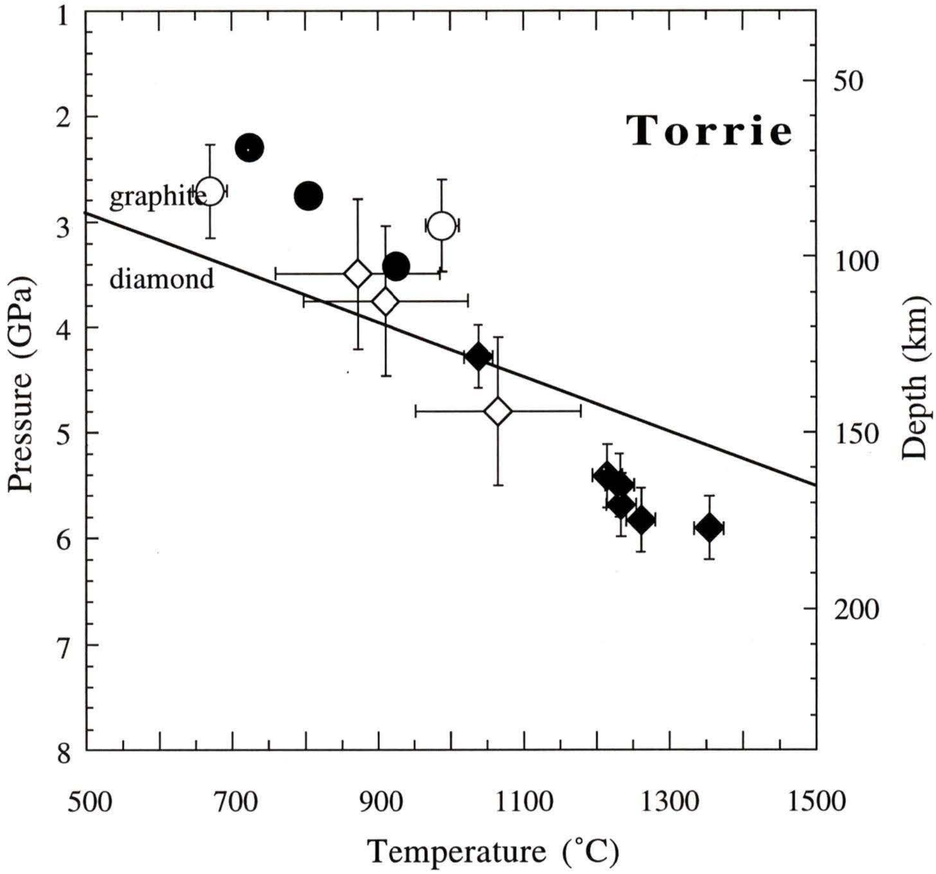

Figure 4.9: Pressure-Temperature (P-T) plot showing the positions of calculated equilibrium conditions for the Torrie xenoliths using T_{BKN}-P_{BKN} for Gt lherzolites (solid diamonds), T_{ONEILL}-P_{BKN} for Gt harzburgites (open diamonds), T_{BKN}-P_{KB} for Sp lherzolites (open circles) and T_{BKN}-P_{INT} for Sp peridotites (solid circles). Diamond-graphite transition after Kennedy and Kennedy (1976). Error bars are calculated at 1σ.

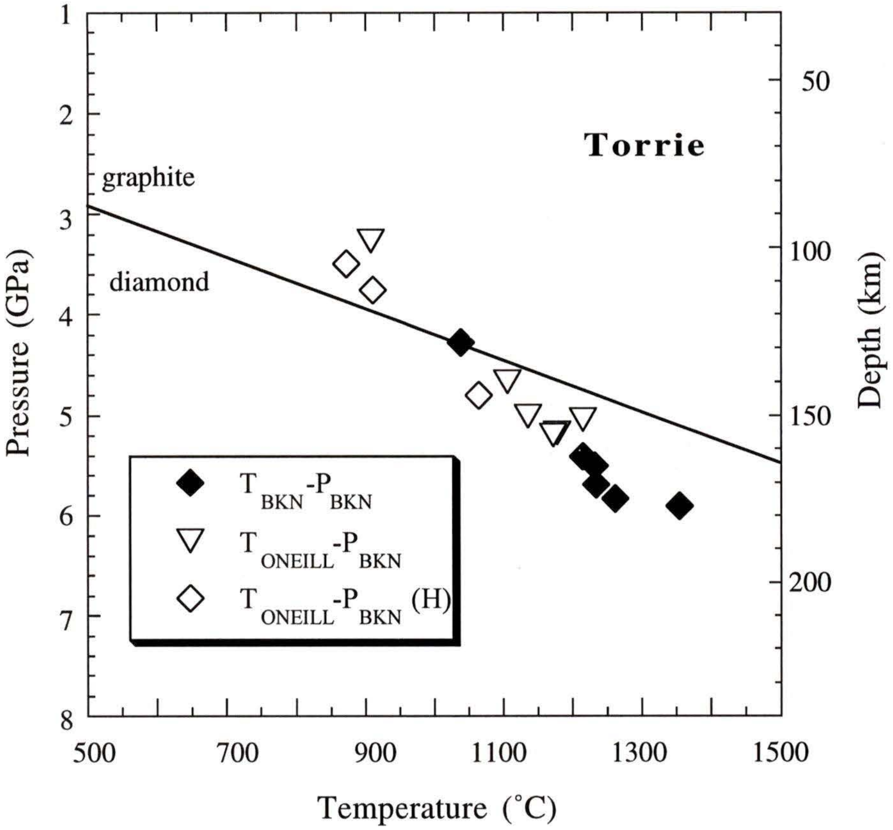

Figure 4.10: P-T plot comparing the distribution of equilibration conditions recorded by the Torrie suite using T_{ONEILL}-P_{BKN} (open diamonds (harzburgite -H-)/triangles) and T_{BKN}-P_{BKN} (solid diamonds). Diamond-graphite transition after Kennedy and Kennedy (1976). Notice that although the absolute P-T values are dependent on the choice of thermobarometer used, the array remains constant. P-T estimates, however, are consistiently offset ~1 GPa and 120-150 ˚C using T_{ONEILL}-P_{BKN} and T_{BKN}-P_{BKN} possibly reflecting differences in closure temperatures for ol-gt and 2-pyx equilibria respectively.

CHAPTER 5

THERMAL STRUCTURE

5.1 Geotherms and surface heat flow

Geotherms refer to the change in temperature with depth in the Earth and typically have a characteristic surface heat flow ascribed to them. The global average surface heat flow for both oceanic and continental regions is ~60 mWm^{-2} (Pollack and Chapman, 1977). The contributions to surface heat flow may be divided into three components: 1) heat from radioactive decay of heat producing elements (U, Th, K), 2) heat conducted through the lithosphere derived from the underlying convecting mantle and 3) "orogenic" heat transported convectively from magmas and fluids that penetrate the lithosphere during orogenic events (Rudnick et al., 1998).

Surface heat flow in oceanic regions is mainly supported by heat conducted through the lithosphere. The surface heat flow in oceanic regions decreases with the age, thickness of the plate and distance from the ridge axis. Heat produced within oceanic plates is comparably small relative to continental plates because the concentrations of heat producing elements in oceanic crust are much lower than that of continental crust. In continental regions, the mean surface heat flow for stable Proterozoic regions is 55 $mWm^{-2} \pm 17$ (1σ of mean) whereas the mean surface heat flow in Archean cratons is 41$mWm^{-2} \pm 12$ (1σ of mean) (Rudnick et al., 1998). Nyblade and Pollack (1993) suggest that the lower surface heat flow in Archean cratons may be the result of lower heat production in their crust or may result from refraction of heat due to the presence of thick mantle roots effectively deflecting heat derived from below away from central cratonic regions to bordering orogenic belts which generally have higher surface heat flow values. Regardless, surface heat flow in stable Archean cratons appears to be supported by a combination of heat conducted through the lithosphere derived from the underlying mantle and heat produced within the lithosphere. Since, by definition, cratons are long-lived stable regions, contributions to surface heat flow from orogenic events may be ignored.

Assumptions that need be made in geotherm modeling include the distribution of heat producing elements with depth in the lithosphere and the change in thermal conductivity with depth. Pollack and Chapman (1977) calculated a family of geotherms for continental areas using a model of steady state conduction, estimates of thermal conductivity after Schatz and Simmons (1972) (eqn. 6) and heat generation that decreases exponentially to ~8 km depth, with upper crust heat production of 2.5 μWm^{-3}. Comparing their calculated geotherms with the Torrie P-T array at depth indicates that the Torrie P-T array corresponds to a geotherm with a surface heat flow of approximately 40 mWm^{-2} (fig 5.1), similar to average surface heat flow values from Archean cratons (Rudnick et al., 1998).

Rudnick et al. (1998) have shown, however, that P-T arrays at depth may be consistent with a number of surface heat flow values depending on the assumptions made about the thickness and heat producing properties of the lithosphere. By far the most important parameter in modeling surface heat flow in continental regions is the contribution of heat generated within the lithosphere, in particular, the crust.

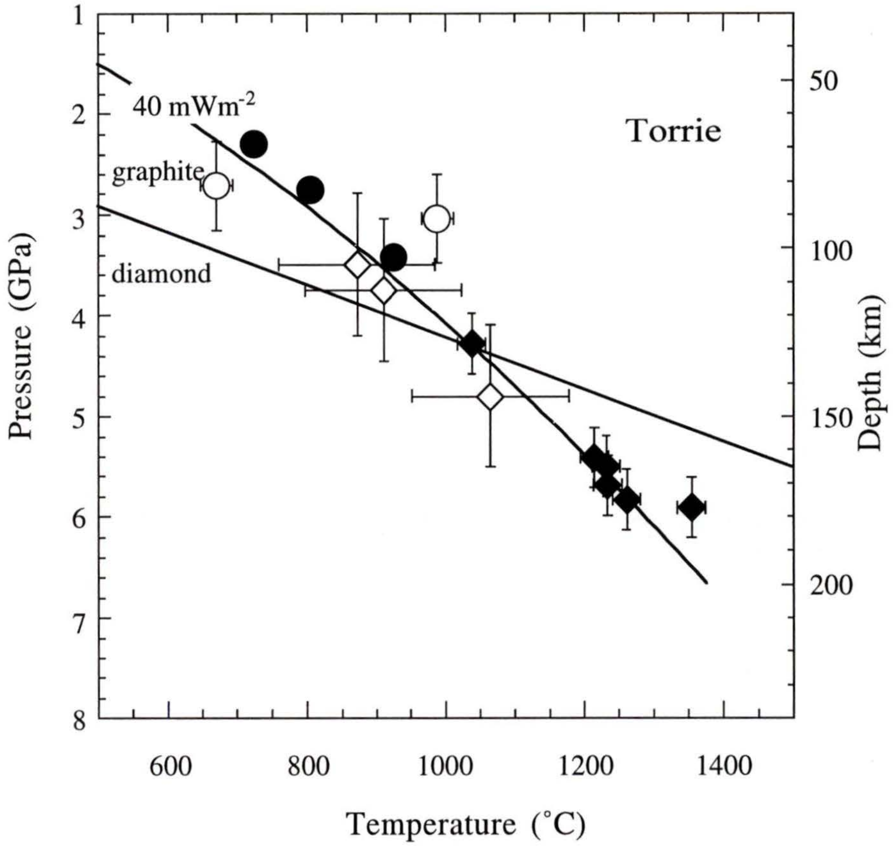

Figure 5.1: Pressure-Temperature (P-T) plot showing the 40 mWm^{-2} continental geotherm of Pollack and Chapman (1977) and the positions of calculated equilibrium conditions for the Torrie xenoliths using T_{BKN}-P_{BKN} for Gt lherzolites (solid diamonds), T_{ONEILL}-P_{BKN} for Gt harzburgites (open diamonds), T_{BKN}-P_{KB} for Sp lherzolites (open circles) and T_{BKN}-P_{INT} for Sp peridotites (solid circles). Diamond-graphite transition after Kennedy and Kennedy (1976). P-T estimates for the Torrie xenoliths are from table 4.2 Error bars are calculated at 1σ.

In an extensive review regarding the thermal structure and composition of continental lithosphere, Rudnick et al. (1998) have placed constraints on the maximum and minimum values for heat production in Archean lithosphere. In their work, maximum bulk crustal heat productions were constrained by the intersection of the 41 mWm^{-2} geotherm with the mantle adiabat. This intersection was judged by Rudnick et al. (1998) to represent the base of the thermal lithosphere. Rudnick et al. (1998) deemed estimates of bulk crustal heat production acceptable if this intersection was less than or equal to seismic estimates of maximum lithospheric thickness (i.e. < 400 km). Using this constraint, the authors provide a limit for the maximum heat generation value of bulk Archean continental crust as ≤ 0.77 μWm^{-3} assuming no heat generation in the mantle. Rudnick et al. (1998) indicate that this value is an upper limit because heat production in cratonic mantle will give rise to thicker lithosphere and a lower maximum bulk heat production in the crust. For example, if the heat production in cratonic upper mantle is 0.03 μWm^{-3}, the maximum bulk crustal heat production would be lowered to ~0.67 μWm^{-3}. Rudnick et al. (1998) estimate the minimum heat production in Archean crust is 0.4 μWm^{-3} based on the average heat production of Archean granulite terrains.

5.2 Paleogeotherm for the central Slave

Using the constraints outlined in Rudnick et al. (1998), a late Cretaceous-early Paleocene paleogeotherm for the central Slave craton was constructed using the Torrie P-T array. The geotherm was modeled using the equation of Chapman (1986) for one dimensional heat conduction in the lithosphere:

$$T(z) = T_T + \frac{q_T}{k} z - \frac{Az^2}{2k} \qquad (6)$$

where T = temperature at depth (z), T_T = temperature z=0, q_T = heat flow at z=0, A = volumetric heat production (μWm^{-3}), and k = thermal conductivity ($Wm^{-1}K^{-1}$).

Schatz and Simmons (1972) measured the total thermal conductivities (both lattice and radiative) of polycrystalline forsterite rich olivine and enstatite compositions to 1900 °K and found that thermal conductivity varies as a function of both temperature and, subsequently, depth within the lithosphere. Using their data, the change in thermal conductivity with depth was fitted by Ganguly et al. (1995) to a model equation (eqn. 6) with k = 2.5 at z < 30 km and:

$$k = 3.10 - 1.4x10^{-2}(z) + 2.18x10^{-4}(z^2) - 5.34x10^{-7}(z^3) \qquad (7)$$

at z > 30 km. Equation 6 was used in modelling the Torrie P-T array.

The results of the geotherm modeling are shown in figure 5.2 and indicate that the Torrie P-T array is best described by a paleogeotherm having a corresponding surface heat flow of 42 mWm^{-2} with a bulk crustal heat production of ~ 0.6 μWm^{-3}, similar to average surface heat flow values in the Archean Superior Province (Pinet et al., 1991) and most other Archean cratons globally (Rudnick et al., 1998). Additionally, our calculated surface heat flow agrees well with the 40 mWm^{-2} surface heat flow model geotherm for the central Slave Province of Thompson et al. (1996).

The only existing surface heat flow measurement for the Slave craton, measured near Yellowknife, is 53 ± 2 mWm^{-2} (Lewis and Wang, 1992). This surface heat flow

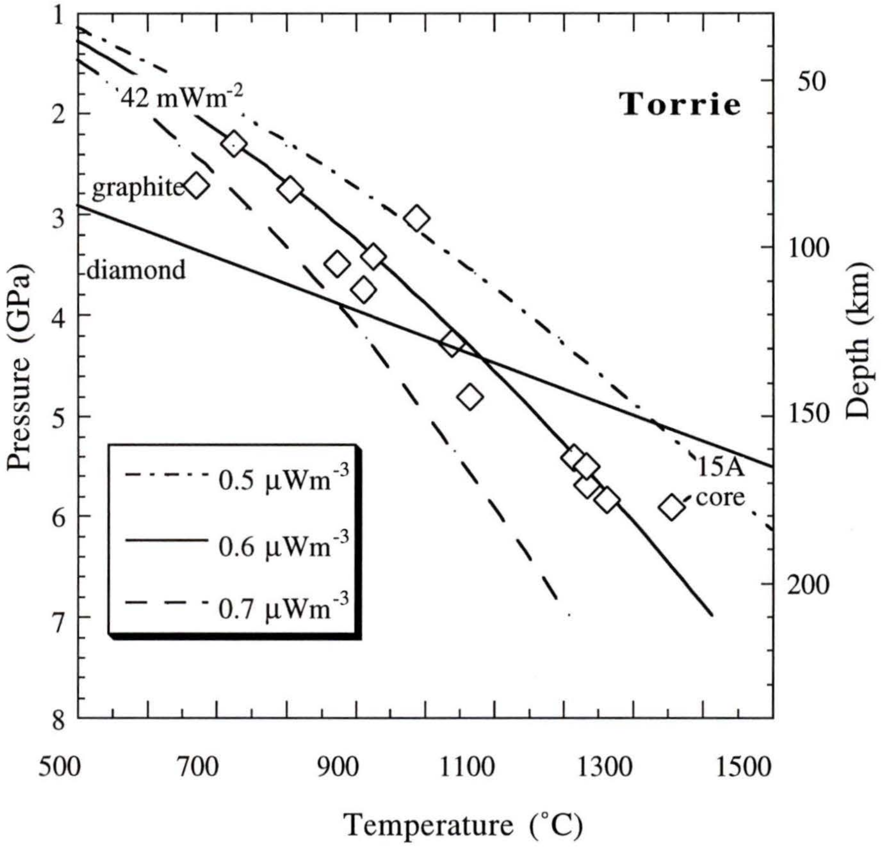

Figure 5.2: P-T plot for the Torrie peridotites and the positions of geotherms assuming bulk crustal heat productions of 0.5, 0.6, 0.7 μWm^{-3} and a surface heat flow of 42 mWm^{-2} Note the position of sample TQY94-17-15A (15A). Diamond graphite transition after Kennedy and Kennedy (1976). P-T estimates for the Torrie xenoliths are from table 4.2, errors in P-T estimates shown in figs. 4.9 and 5.1 and are listed in Table 4.1.

is not consistent with the Torrie P-T array at depth. Figure 5.3 illustrates that, by keeping the surface heat flow constant at 53 mWm^{-2}, the Torrie P-T array cannot be matched to any of the bulk crustal heat production values (i.e. 0.5, 0.6, 0.7 μWm^{-3}) characteristic of typical Archean crust (Rudnick et al., 1998). A surface heat flow of 53 mWm^{-2} in the central Slave craton would require a bulk crustal heat production of ~1 μWm^{-3}, a value that is greater than the maximum heat production of Archean crust noted by Rudnick et al. (1998). Consequently, the surface heat flow measured at Yellowknife may either not be representative of the surface heat flow during the late Cretaceous-early Paleocene, or may not reflect the heat flow in the central part of the craton because the heat flow measurement is near the Slave craton boundary as represented in the surface geology (fig 1.1). Alternatively, the rocks may be as "hot" as 1 μWm^{-3} consistent with the atypical nature of the Slave crust. Presently, the bulk composition of the Slave crust remains unknown.

Some notable outliers from the Torrie paleogeotherm may record a markedly different thermal history. Porphyroclastic sample TQY94-17-15A (figs 5.2, 5.3) records a P-T condition, using the core compositions, that lies above the ambient geotherm recorded by the remainder of the samples. The rim compositions for this sample record a much lower temperature (~250°C lower) and lie on the geotherm similar to the other Torrie samples. Chemically, clinopyroxene rims in this sample show an increase in Ca and decrease in both Na and Mg. The cause of this chemical heterogeneity may be due to interaction of clinopyroxene with melt in the mantle shortly before entrainment in the host kimberlite. The high Ca in clinopyroxene rims in this sample produce lower calculated temperatures for the rim compositions of TQY94-17-15A but do not necessitate a cooling effect. Indeed, this sample may have initially been on the 42 mWm^{-2} geotherm followed by a transient perturbation which texturally and thermally re-equilibrated it, as recorded in the core compositions. After the termination of this thermal event, metasomatism prior to kimberlite entrainment may have overprinted the rim compositions.

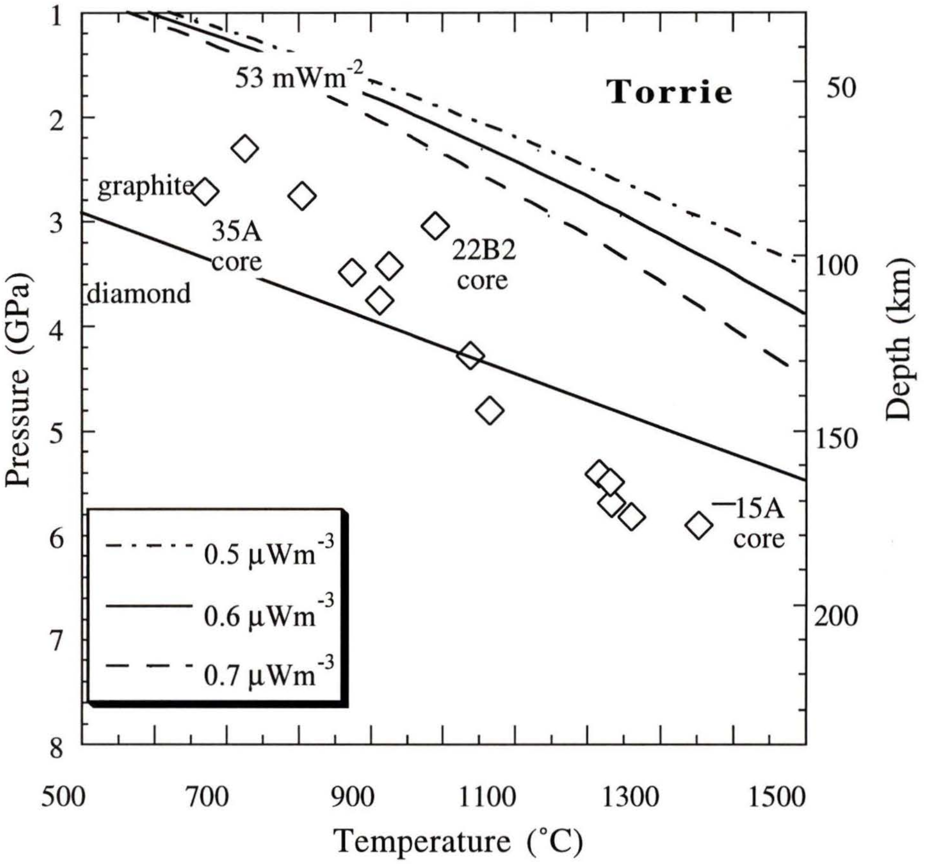

Figure 5.3: P-T plot for the Torrie peridotites and the positions of geotherms assuming bulk crustal heat productions of 0.5, 0.6, 0.7 μWm^{-3} and a surface heat flow of 53 mWm^{-2} Note the position of samples TQY94-17-15A (15A), TQY94-17-22B2 (22B2) and TANQ93-2-35A (35A). Diamond graphite transition after Kennedy and Kennedy (1976). P-T estimates for the Torrie xenoliths are from table 4.2, errors in P-T estimates shown in figs. 4.9 and 5.1 and are listed in Table 4.1.

The two spinel peridotite samples, TQY94-17-22B2 and TANQ93-2-35A (calculated using T_{BKN}, P_{KB}) also plot both above and below our calculated 42 mWm^{-2} geotherm (figs. 5.2, 5.3). This is likely a consequence of analytical uncertainty for Ca in olivine (± 8 ppm, 1σ). P-T's for the remaining spinel peridotites were calculated using the intersection of calculated temperatures with the geotherm based on samples for which both P and T were available (see chapter 4 for discussion of method).

Figure 5.4 shows a suite of calculated geotherms using P-T arrays for peridotite xenoliths from the Torrie, Jericho, and Grizzly pipes (see fig 1.2). The Jericho and Grizzly P-T arrays lie along a cooler paleogeotherm and, like the Torrie P-T array, cannot be fit to a surface heat flow of 53 mWm^{-2} using the values for bulk crustal heat production predicted by Rudnick et al. (1998) for typical Archean continental crust (Fig 5.4).

These observations could suggest that the Slave lithosphere has warmed since the Jurassic to the present day heat flow measured at Yellowknife (~53 mWm^{-2}; Lewis and Wang, 1992). The apparent warming of the Slave lithosphere could be due to lithospheric thinning promoting an increased contribution to heat flow from the convecting asthenosphere. This interpretation, however, is not supported by seismic tomography (Bostock, 1997) or magnetotellurics (Jones and Ferguson, 1997), which show more than 200 km of lithosphere beneath the Slave craton today. Instead, the latter studies require that any variation in heat flow between localities would have to be accommodated by regional variations in radiogenic heat production, thermal conductivity, or crustal thickness. Interestingly, many late K-rich granitoids which comprise the upper crust of the Slave craton, including the suite intruded by the Torrie kimberlite, have heat production as high as 5 to 15 μWm^{-3} (Thompson et al., 1995; 1996) implying that the high surface heat flow measured at Yellowknife (~53 mWm^{-2}; Lewis and Wang, 1992) is mainly supported by

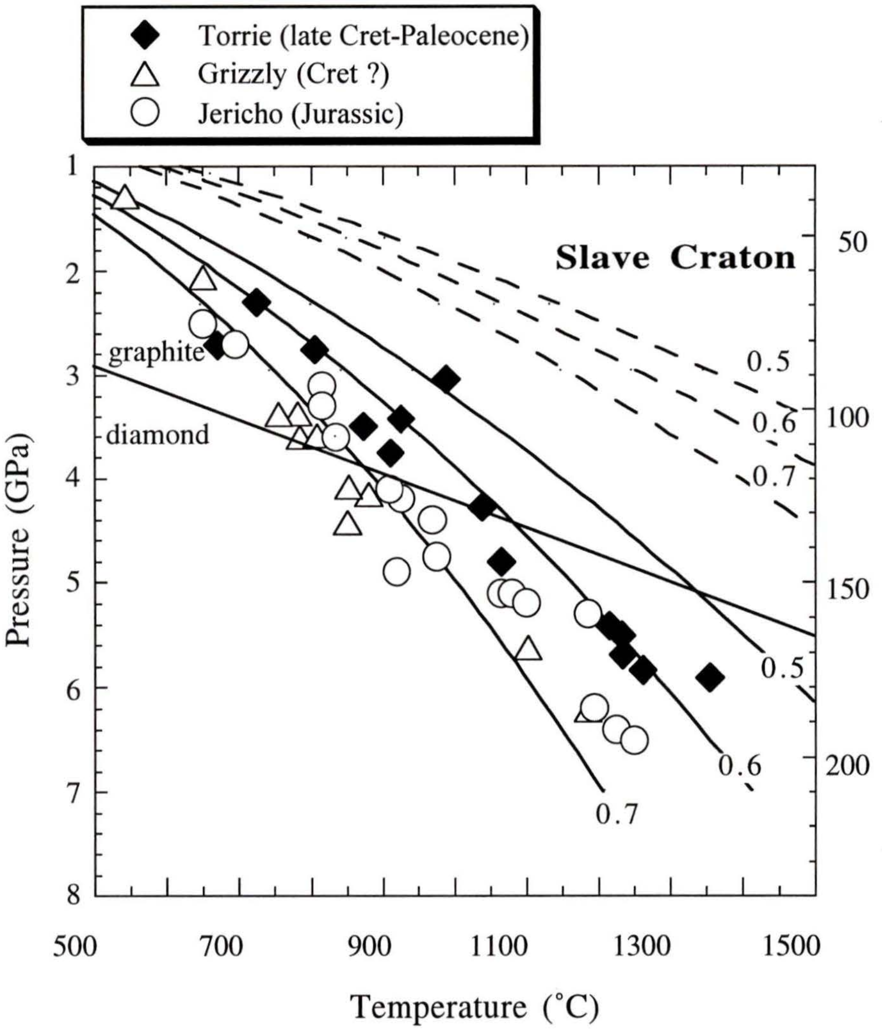

Figure 5.4: Calculated geotherms with varying bulk radiogenic heat production (μWm^{-3}) and surface heat flow values as described in figure 5.2 and 5.3 (dashed lines = $53mWm^{-2}$, solid lines = $42mWm^{-2}$) compared with P-T arrays for kimberlite-hosted peridotite, pyroxenite and macrocryst xenoliths from the Torrie, Jericho and Grizzly pipes. P-T combinations include: T_{BKN}-P_{BKN} for samples from this study and the Jericho pipe (Kopylova et al. 1998) and T_{ONEILL}-P_{MC74} for samples from the Grizzly pipe (F.R. Boyd, pers. comm., 1998). Diamond-graphite transition after Kennedy and Kennedy (1976). P-T estimates for the Torrie xenoliths are from table 4.2, errors in P-T estimates shown in figs. 4.9 and 5.1 and are listed in Table 4.1.

highly radiogenic rocks at the surface, where the measured heat production in the upper crust is 2.3 μWm^{-3} (Thompson et al., 1996), and not necessarily thinner mantle lithosphere.

Alternatively, assuming a surface heat flow of 53 mWm^{-2}, differences in P-T arrays between Torrie, Jericho and Grizzly may be accommodated by different bulk crustal heat production beneath these areas. This interpretation, however, requires a bulk crustal heat production greater than 1 μWm^{-3} and is at odds with the estimate of maximum heat production of Archean continental crust noted by Rudnick et al. (1998).

5.3 Lithospheric thickness of the central Slave

The thickness of cratonic mantle is an essential parameter for understanding the development and geodynamics of cratons. Thermobarometry of kimberlite-hosted xenoliths and diamond inclusion studies have been the principal source of information concerning these issues (i.e. Richardson et al., 1990; Boyd et al., 1985; Nixon and Davies, 1987) as well as seismic studies (ie. Grand, 1987).

Using the maximum P-T conditions recorded by the Torrie xenoliths (Table 4.2, fig 5.2 and 5.3), the minimum lithospheric thickness for the central Slave craton during the late Cretaceous-early Paleocene is established to be approximately 180 km.

This thickness is similar to other lithospheric thickness estimates based on recent magnetotelluric (Jones and Ferguson, 1997) and seismic (Bostock, 1997) data which place the electrical/seismic lithosphere-asthenosphere transition at ~200-250 km and ~195 km, respectively. Kopylova et al. (1998) estimate a lithospheric thickness of 190 km based on the transition in P-T estimates between coarse and sheared xenoliths hosted in the Jurassic Jericho pipe located in the north-central Slave craton (fig 1.2). Additionally, P-T data for xenoliths from the Grizzly pipe (fig 1.2), require a minimum lithospheric thickness of ~190 km (Boyd and Canil, 1997).

Grotzinger and Royden (1990), using flexural analysis of the Kilohigok Basin (1.9 Ga), estimated an effective elastic thickness of the Slave craton of 12±4 km which, if correct, implies up to a fourfold decrease in geothermal gradient since the paleoProterozoic (~2 Ga). This implies that the Slave geothermal gradient was up to four times higher during the paleoProterozoic and if we assume that the base of the paleo lithosphere occurs at the intersection of this gradient with the mantle adiabat then the lithosphere must have been much thinner during this time. The Slave craton, therefore, may not have developed a cool "mantle root" zone until sometime after 1.9 Ga but before 538 Ma, the age for the oldest diamondiferous kimberlite in the Slave craton [5034 Pipe -Heaman et al., (1997)]. In contrast, Archean-aged diamonds present in some kimberlites from the Kaapvaal craton (Boyd et al., 1985) and eclogite xenoliths in some kimberlites from the Siberian craton (Pearson et al., 1995) indicate that these cratons had established deep, cool mantle roots by the end of the Archean. Thus, the time duration since the emergence of cool mantle roots, essential to stabilize diamond, may vary among cratons globally.

5.4 Summary

The array of P-T estimates from the Torrie xenolith suite define a late Cretaceous-early Paleocene paleogeotherm for the central Slave craton consistent with a surface heat flow of 42 mWm^{-2} and a bulk crustal heat production of ~ 0.6 μWm^{-3}. This estimate is similar to the average surface heat flow in Archean cratons (Rudnick et al., 1998) and is consistent with 40 mWm^{-2} surface heat flow model geotherm for the central Slave Province of Thompson et al. (1996). The measured surface heat flow at Yellowknife is 53 mWm^{-2} (Lewis and Wang, 1992). This surface heat flow cannot be matched by the Torrie P-T array at depth using bulk crustal heat production values consistent with average Archean crust (Rudnick et al., 1998) and would require a composition with heat production of ~ 1 μWm^{-3}, greater than Rudnick et al.'s (1998) estimate for typical Archean crust of 0.77

μWm^{-3}. The results reveal that the surface heat flow measured at Yellowknife may either not be representative of the surface heat flow during the late Cretaceous-early Paleocene, or the heat flow in the central part of the craton. During the late Cretaceous-early Paleocene at least 180 km of lithosphere was present beneath the central Slave craton.

CHAPTER 6

ORIGIN OF THE SLAVE MANTLE ROOT

6.1 Existing models

Cratonic "mantle roots" represent a major source of heterogeneity in the Earth's upper mantle as these roots are chemically and petrologically distinct from the "pyrolite" model composition (Ringwood, 1991) advocated by many to be representative of the upper mantle (Angel, 1997). Whereas oceanic peridotites have been interpreted in terms of melt extraction, the origin of cratonic peridotites has remained cryptic (Walter, 1998). The central issue surrounding the origin of cratonic peritotites is the coupling of high Mg# in olivine, with high orthopyroxene content (Walter, 1998) as both modal olivine and olivine Mg# should increase proportionally with increasing differientiation. Presently, there is no consensus concerning the emergence and growth of refractory cratonic upper mantle although several hypotheses have been forwarded invoking continental collision (Jordan, 1978), plume origin (Boyd, 1989; Walter, 1998; Herzberg, submitted) and tectonic stacking of oceanic plates through shallow subduction (deWit et al., 1992; Abbott, 1991; Hart et al., 1997).

The collisional model of Jordan (1978) proposes that the growth of continental lithosphere (termed tectosphere in Jordan, 1978) may be attributed to the shortening of formerly thin lithosphere, similar to the present day situation involving the collision of India and Eurasia in which the crust has thickened from ~40 to ~75 km due to shortening

(Abbott, 1991). If the crust is thickened to ~ 75 km, then high pressure, lower crustal, metamorphic rocks (granulites) should record conditions of metamorphism approaching 1.5-2.5 GPa (Abbott, 1991). Abbott (1991) advocates the unsuitability of this model due to the lack of Archean aged high pressure granulite xenoliths from the Kimberley pipe in the Archean Kaapvaal craton. Based on diamond inclusion isotopic dating, the lithosphere in this region has been shown to be Archean in age (Richardson et al., 1984). From the above observations, Abbott (1991) indicates that, since the Archean crust through which the Kimberley pipe intruded was not thickened by continental collision, the tectosphere must necessarily not have been formed through continental collision.

The plume model of Boyd (1989) and Herzberg (1997) advocates that cratonic upper mantle may have formed as high pressure residues resulting from the extraction of ultramafic liquids from the primitive Archean mantle ("pyrolite"). This hypothesis is supported by peridotite melting experiments which show increased orthopyroxene contents in residues after partial melting at high pressures (i.e. > 6 GPa) (Walter, 1998) and by comparisons of cratonic lithosphere with abyssal peridotites, ophiolites, alpine massifs and xenoliths from alkali basalts (Boyd, 1989) (fig 6.1).

Models involving shallow subduction propose that continental lithosphere formed as a result of intraoceanic tectonic stacking of oceanic plates. In this model, oceanic plates are progressively accreted to the base of an existing oceanic "kernel" (fig 6.2). DeWit et al. (1992) believe this process arose only when the elevation of mid-ocean ridges exceeded mean sea level. Evidence for this model (Abbott, 1991) includes: 1) the behavior of isotopic systems in mantle eclogites, 2) the occurrence of coesite in mantle-derived eclogites indicating basalt crystallization at crustal depths and, 3) seafloor hydrothermal alteration, rather than mantle metasomatism, being the likely source for carbon in diamond. Additionally, Hart et al. (1997) have shown that trace element ratios in silicate and sulphide inclusions in diamonds from southern Africa are similar to trace element ratios in MORB's.

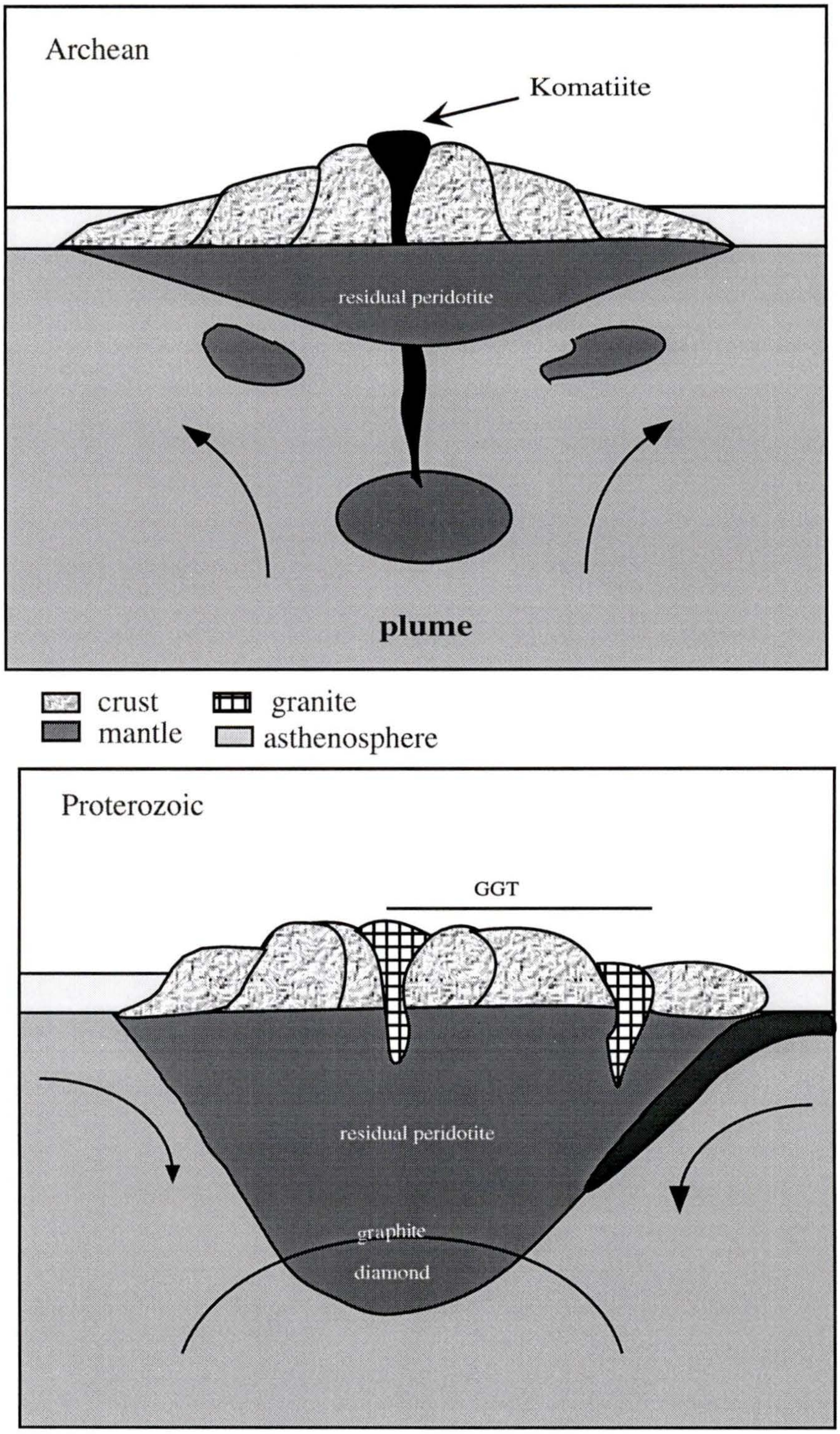

Figure 6.1: Plume model (after Hart et al 1997)
GGT = granite-greenstone terrain.

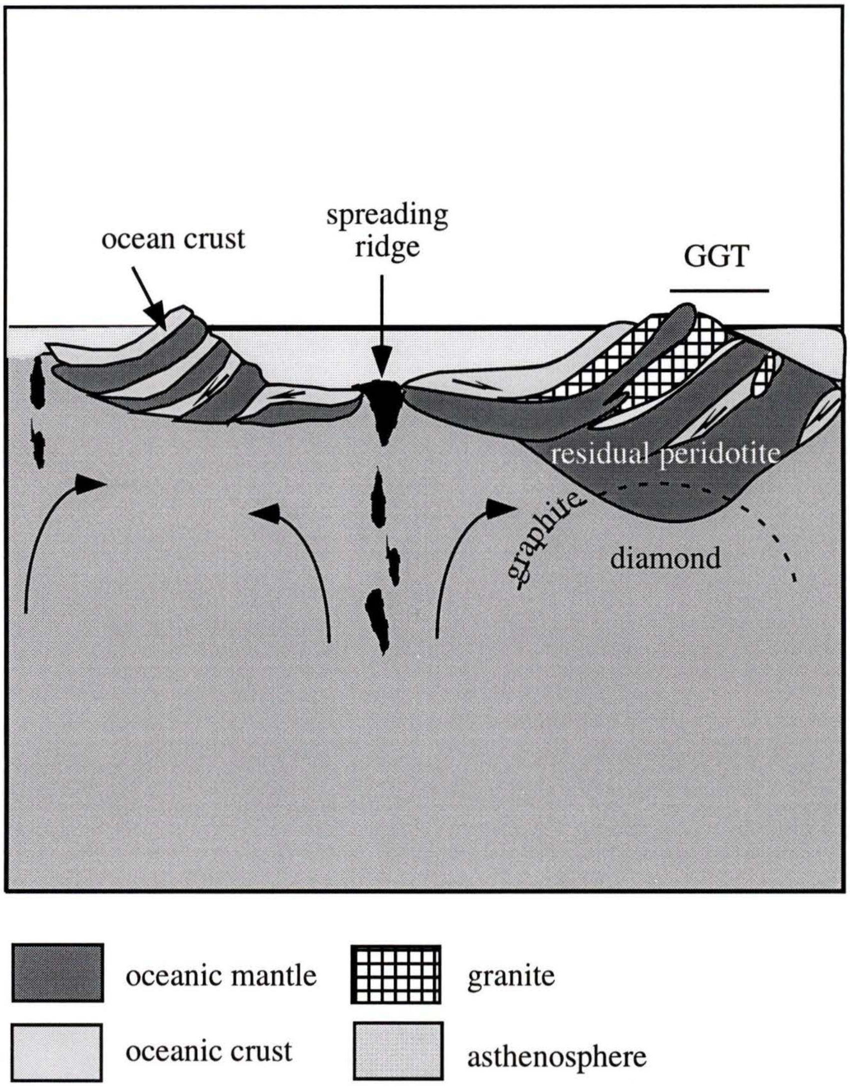

Figure 6.2: Shallow subduction model (after Hart et al 1997)
GGT = granite-greenstone terrain.

6.2 Evidence from the Torrie suite

The relationship between melt depletion and residual peridotite composition is shown in figure 6.3. The oceanic trend in figure 6.3 is the compositional trend from fertile lherzolite to depleted harzburgite defined by residues of lithosphere-forming processes at low pressures in orogenic belts and ocean basins (Boyd, 1989). Peridotites from the Torrie suite lie above this trend (fig 6.3), similar to cratonic peridotites from several localities in southern Africa and Siberia (Boyd, 1989; Boyd et al., 1997) reflecting their low modal abundance of olivine at a given degree of depletion as measured by the Mg# of olivine. The trend requires that cratonic xenoliths from the Torrie suite owe their provenance to some other process, in addition to being simply residues of melting. In contrast, peridotite xenoliths from the nearby Grizzly pipe cluster near the top of the oceanic trend (fig 6.3) indicating that they may have formed as low pressure residues similar to harzburgites from the Papua Ultramafic belt (Boyd, 1989). Differences between the two suites might possibly be due to variations in the degree of primary depletion, or secondary depletion associated with subduction or obduction in a trench environment (Boyd, 1989).

Modally, the Torrie xenoliths have average olivine and orthopyroxene contents of 58 wt% and 30 wt% whereas the Grizzly xenoliths average 86 wt% and 10 wt% respectively (Table 2.2). This difference may be due to a number of reasons. For example, the Torrie kimberlite may have sampled different stratigraphic levels than the Grizzly kimberlite but this interpretation is not supported by thermobarometric work which shows that both suites have sampled equivalent depths in the mantle. Alternatively, the differences in modal mineralogy may be due to lateral heterogeneities at a local scale (i.e. < 60 km) in the mantle. Finally, the two suites may possibly have formed as residues of different degrees of partial melting, or melting at variable pressures (Walter, 1998). Although the Torrie xenoliths are considerably more altered than those from Grizzly, figure 2.7 dictates

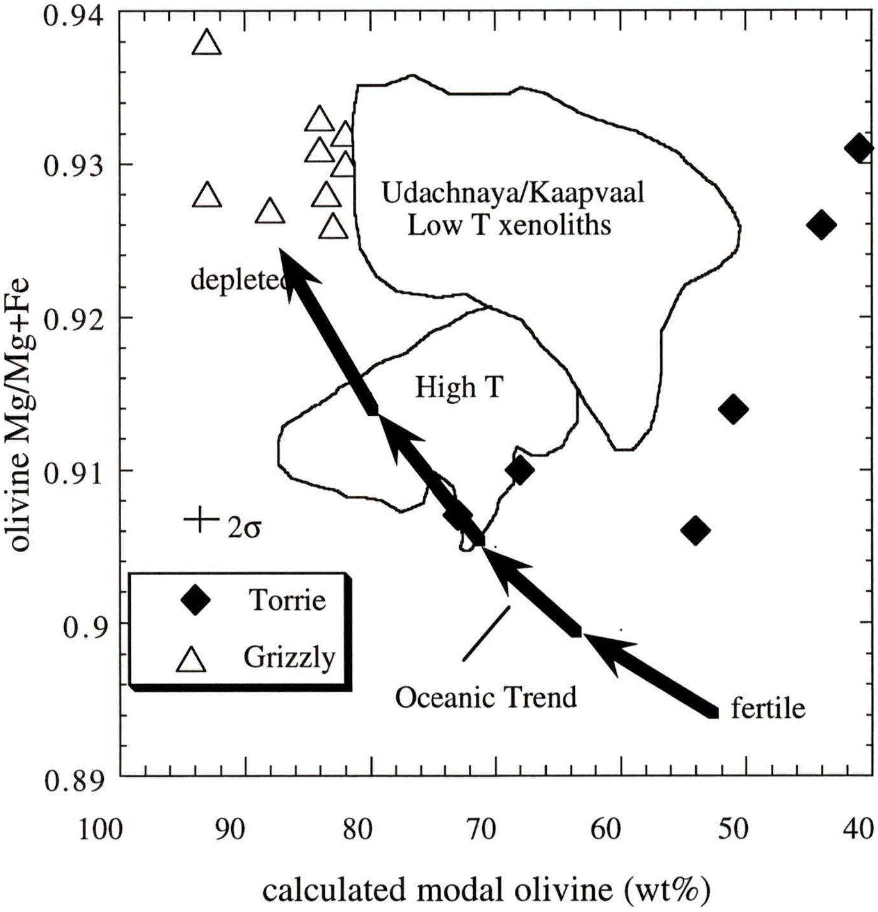

Figure 6.3: Olivine Mg# [Mg/(Mg+Fe)] vs. modal olivine for peridotites (> 40% modal olivine) from the Torrie (this study) and Grizzly (FR Boyd, pers. comm. 1998) pipes. The oceanic trend (arrows) after Boyd (1989). Kaapvaal and Udachnaya fields after Boyd (1989) and Boyd et al. (1997).

that alteration does not modify the primary modes and thus cannot be responsible for the modal variations between these two suites.

Modal data was combined with mineral chemistry in order to provide an estimate of bulk rock composition for the Torrie xenoliths. This method has the advantage of being independent of secondary metasomatic effects evident in many peridotite xenoliths (Boyd et al., 1997) but is sensitive to any mineralogical heterogeneity as described by Cox et al. (1987). The errors shown in figure 6.4 are the averaged 2σ standard deviations for all the Torrie peridotites. Because of the small size of the Torrie xenoliths and the large 2σ standard deviation associated with one spinel peridotite, this approach leads to large uncertainties for many oxides, but it should not obscure any trends amongst those oxides. Values for bulk FeO in the Torrie peridotites have a negative correlation with SiO_2 (fig 6.4) which crosses the olivine-orthopyroxene join calculated using the average compositions of the Torrie olivines and orthopyroxenes. Boyd et al. (1997) suggest that the preferential incorporation of Fe and Si into the melt phase will cause these elements to be positively correlated in both residues and cumulates. Walter (1998), based on melting experiments on Gt peridotite to 7 GPa, also supports this inference and indicates that the same relationship will hold for melting in both the spinel and garnet lherzolite field. Thus the observed negative trend is an enigma if the rocks are to represent residues of partial melting.

Boyd et al. (1997) have observed a similar negative trend in bulk rock FeO and SiO_2 in low-temperature peridotites from Udachnaya (fig 6.4) and proposed that this trend is difficult to reconcile in terms of simple melting relationships. Boyd et al. (1997) hypothesized that such a trend may reflect the physical segregation of olivine and orthopyroxene by either cumulate sorting, metamorphic differentiation or, conversely, by metasomatic replacement of olivine by orthopyroxene. Boyd (1997) found a positive correlation between NiO in olivine and modal orthopyroxene which may reflect SiO_2

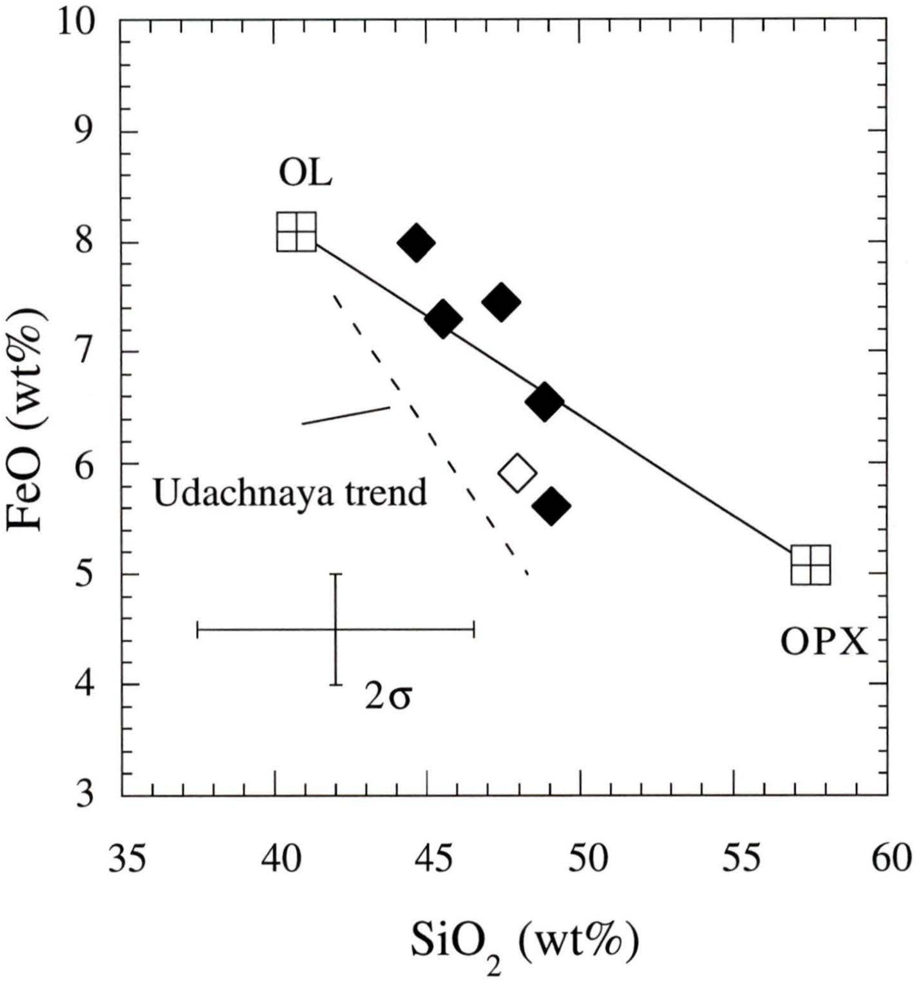

Figure 6.4: Bulk FeO vs. SiO$_2$ for Torrie Gt (solid diamonds) and Sp (open diamond) peridotites (> 40% modal olivine) calculated using individual modal and mineral chemical data. OL= average olivine composition, OPX= average orthopyroxene composition. Udachnaya trend after Boyd et al. (1997). Negative trend requires the physical segregation of olivine and orthopyroxene. Error bars calculated at 2σ.

enrichment of a high Mg# (Mg/Mg+Fe) protolith by reactions with small degree silicic melts from subducted eclogite (Kelemen et al., 1997). Alternatively, Herzberg (1997) has suggested that the higher NiO in olivines from orthopyroxene-rich peridotites is a requirement of equilibrium cooling.

This inference is a consequence of the temperature dependence of the partition coefficient $D_{NiO}^{ol/opx}$ which requires that NiO in olivine should be higher in peridotites with higher modal orthopyroxene (Herzberg, 1997). For example, for a given bulk Ni in a mixture of olivine and orthopyroxene, Ni will preferentially be incorporated into the olivine structure upon cooling. This effect should be more prominent in assemblages with high modal orthopyroxene as, upon cooling, Ni will be more strongly partitioned into the olivine structure in the presence of orthopyroxene.

The Torrie peridotites do not show a positive correlation of NiO (olivine) and orthopyroxene (fig 6.5) but reveal a relatively flat slope, similar to garnet and spinel peridotites from Kimberley, South Africa (Boyd, 1997). Data in figure 6.5 shows that the source of orthopyroxene enrichment observed in the Torrie xenoliths must be accommodated by processes other than reaction with Si-rich melts such as metamorphic differentiation or cumulate sorting. Alternatively, Boyd (1997) suggests that the flat slope for NiO (olivine) and modal orthopyroxene in the Kimberley suite may be a consequence of exchange of Ni between orthopyroxene-rich and orthopyroxene-poor peridotites under ambient mantle conditions. This inference may be supported by the Torrie and Grizzly suites which have very different orthopyroxene contents but similar NiO contents.

In the Kaapvaal craton, xenoliths from the Kimberley and Premier pipes have high orthopyroxene contents. The Kimberley suite does not have a positive correlation between NiO (olivine) and modal orthopyroxene whereas the Premier suite does show a positive correlation (Boyd, 1997). This observation may be due to local Si enrichment which has affected some regions of the Kaapvaal mantle but not others.

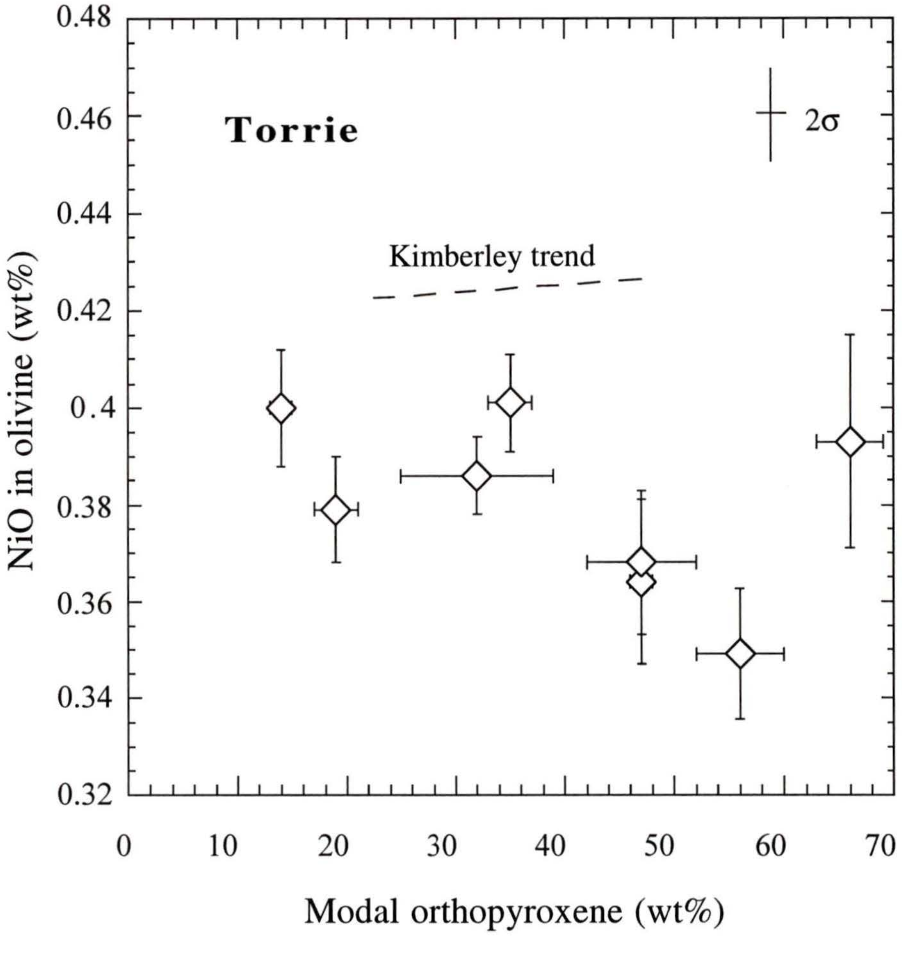

Figure 6.5: NiO in olivine vs. modal orthopyroxene for peridotites from the Torrie pipe. Also shown is the trend from Kimberely South Africa [dashed line (Boyd, 1997)].

This hypothesis could be validated for the Slave craton if the Torrie xenoliths, which are orthopyroxene rich but do not show a positive correlation between NiO (olivine) and modal orthopyroxene were compared to the Grizzly or Jericho xenoliths. Presently, NiO (olivine) data for the Grizzly and Jericho samples are unavailable and therefore this interpretation cannot be tested. Regardless, if Si enrichment in cratons is a widespread global phenomenon, it does not explain the dichotomy between the Torrie and Grizzly suites reviewed above, or the Kimberley and Premier suites, three of which are high in orthopyroxene, yet only Premier shows the positive correlation between NiO (ol) and modal orthopyroxene indicative of such enrichment (e.g. Kelemen et al., 1997).

6.3 Shallow subduction in the Slave craton

Bostock (1997a) has observed the seismic structure of the Slave craton using the coda of teleseismic P-waves recorded at Yellowknife (station **YKA**). In his study, Bostock (1997a) was able to delineate distinct anisotropy in the Slave lithosphere. In particular, strong reflectors, defined by converted P to S waves, were imaged at depths of 75, 135 and 195 km beneath the Slave.

Bostock (1997a) notes that the dipolar nature of the conversion at 75 km is indicative of two P-S conversions originating at the boundaries of a high velocity layer. Regarding the nature of the 135 km reflector, Bostock (1997a) suggests three possible sources: 1) phase transition from spinel to garnet in lherzolitic peridotite, 2) temperature controlled transition between diffusion and dislocation creep and 3) a structural origin associated with shallow subduction and underplating. The conversion at 195 km has been proposed to represent the base of the Slave lithosphere. Bostock (1997b) compared his results to recent *LITHOPROBE* seismic reflection profiles in the southern Slave craton (Cook et al., 1998) and found a consistent correlation between the reflection and teleseismic data.

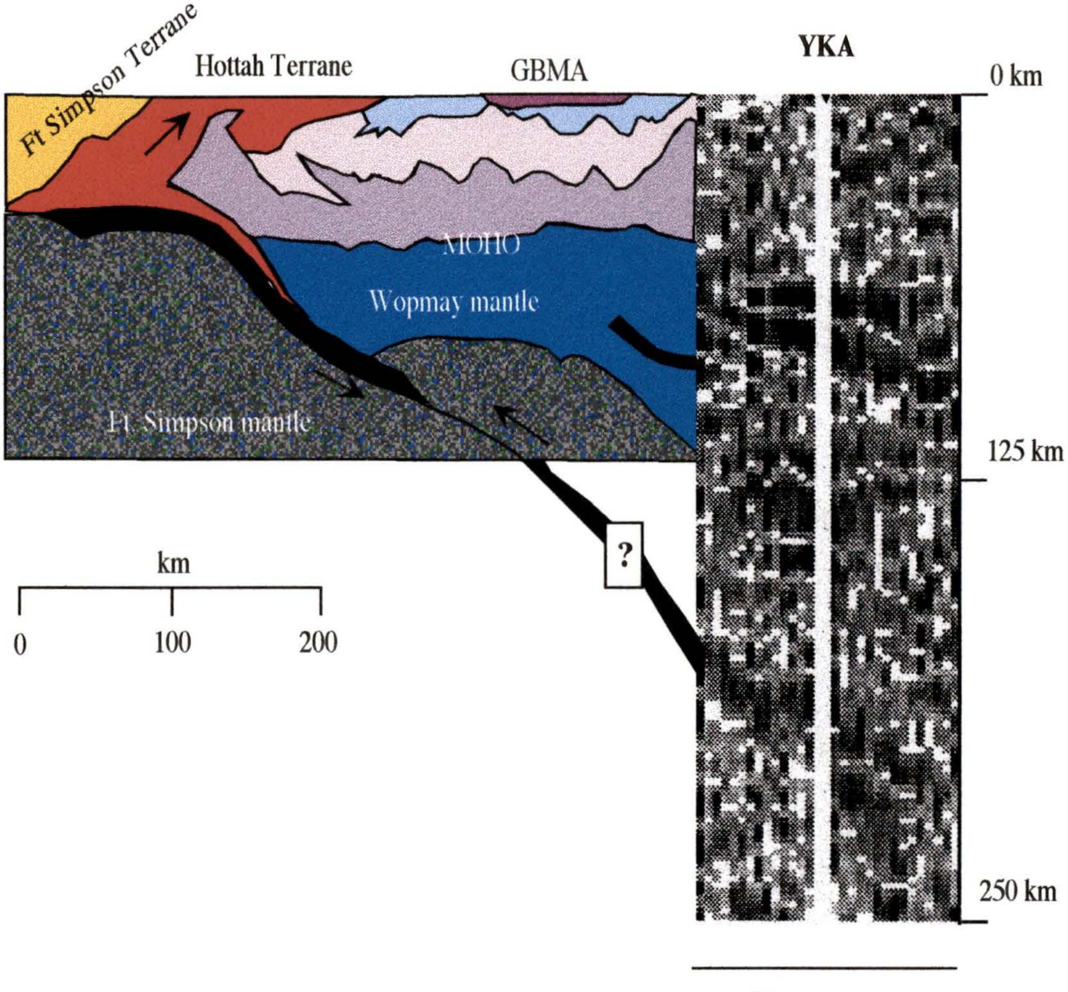

Figure 6.6: Schematic cross section of transition between Slave craton (right) to the younger Proterozoic terranes to the west (left). **YKA** = teleseismic station at Yellowknife. note correlation between *LITHOPROBE* reflection data and the teleseismic data both of which have been interpreted to image previously subducted slabs beneath the Slave craton and younger terranes to the west. GBMA = Great Bear magmatic arc. Dark greys in teleseismic data represent P-S wave conversions. Figure modified after Bostock (1997b).

This correlation is shown in figure 6.6 and supports the notion that discontinuities in the teleseismic data are structural in origin, possibly due to the imbrication of ancient subducted slabs beneath the Slave craton. These observations are compelling evidence that the Slave mantle root may have grown by processes involving shallow subduction and tectonic underplating. Accounting for the data revealed by the Torrie xenoliths, which record a residual history, the mantle beneath the central Slave craton may have developed initially as high pressure residua and grown through processes involving shallow subduction.

6.4 Summary

The Torrie xenolith suite reveal a history of development consistent with a plume model advocated by Boyd (1989) and Herzberg (1997). The Torrie suite represents residua remaining after the extraction of ultramafic liquids at high pressures (i.e. > 6 GPa). This residue has since been altered by metamorphic differentiation or cumulate sorting after primary crystallization to modify the original olivine/orthopyroxene ratio. Accounting for the seismic structure data of Bostock (1997 a,b) and *LITHOPROBE* (Cook et al., 1998), the mantle beneath the Slave craton may have developed initially as high pressure residua providing a "kernel" followed by tectonic underplating of oceanic lithosphere which facilitated the growth of cratonic mantle beneath the Slave. The similarities between the Torrie suite and kimberlite-hosted cratonic xenolith suites from southern Africa and Siberia (Boyd, 1989; Boyd et al., 1997) shown in figures 6.3 to 6.5 also reveals that cratonic upper mantle is similar in chemical composition and modal character on a global scale.

CHAPTER 7

CONCLUSIONS

7.1 Thermal state

As defined by the Torrie xenolith P-T array, the thermal state of the central Slave craton during the late Cretaceous-early Paleocene is consistent with a model paleogeotherm having a surface heat flow of 42 mWm^{-2} and a bulk crustal heat production value of ~0.6 μWm^{-3}. This value is similar to the average surface heat flow value for most Archean cratons (Rudnick et al., 1998) including the Superior Province (Pinet et al., 1991) and the model geotherm for the central Slave craton of Thompson et al. (1996). Xenolith P-T arrays from other kimberlites in the Slave craton describe a paleogeotherm with slightly lower surface heat flow values or may be explained assuming higher bulk crustal heat production values.

The only existing surface heat flow measurement in the Slave craton, measured near Yellowknife, is 53 mWm^{-2} (Lewis and Wang, 1992). Assuming a surface heat flow of 53 mWm^{-2} would require a bulk crustal heat production of ~1 μWm^{-3}, a value which exceeds Rudnick et al's (1998) estimate of maximum crustal heat production of 0.77 μWm^{-3}. Measurements of heat production near Yellowknife show heat productions in the upper crust in excess of 2 μWm^{-3} indicating that the higher heat flow measured at Yellowknife is supported by highly radiogenic rocks at the surface.

The array of P-T conditions recorded by the Torrie suite provide an estimate of the minimum lithospheric thickness in the late Cretaceous-early Paleocene of ~180 km, a value which is consistent with estimates from other xenolith suites in the Slave Province

(Kopylova et al., 1997; Boyd and Canil, 1997) and with present day seismic and magnetotelluric estimates of lithospheric thickness (Bostock, 1997; Jones and Ferguson 1997, respectively).

7.2 Craton development

The Torrie xenoliths are similar in texture, modal mineralogy and bulk chemistry to comparable cratonic xenolith suites from southern Africa and Siberia (Boyd and Mertzman, 1987; Boyd et al., 1997). Specifically, the Torrie xenoliths are enriched in modal orthopyroxene and have average olivine Mg# ratios of 0.920. The latter observations indicate that the mantle root beneath the central Slave may have formed as residues after the extraction of ultramafic liquid in tectonic regimes unlike those at modern-day spreading centres, possibly under higher P-T conditions. In conjunction with seismic evidence for subducted slabs beneath the Slave, a model is proposed in which cratonic lithosphere developed through initial separation from the primitive mantle as residues after extraction of ultramafic liquids, followed by subsequent tectonic underplating of oceanic slabs during the Proterozoic (fig 7.1). The Slave craton is unique from other Archean cratons in size and crustal composition, whereas the underlying mantle appears to be similar to cratonic mantle beneath other Archean regions globally, suggesting that processes involved in the formation of Archean crustal sequences may be isolated from those responsible for the formation of the underlying mantle.

Grotzinger and Royden (1990), using flexural analysis of the Kilohigok Basin (1.9 Ga), estimated an effective elastic thickness of the Slave craton of 12±4 km which, if correct, implies up to a fourfold decrease in geothermal gradient since the paleoProterozoic (~2 Ga). The Slave craton, therefore, may not have developed a cool mantle root until sometime after 1.9 Ga but before 538 Ma, the age for the oldest diamondiferous kimberlite in the Slave craton [5034 Pipe -Heaman et al. (1997)]. In contrast, Archean-aged diamonds

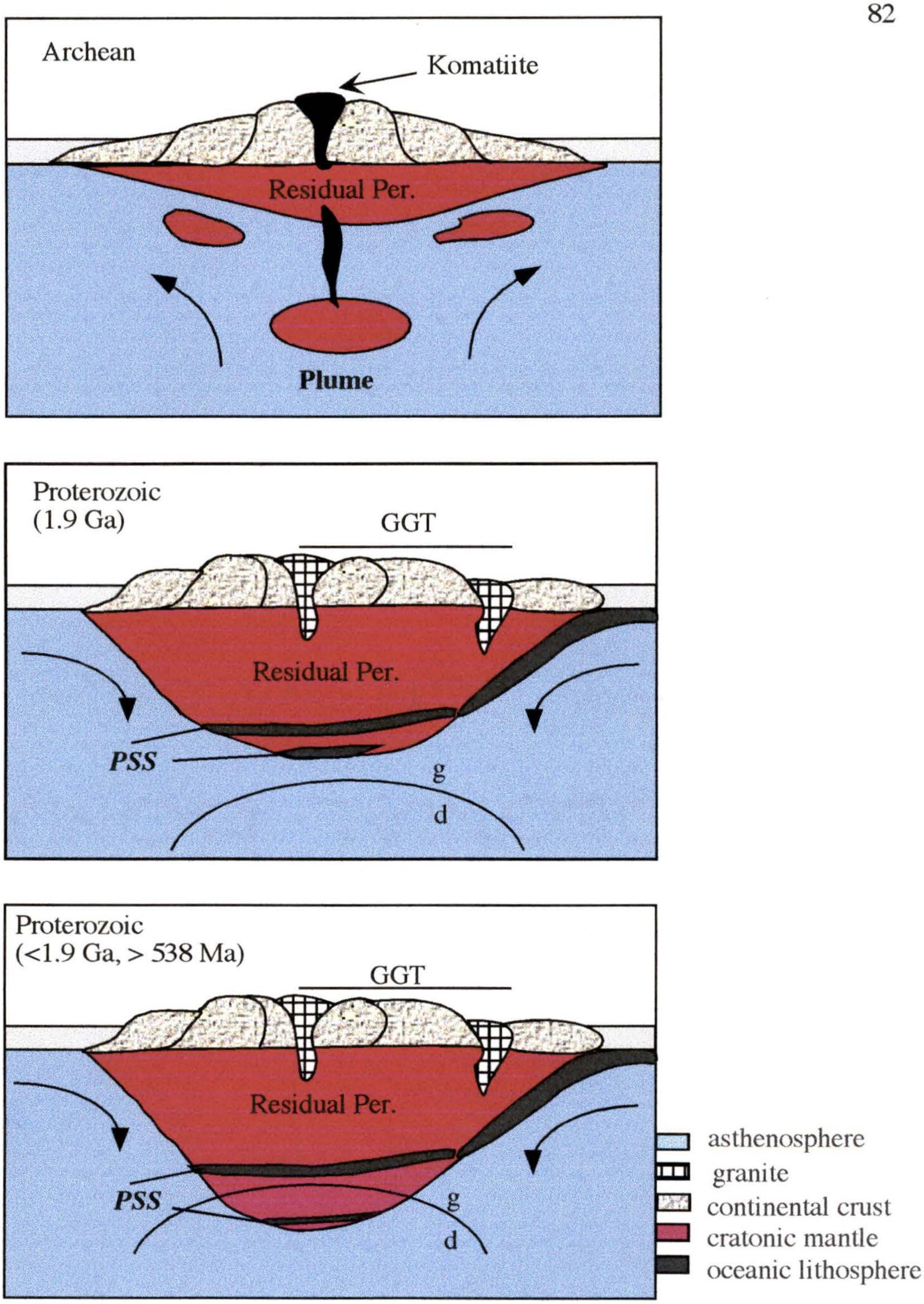

Figure 7.1: Schematic cross section depicting the tectonic development of the mantle beneath the central Slave craton. GGT=granite-greenstone terrain, g=graphite, d=diamond, ***PSS*** = previously subducted slabs.

present in some kimberlites from the Kaapvaal craton (Boyd at al., 1985) and eclogite xenoliths in some kimberlites from the Siberian craton (Pearson et al., 1995) indicate that these cratons had established deep, cool mantle roots by the end of the Archean. Thus, the time duration since the emergence of cool mantle roots, essential to stabilize diamond, may vary among cratons globally, but almost all cratons appear to have developed orthopyroxene-rich mantle lithosphere at some time during their history.

7.3 Future work

Presently, characterization of the mantle beneath the Slave craton is in its infancy due largely to the lack of samples. Ongoing diamond exploration has served to alleviate this and as more samples become available, the Slave mantle will become better characterized. Trace element geochemistry of the Torrie xenoliths may provide insights into the processes involved in their evolution. Isotopic dating of the Torrie suite is not feasible due to the small size of the samples but dating other xenoliths from the Slave craton and/or diamond inclusions would greatly expand our knowledge pertaining to the age of the mantle root beneath the Slave, an issue which is central to genetic models concerned with the formation and subsequent emergence of continental lithosphere. Isotopic dating of crustal and mantle xenoliths from the Torrie and other kimberlite-hosted xenoliths from the Slave province might also serve to constrain the timing and processes involved in the formation of the Slave crust.

REFERENCES

Abbott D. (1991). The case for accretion of the tectosphere by buoyant subduction, *Geophysical Research Letters* , v.**18**, n.**4**: 585-588.

Angel R. (1997). The Earth's mantle remodelled, *Nature* , **385**: 490-491.

Bostock M.G. (1997a). Anisotropic upper-mantle stratigraphy and architecture of the Slave craton, *Nature*, **390**: 392-395.

Bostock M.G. (1997b). Mantle stratigraphy and evolution of the Slave Province, *Journal of Geophysical Research*, submitted.

Bowring S.A., Housh T.B., Isachsen C.E. (1990). The Acasta gneiss: Remnant of Earth's early crust, In: Newsom H, Jones J (ed), *Origin of the Earth*, Lunar and Planetary Institute, Houston: 319-242.

Boyd F.R., Mertzman S.A. (1987). Composition and structure of the Kaapvaal lithosphere, southern Africa, In: Mysen BO (ed), *Magmatic processes: physiochemical principles*. Geochemical Society Special Publication 1, pp. 13-24.

Boyd F.R. (1989). Compositional distinction between oceanic and cratonic lithosphere, *Earth and Planetary Science Letters*, **96**: 15-26.

Boyd F.R. (1997). Correlation of orthopyroxene abundance with the Ni content of coexisting olivine in cratonic peridotites, *Transactions of the American Geophysical Union*, fall meeting abstract volume (1997): F746.

Boyd F.R., Pokhilenko N.P., Pearson D.G., Mertzman S.A., Sobolev N.V., Finger L.W. (1997). Composition of the Siberian cratonic mantle: evidence from Udachnaya peridotite xenoliths, *Contributions to Mineralogy and Petrology*, **128**: 228-246.

Boyd F.R., Canil D. (1997). Peridotite xenoliths from the Slave craton, Northwest Territories, In: Abstracts, *Seventh annual V.M. Goldschmidt Conference*, LPI contribution No. **921**, Lunar and Planetary Institute, Houston: 34-35.

Boyd F.R., Nixon P.H. (1978). Ultramafic nodules from the Kimberly pipes, South Africa, *Geochimica et Cosmochimica Acta*, **42**: 1367-1382.

Boyd F.R., Gurney J.J., Richardson S.H. (1985). Evidence for a 150-200-km thick Archean lithosphere from diamond incluson thermobarometry, *Nature* **315**: 387-389.

Boyd F.R. (1997). Recent Petrologic Developments in the Study of Cratonic Peridotites, In: Abstracts, Workshop on Continental Roots (Harvard/MIT 1997).

Brey G.P., Köhler T. (1990). Geothermobarometry in four-phase lherzolites II. New thermobarometers, and practical assessment of existing thermobarometers, *Journal of Petrology* , **31**: 1353-1378.

Canil D. (1990). Experimental study bearing on the absence of carbonate in mantle-derived xenoliths, *Geology* **18**: 1011-1013.

Canil D. (1991). Experimental evidence for the exsolution of cratonic peridotite from high-temperature harzburgite, *Earth and Planetary Science Letters*, **106**: 64-72.

Canil D., O'Neill H. (1996) Distribution of ferric iron in some upper-mantle assemblages, *Journal of Petrology*, **37**: 609-635.

Canil D., Fedourtchouk Y. (1998). Olivine-garnet reaction, garnet dissolution and the emplacement of kimberlites, submitted to *Earth and Planetary Science Letters* .

Chapman D.S. (1986). Thermal gradients in the continental crust, In The nature of the lower crust; Geological Society Special Publication No. **24**: 63-70.

Cook F.A., van der Velden A.J., Hall K.W., Roberts B.J. (1998). Tectonic delamination of the Precambrian lithosphere in northwestern Canada mapped by LITHOPROBE, In: Cook F. and Erdmer P.(compilers) Slave-Northern Cordillera Lithospheric Evolution (SNORCLE) transect and Cordillerian tectonics workshop meeting (Simon Fraser University 199), LITHOPROBE Report No. **64**: 54-69.

Cox K.G., Smith M.R., Beswetherick S. (1987). Textural studies of garnet lherzolites: evidence of exsolution origin from high-temperature harzburgites, In PH Nixon (Ed), *Mantle xenoliths*, Wiley, New York: 537- 550.

Dalton J.A., Lane S.J. (1996) Electron microprobe analysis of Ca in olivine close to grain boundaries: The problem of secondary X-ray fluoresence, *American Mineralogist* , **81**: 194-201.

Davis W.J., Kjarsgaard B.A. (1997) A Rb-Sr isochron age for a kimberlite from the recently discovered Lac de Gras field, Slave Province, Northwest Canada, *Journal of Geology* , **105**: 503-509.

DeWit M.J., Roering C., Hart R.J., Armonstrong R.A., de Ronde C.E.J., Green R.W.E., Tredoux M., Peberdy E., Hart R.A. (1992). Formation of an Archean continent, *Nature* , **357**: 553-562.

Eggler D.H., Dudas F.O., Hearn B.C., McCallum M.E., McGee E.S., Meyer H.O.A., Schulze D.J. (1987). Lithosphere of the continental United States: xenoliths in kimberlites and other alkaline magmas, In PH Nixon (Ed), *Mantle xenoliths*, Wiley, New York: 41-57.

Fipke C.E., Dummett H.T., Moore R.O., Carlson J.A., Ashley R.A., Gurney J.J., Kirkley M.B. (1995). History of the discovery of diamondiferous kimberlites in the Northwest Territories, Canada. *Sixth Int.Kimberlite Conf. (Novosibirsk) Extended Abstracts*:: 158-160.

Fung A.T., Haggerty S.E. (1995) Petrography and mineral compositions of eclogites from the Koidu Kimberlite complex, Sierra Leone, *Journal of Geophysical Research* , **100**: 20451-20473.

Ganguly J., Singh R.N., Ramana D.V. (1995). Thermal perturbation during charnockitization and granulite facies metamorphism in southern India, *Journal of Metamorphic Geology* , **13**: 419-430.

Grotzinger J., Royden L. (1990). Elastic strength of the Slave craton at 1.9 Gyr and implications for the thermal evolution of the continents, *Nature* **347**: 64-66.

Grand S.P. (1987). Tomographic inversion for shear velocity beneath the North American plate, *Journal of Geophysical Research* , **92**: 14065-14090.

Gurney J.J. (1984). A correlation between garnets and diamonds in kimberlites, In: Kimberlites, Occurrences and Origin, (University of Western Australia, **8**): 143-166.

Harley S.L. (1984). An experimental study of the partitioning of Fe and Mg between garnet and orthopyroxene, *Contributions to Mineralogy and Petrology* , **86**: 359-373.

Hart R.J., Tredoux M., deWit M.J. (1997). Refractory trace elements in diamond inclusions: Further clues to the origins of ancient cratons, *Geology* , **25**, 12: 1143-1146.

Harte B. (1977). Rock nomenclature with particular relation to deformation and recrystallisation textures in olivine-bearing xenoliths, *Journal of Geology* , **85**: 279-288.

Heaman L.M., Kjarsgaard B., Creaser R.A., Cookenboo H.O., Kretschmar U. (1997) Multiple episodes of kimberlite magmatism in the Slave Province, North America, In: Cook F. and Erdmer (compilers) Slave-Northern Cordillera Lithospheric Evolution (SNORCLE) transect and Cordillerian tectonics workshop meeting (Univ. of Calgary 1997), LITHOPROBE Report No. **56**: 14-17.

Herzberg C. (1997). Formation of cratonic mantle as plume residues and cumulates. submitted to the Boyd Symposium, Oct. 1997.

Hoffman P.F. (1990) Old and young mantle roots, *Nature* , **347**: 19-20.

Isachsen C.E., Bowring S.A. (1994). Evolution of the Slave craton, *Geology* **22**: 917-920.

Jones A.G., Ferguson I.J. (1997). Results from 1996 MT studies along SNORCLE profiles 1 and 1A, In: Cook F and Erdmer P.(compilers) Slave-Northern Cordillera Lithospheric Evolution (SNORCLE) transect and Cordillerian tectonics workshop meeting (Univ. of Calgary 1997), LITHOPROBE Report No. **56**: 42-47.

Kearey P., Vine F.J. (1990). *Global tectonics*, Blackwell Scientific Publication, Oxford University Press, Ontario, copyright 1990.

Kelemen P.B., Bernstein S., Hart S.R. (1997). SiO_2 addition to cratonic mantle via melt/rock reaction above subduction zones, In: Abstracts, Workshop on Continental Roots (Harvard/MIT 1997).

Kennedy S.C., Kennedy G.C. (1976). The equilibrium boundary boundary between graphite and diamond, *Journal of Geophysical Research* , **81**: 2467-2470.

Kjarsgaard B.A., Peterson T.D. (1992). Kimberlite-derived ultramafic xenoliths from the diamond stability field: a new Cretaceous geotherm for Somerset Island, Northwest Territories, In Current Research Part B; GSC paper **92-1B**: 1-6.

Köhler T., Brey G.P. (1990). Calcium exchange between olivine and clinopyroxene calibrated as a geothermobarometer for natural peridotites from 2-60 kb with applications, *Geochimica et Cosmochimica Acta* , **54**: 2375-2388.

Kopylova M.G., Russell J.K., Cookenboo H. (1998). Upper-mantle stratigraphy of the Slave craton, Canada: Insights into a new kimberlite province, *Geology* , **26**, 4: 315-318.

Krogh E.J. (1988). The garnet-clinopyroxene Fe-Mg geothermometer- a reinterpretation of existing experimental data, *Contributions to Mineralogy and Petrology,* **99**: 44-48.

Lewis T.J., Wang K. (1992). Influence of terrain on bedrock temperatures, *Palaeogeography, Palaeoclimatology, Palaeoecology* , **98**: 87-100.

MacGregor I.D. (1974). The system MgO-Al_2O_3-SiO_2: solubility of Al_2O_3 in enstatite for spinel and garnet peridotite compositions, *American Mineralogist* , **59**: 110-119.

Mitchell R.H. (1995). Kimberlites, Orangites, and Related rocks, Plenum Press, New York ©1995.

Nassichuk W.W., McIntyre D.J. (1995). Cretaceous and Tertiary fossils discovered in kimberlites at Lac de Gras in the Slave Province, Northwest Territories, In Current Research **1995-B**; GSC: 109-114.

Nickel K.G., Green D.H. (1985). Empirical geothermobarometry for garnet peridotites and implications for the nature of the lithosphere, kimberlites and diamonds, *Earth and Planetary Science Letters*, **73**: 158-170.

Nixon P.H., Davies G.R. (1987). Mantle xenolith perspectives, In PH Nixon (Ed), *Mantle xenoliths*, Wiley, New York: 741-756.

Nyblade A.A., Pollack H.N. (1993). A global analysis of heat flow from Precambrian terrains: implications for the thermal structure of Archean and Proterozoic lithosphere, *Journal of Geophysical research*, **98**: 12207-12218.

O'Neill H.C., Wood B.J. (1979) An experimental study of Fe-Mg partitioning between garnet and olivine and its calibration as a geothermometer, *Contributions to Mineralogy and Petrology* , **70**: 59-70.

Padgham W.A., Fyson W.K. (1992). The Slave province: a distinct Archean craton, *Canadian Journal of Earth Sciences*, **29**: 2072-2086.

Pearson D.G., Snyder G.A., Shirey S.B., Taylor L.A., Carlson R.W., Sobolev N.V. (1995). Archaean Re-Os age for Siberian eclogites and constraints on Archaean tectonics, *Nature* , **26**: 711-713.

Pell J.A. (1997). Kimberlites in the Slave craton, Northwest Territories, Canada, *Geoscience Canada*, **24**: 77-90.

Pinet C., Jaupart C., Mareschal J.C., Gariepy C., Bienfait G., Lapointe R. (1991). Heat flow and structure of the lithosphere in the Eastern Canadian Shield, *Journal of Geophysical Research*, **96**: 19941-19963.

Pollack H.N. (1986). Cratonization and thermal evolution of the mantle, *Earth and Planetary Science Letters*, **80**: 175-182.

Pollack H.N., Chapmen D.S. (1977). On the regional variation of heat flow, geotherms and lithospheric thickness, *Tectonophysics*, **38**: 279-296.

Reid A.M., Dawson J.B. (1972). Olivine-garnet reaction in peridotites from Tanzania, *Lithos*, **5**: 115-124.

Richardson S.H., Erlank A.J., Harris J.W., Hart S.R. (1990) Eclogitic diamonds of Proterozoic age from Cretaceous kimberlites, *Nature* , **346**: 54-56.

Ringwood A.E. (1991). Phase transformations and their bearing on the constitution and dynamics of the mantle, *Geochimica et Cosomochimica Acta*, **55**: 2083-2110.

Rudnick R.L., Presper T. (1990). Geochemistry of intermediate/- to high pressure granulites, In: Vielzeuf D. And Vidal Ph. (eds) *Granulites and Crustal Evolution* : 523-550.

Rudnick R.L., McDonough W.F., Orpin A. (1994). Northern Tanzanian peridotite xenoliths: a comparison with Kaapvaal peridotites and inferences on metasomatic interactions, In: HOA Meyer and OH Leonardos (eds):*Kimberlites, Related Rocks, and Mantle Xenoliths*. Proceedings of the Fifth International Kimberlite Conference, I, CPRM Special Publication 1A, Brazilia: 336-353.

Rudnick R.L., McDonough W.F., O'Connell R.J.(1998). Thermal Structure, thickness, and composition of continental lithosphere, *Chemical Geology* , **145**: 395-411.

Schmidberger S.S., Francis D. (1998). Nature of the mantle roots beneath the North American craton: mantle xenolith evidence from Somerset Island kimberlites, (submitted to *Lithos*).

Schatz J.F., Simmons G. (1972) Thermal Conductivity of Earth Materials at High Temperatures, *Journal of Geophysical Research*, **77**, 35: 6966-6983.

Smith D., Barron B.R. (1991). Pyroxene-garnet equilibration during cooling in the mantle,*American Mineralogist* , **76**: 1950-1963.

Sobolev N.V., Lavrent'yev, Yu G., Pokhilenko N.P., Usova L.V. (1973). Chrome-rich garnets from the kimberlites of Yakutia and their paragenesis, *Contributions to Mineralogy and Petrology* , **40**: 39-52.

Solomon M. (1963). Counting and Sampling Errors in Modal Analysis by Point Counter, *Journal of Petrology* , **l4**: 367-382.

Stiefenhofer J., Viljoen K.S., Marsh J.S. (1997). Petrography and geochemistry of peridotite xenoliths from the Lethlakane kimberlites, Botswana, *Contributions to Mineralogy and Petrology* , **127**: 147-158.

Thompson P.H., Judge A.S., Lewis T.J. (1995). Thermal parameters in rock units of the Winter Lake- Lac de Gras area, central Slave Province, Northwest Territories- implications for diamond genesis, In: Current Research **1995-E**; Geological Survey of Canada: 125-135.

Thompson P.H., Judge A.S., Charbonneau B.W., Carson J.M., Thomas M.D. (1996) Thermal regimes and diamond stability in the Archean Slave Province, northwestern Canadian shield, District of MacKenzie, Northwest Territories. In: Current Research **1996-E**; Geological Survey of Canada: 135-146.

Thompson P.H., Judge A.S., Lewis T.J. (1996) Thermal evolution of the lithosphere in the central Slave Province: Implications for diamond genesis. In Searching for diamonds in Canada, A.N. LeCheminant, D.G. Richardson, R.N.L. DiLabio, K.A. Richardson (ed.); Geological Survey of Canada, Open File **3228**: 151-160.

Walter M.J. (1998). Melting of Garnet Peridotite and the Origin of Komatiite and Depleted Lithosphere, *Journal of Petrology* , **39**: 29-60.

Wood B.J., Fraser D.G. (1977). *Elementary thermodynamics for geologists*, Oxford University Press © 1977.

APPENDIX 1

XENOLITH PETROGRAPHY

TQY94-17-22B1 (Gt lherzolite)

mineralogy	approx. mode (vol %)	colour	grain size (mm)
ol	80	pale pink/green	1.4
opx	14	colourless	0.3-1.3
cpx	3	pale green/pink	0.2-0.5
gt	3	colourless	1

Comments: heavily fractured,subhedral grains of garnet and pyroxene present as inclusions in macrocrystic olivine; *coarse-equant* .

TQY94-17-22B2 (Sp lherzolite)

mineralogy	approx. mode (vol %)	colour	grain size (mm)
ol	45	colourless	0.2-0.5
opx	25	colourless	0.1-0.7
cpx	25	pale yellow/green	0.3-1.4
spin	5	maroon	0.1-0.4

Comments: entire xenolith is 4 mm and very fresh; *granuloblastic,* inequigranular.

TQY94-17-22F (Sp lherzolite)

mineralogy	mode (wt %)	colour	grain size (mm)
ol	44	pale yellow/pink	0.2->4
opx	47	colourless	0.2->4
cpx	5	pale yellow/green	0.1-0.5
spinel	2	maroon	0.15

Comments: heavily fractured, serpentinized with minor interstitial carbonate (~34 % alteration); *coarse*, inequigranular.

TQY94-17-15(A) (Gt lherzolite)

mineralogy	mode (wt %)	colour	grain size (mm)
ol	51	colourless	0.2-1.2
opx	35	colourless	0.4-3.5
cpx	6	pale green/pink	0.7-1
gt	3	colourless	0.1-0.6

Comments: ~0.4 mm kelyphite rims surrounding gt, ol neoblasts present adjacent to both opx and ol, some euhedral ol, alteration (~ 26 %); *mosaic porphyroclastic,* inequigranular.

TANQ93-1-39 (Gt lherzolite)

mineralogy	mode (wt %)	colour	grain size (mm)
ol	68	colourless	0.2->4
opx	14	colourless	0.2-1.3
cpx	13	colourless	0.5
gt	2	colourless	0.5-1.3

Comments: ~ 22% alteration, ol neoblasts and phlog present along some fractures and interstitially, <0.1 mm kelyphite rims developed surrounding garnets; *coarse-equant*..

TANQ93-1-13 (Gt lherzolite)

mineralogy	mode (wt %)	colour	grain size (mm)
ol	73	colourless	0.1->4
opx	19	colourless	0.4-1.3
cpx	3	pale yellow/green	1.2
gt	4	colourless	0.5-1.4

Comments: minor ol neoblasts present interstially, gts are heavily fractured and altered (along fractures and interstitially, ~40 % alteration), ol and phlog inclusions in gt; *coarse-equant* .

TANQ93-2-35A (Ol websterite)

mineralogy	mode (wt %)	colour	grain size (mm)
ol	26	colourless	0.1-0.9
opx	66	colourless	0.1-0.8
cpx	8	colourless	<0.6
spin	<1	maroon	0.3

Comments: serpentinized (~ 68 %), minor phlog occurring along ol edges; inequigranular, *granuloblastic.*

TQ9513B (Gt lherzolite)

mineralogy	mode (wt %)	colour	grain size (mm)
ol	54	colourless	0.1-1.3
opx	35	colourless	0.8-3
cpx	6	very pale green	0.4-1
gt	3	colourless	1.4-2.6

Comments: 4 mm kelyphite rim developed on gt where in contact with the host kimberlite, undulose extinction in porphyroblasts. <0.3 mm neoblasts of ol and opx, (~19 % atleration); *porphyroblastic.*

X9501A (Gt harzburgite)

mineralogy	mode (wt %)	colour	grain size (mm)
ol	41	colourless	0.4-2
opx	47	colourless	0.2-1.2
gt	11	colourless	1-2

Comments: extensive deformed kelyphite rims on gt, serpentinized, carbonate present interstitially (total alteration ~ 64 %); inequigranular, *granuloblastic.*

X9501B(Gt harzburgite)

mineralogy	mode (wt %)	colour	grain size (mm)
ol	10	colourless	1
opx	56	colourless	0.6-2.2
cpx	<1	colourless	0.2-0.4
gt	34	colourless	1-4

Comments: extensive kelyphite rims grade into fine grained phlog and serp, (total alteration ~ 56 %) , minor interstitial carbonate also present interstitially; inequigranular, *coarse.*

TANQ93-2-44B (Ol websterite)

mineralogy	mode (wt %)	colour	grain size (mm)
ol	29	colourless	0.2-2
opx	41	colourless	0.4-0.6
cpx	15	colourless	0.15-1.8
spin	15	brown	0.2-0.5

Comments: ~ 75 % alteration, inequigranular, *granuloblastic.*

*The following samples were mounted in 25 mm epoxy plugs which are optically non-transparent thus quantitative petrography was not attainable using a petrographic microscope so the following descriptions were done in reflected light:

TANQ93-2-45 (Sp lherzolite)
mineralogy: ol, opx, cpx, spin
Comments: sample is heavily serpentinized (~65 %), grains are heavily fractured and range from <1-5 mm, phlog present, *granuloblastic.*

TANQ93-2-45A (Gt macrocryst)
mineralogy: ol, opx, cpx, gt
Comments: sample is a 1 cm gt macrocryst with inclusions of opx, cpx and ol, alteration present along fractures throughout the sample, secondary opx observed mantling cpx inclusion on scanning electron microprobe, pentlandite and Ni-pyrite also present.

TQY94-17-11 (Gt harzburgite)
mineralogy: ol, opx, gt
Comments: sample is ~1.6 cm, kelyphite rims surrounding gts, fractured with alteration along fractures, *granuloblastic,* pyrite and millerite also present.

APPENDIX 2

MINERAL CHEMISTRY

()= 2σ CaO in olivine analysis
*= Fe^{3+} in spinel calculated assuming stoichiometry

TQ9513B

	ol core	ol rim	opx core	opx rim	cpx core	cpx rim	gt core	gt rim
Na_2O	b.d.	b.d.	0.11	0.12	0.91	0.93	0.02	0.02
MgO	49.77	49.82	34.89	34.85	18.97	18.96	20.26	20.33
Al_2O_3	b.d.	b.d.	0.63	0.64	1.16	1.18	18.93	19.36
SiO_2	40.52	40.30	57.31	57.09	54.37	54.40	41.09	41.44
K_2O	b.d.	b.d.	b.d.	b.d.	0.06	0.06	b.d.	b.d.
CaO	0.05	0.07	0.90	0.92	19.56	19.51	5.63	5.46
TiO_2	b.d.	b.d.	0.03	0.03	0.06	0.05	0.19	0.21
Cr_2O_3	0.03	0.08	0.27	0.26	0.87	0.84	5.49	5.02
MnO	0.10	0.10	0.12	0.12	0.10	0.10	0.31	0.28
FeO	9.23	9.14	5.47	5.46	3.08	3.06	7.78	7.75
NiO	0.38	0.45	0.14	0.14	0.08	0.07	0.02	0.02
Total	100.14	100.04	99.90	99.67	99.23	99.19	99.79	99.93
Na	-	-	.008	.008	.064	.065	.003	.003
Mg	1.815	1.820	1.793	1.796	1.029	1.029	2.188	2.185
Al	-	-	.025	.026	.050	.051	1.617	1.646
Si	.991	.988	1.976	1.973	1.979	1.980	2.977	2.989
K	-	-	-	-	.003	.003	-	-
Ca	.001	.002	.033	.034	.763	.761	.437	.422
Ti	-	-	.001	.001	.002	.001	.010	.011
Cr	.001	.002	.007	.007	.025	.024	.315	.286
Mn	.002	.002	.004	.003	.003	.003	.019	.017
Fe	.189	.187	.158	.158	.094	.093	.471	.467
Ni	.008	.009	.004	.004	.002	.002	.001	.001
Fe^{3+}	-	-	-	-	-	-	-	-
Total	**3.008**	**3.011**	**4.010**	**4.012**	**4.014**	**4.013**	**8.043**	**8.032**
Mg#	.906	.907	.919	.919	.917	.917	.823	.824

b.d. - below detection limit.

	X9501A					X9501B		
	ol	opx	gt	serpentine	calcite	ol	opx	gt
Na_2O	0.02	0.12	0.03	0.11	b.d.	b.d.	0.11	b.d.
MgO	52.34	36.99	23.04	29.13	1.28	50.04	36.01	21.93
Al_2O_3	0.01	0.53	20.81	2.01	b.d.	b.d.	0.56	20.91
SiO_2	40.73	58.14	41.73	47.97	0.05	41.80	58.67	41.49
K_2O	b.d.	b.d.	b.d.	0.13	b.d.	b.d.	b.d.	b.d.
CaO	b.d.	0.24	3.08	0.62	59.46	0.03	0.23	2.97
TiO_2	b.d.	b.d.	b.d.	0.17	b.d.	b.d.	b.d.	b.d.
Cr_2O_3	0.04	0.28	4.66	0.23	b.d.	b.d.	0.32	4.50
MnO	0.10	0.11	0.34	0.06	1.68	b.d.	0.11	0.35
FeO	6.89	4.17	6.95	5.92	0.09	7.73	4.14	7.04
NiO	0.35	0.08	b.d.	0.15	b.d.	0.35	0.08	b.d.
Total	100.52	100.66	100.77	86.57	62.77	99.98	100.25	99.22
Na	0.001	0.008	0.004	0.006	-	-	0.007	-
Mg	1.883	1.872	2.427	1.161	0.085	1.808	1.826	2.344
Al	0.000	0.021	1.733	0.063	-	-	0.022	1.767
Si	0.983	1.974	2.949	1.283	0.002	1.013	1.996	2.974
K	-	-	-	0.004	-	-	-	-
Ca	-	0.009	0.233	0.018	2.826	0.001	0.008	0.228
Ti	-	-	-	0.003	-	-	-	-
Cr	0.001	0.008	0.260	0.005	-	-	0.009	0.255
Mn	0.002	0.003	0.020	0.001	0.063	-	0.003	0.021
Fe	0.139	0.118	0.411	0.132	0.003	0.157	0.118	0.422
Ni	0.007	0.002	-	0.003	-	0.007	0.002	-
Fe^{3+}	-	-	-	-	-	-	-	-
Total	**3.017**	**4.016**	**8.039**	**2.681**	**2.980**	**2.986**	**3.992**	**8.016**
Mg#	0.931	0.940	0.855	0.898	0.964	0.920	0.939	0.847

b.d. - below detection limit.

TQY94-17-22B1

	ol. core	ol rim	opx	cpx	gt core	gt rim
Na_2O	b.d.	b.d.	0.12	1.18	0.04	0.03
MgO	50.58	50.60	34.52	18.28	19.73	19.93
Al_2O_3	b.d.	b.d.	0.62	1.37	19.01	19.11
SiO_2	40.92	41.29	57.46	54.90	40.89	41.44
K_2O	b.d.	b.d.	b.d.	0.05	b.d.	b.d.
CaO	b.d.	b.d.	0.76	18.69	5.49	5.41
TiO_2	b.d.	b.d.	0.03	0.03	0.06	0.10
Cr_2O_3	b.d.	b.d.	0.28	1.16	6.04	5.78
MnO	0.10	0.08	0.10	0.07	0.31	0.34
FeO	7.39	7.44	5.08	2.81	6.92	6.83
NiO	0.42	0.44	0.15	0.02	b.d.	b.d.
Total	99.47	99.92	99.13	98.58	98.48	98.96
Na	-	-	0.008	0.084	0.005	0.004
Mg	1.840	1.831	1.782	0.994	2.152	2.158
Al	-	-	0.025	0.059	1.639	1.636
Si	0.999	1.003	1.990	2.002	2.992	3.011
K	-	-	-	0.002	-	-
Ca	-	-	0.028	0.730	0.430	0.421
Ti	-	-	0.001	0.001	0.003	0.005
Cr	-	-	0.008	0.034	0.349	0.332
Mn	0.002	0.002	0.003	0.002	0.019	0.021
Fe	0.151	0.151	0.147	0.086	0.423	0.415
Ni	0.008	0.009	0.004	0.001	-	-
Fe^{3+}	-	-	-	-	-	-
Total	**3.001**	**2.997**	**3.997**	**3.994**	**8.013**	**8.002**
Mg#	0.924	0.924	0.924	0.921	0.836	0.839

b.d. - below detection limit.

TQY94-17-22B2

	ol core	ol rim	opx core	opx rim	cpx core	cpx rim	sp core	sp rim
Na_2O	b.d.	b.d.	0.03	0.03	1.67	1.65	b.d.	b.d.
MgO	49.83	49.41	34.23	34.19	14.78	14.97	17.79	17.70
Al_2O_3	b.d.	b.d.	3.63	3.38	5.84	5.46	48.13	47.73
SiO_2	41.00	41.30	56.13	56.22	52.93	52.97	b.d.	b.d.
K_2O	b.d.	b.d.	b.d.	b.d.	b.d.	b.d.	b.d.	b.d.
CaO	0.032 (7)	0.03	0.28	0.30	20.40	20.79	b.d.	b.d.
TiO_2	b.d.	b.d.	0.08	0.10	0.32	0.34	0.20	0.56
Cr_2O_3	0.04	0.06	0.60	0.49	1.48	1.32	21.33	21.53
MnO	0.11	0.12	0.11	0.11	0.07	0.09	0.08	0.07
FeO	8.55	8.70	5.03	5.34	1.51	1.46	11.93	12.03
NiO	0.35	0.44	0.05	0.02	0.03	0.04	0.15	0.15
Total	99.97	100.12	100.17	100.17	99.02	99.10	99.63	99.78
Na	-	-	0.002	0.002	0.117	0.116	-	-
Mg	1.812	1.795	1.748	1.747	0.800	0.810	0.720	0.716
Al	-	-	0.147	0.136	0.250	0.234	1.539	1.526
Si	1.000	1.006	1.922	1.927	1.922	1.924	-	-
K	-	-	-	-	-	-	-	-
Ca	0.001	0.001	0.010	0.011	0.793	0.809	-	-
Ti	-	-	0.002	0.003	0.009	0.009	0.004	0.011
Cr	0.001	0.001	0.016	0.013	0.042	0.038	0.458	0.462
Mn	0.002	0.003	0.003	0.003	0.002	0.003	0.002	0.002
Fe	0.175	0.177	0.144	0.153	0.046	0.044	0.271	0.274
Ni	0.007	0.009	0.001	0.001	0.001	0.001	0.003	0.003
Fe^{3+}	-	-	-	-	-	-	*0.000	*0.000
Total	**2.999**	**2.993**	**3.995**	**3.996**	**3.982**	**3.989**	**2.997**	**2.994**
Mg#	0.912	0.910	0.924	0.919	0.946	0.948	0.727	0.724

b.d. - below detection limit.

TANQ93-2-45

	ol core	ol rim	opx core	opx rim	cpx core	cpx rim	sp
Na_2O	b.d.	b.d.	b.d.	b.d.	1.24	1.26	b.d.
MgO	50.86	51.37	35.07	35.18	16.70	16.90	17.24
Al_2O_3	b.d.	b.d.	2.25	2.04	3.28	3.27	35.79
SiO_2	41.36	41.17	57.35	57.46	54.43	54.65	0.03
K_2O	b.d.	b.d.	0.03	0.03	0.03	0.02	b.d.
CaO	b.d.	b.d.	0.25	0.28	21.62	21.77	b.d.
TiO_2	b.d.	b.d.	0.03	0.03	0.11	0.12	0.11
Cr_2O_3	0.03	0.05	0.38	0.33	1.18	1.16	30.31
MnO	0.08	0.08	0.12	0.11	0.07	0.07	0.23
FeO	6.51	6.07	4.65	4.71	1.27	1.25	13.42
NiO	0.34	0.36	b.d.	b.d.	b.d.	b.d.	0.08
Total	99.20	99.13	100.13	100.19	99.92	100.46	97.22
Na	-	-	-	-	0.087	0.087	-
Mg	1.845	1.863	1.785	1.790	0.896	0.903	0.752
Al	-	-	0.090	0.082	0.139	0.138	1.235
Si	1.006	1.001	1.958	1.962	1.960	1.958	0.001
K	-	-	0.001	0.001	0.001	0.001	-
Ca	-	-	0.009	0.010	0.834	0.836	-
Ti	-	-	0.001	0.001	0.003	0.003	0.002
Cr	0.001	0.001	0.010	0.009	0.033	0.033	0.702
Mn	0.002	0.002	0.004	0.003	0.002	0.002	0.006
Fe	0.132	0.124	0.133	0.134	0.038	0.038	0.264
Ni	0.007	0.007	-	-	-	-	0.002
Fe^{3+}	-	-	-	-	-	-	*0.000
Total	**2.993**	**2.998**	**3.992**	**3.993**	**3.995**	**3.998**	**3.028**
Mg#	0.933	0.938	0.931	0.930	0.959	0.960	0.696

b.d. - below detection limit.

TANQ93-2-45A

	ol	opx core	opx secondary	cpx core	cpx rim	gt core	gt rim	sp
Na_2O	b.d.	0.16	0.16	1.24	1.28	0.07	0.05	b.d.
MgO	47.55	33.66	33.56	16.88	17.38	16.40	16.60	13.30
Al_2O_3	b.d.	1.35	1.06	1.67	1.67	18.69	18.87	15.80
SiO_2	40.64	56.71	57.12	54.54	55.20	40.12	40.34	0.15
K_2O	b.d.	b.d.	b.d.	0.03	0.06	b.d.	b.d.	b.d.
CaO	0.13	1.25	1.07	20.93	20.33	8.47	8.38	b.d.
TiO_2	0.05	0.15	0.10	0.23	0.24	0.87	0.84	2.35
Cr_2O_3	0.05	0.76	0.67	0.91	0.98	4.45	4.37	41.74
MnO	0.11	0.14	0.13	0.10	0.10	0.41	0.41	0.38
FeO	10.88	6.00	5.81	3.11	3.15	9.78	9.78	22.95
NiO	0.18	0.09	b.d.	b.d.	b.d.	0.02	0.02	0.15
Total	99.61	100.26	99.68	99.68	100.40	99.31	99.68	96.82
Na	-	0.105	0.010	0.087	0.090	0.010	0.007	-
Mg	1.752	1.732	1.731	0.915	0.933	1.811	1.824	0.657
Al	-	0.055	0.043	0.072	0.071	1.631	1.639	0.617
Si	1.005	1.958	1.977	1.983	1.988	2.972	2.973	0.005
K	-	-	-	0.002	0.003	-	-	-
Ca	0.004	0.046	0.040	0.815	0.785	0.672	0.662	-
Ti	0.001	0.004	0.003	0.006	0.007	0.049	0.047	0.059
Cr	0.001	0.021	0.018	0.026	0.028	0.260	0.255	1.093
Mn	0.002	0.004	0.004	0.003	0.003	0.026	0.026	0.011
Fe	0.225	0.173	0.168	0.094	0.095	0.606	0.603	0.391
Ni	0.004	0.003	-	-	-	0.001	0.001	0.004
Fe^{3+}	-	-	-	-	-	-	-	*0.241
Total	**2.994**	**4.005**	**3.995**	**4.005**	**4.002**	**8.040**	**8.038**	**3.081**
Mg#	0.886	0.909	0.912	0.906	0.908	0.749	0.752	0.508

b.d. - below detection limit.

TQY94-17-11

	ol core	ol rim	opx core	opx rim	gt core	gt rim	sp
Na_2O	b.d.	b.d.	0.13	0.13	0.03	0.03	b.d.
MgO	50.92	50.81	36.00	36.15	19.76	19.77	14.35
Al_2O_3	b.d.	b.d.	0.50	0.53	18.89	19.08	10.22
SiO_2	41.46	41.27	58.85	58.97	40.85	40.96	0.22
K_2O	b.d.	b.d.	b.d.	b.d.	0.02	0.02	b.d.
CaO	b.d.	b.d.	0.31	0.32	5.39	5.38	b.d.
TiO_2	0.03	0.04	0.02	0.03	0.08	0.10	3.75
Cr_2O_3	0.03	0.03	0.31	0.31	6.50	6.52	45.53
MnO	0.08	0.08	0.12	0.11	0.42	0.40	0.42
FeO	7.32	7.33	4.51	4.53	7.28	7.27	22.92
NiO	0.34	0.34	b.d.	b.d.	0.02	0.02	0.18
Total	100.18	99.92	100.77	101.10	99.23	99.55	97.60
Na	-	-	0.009	0.009	0.004	0.004	-
Mg	1.836	1.837	1.819	1.821	2.147	2.140	0.718
Al	-	-	0.020	0.021	1.623	1.633	0.404
Si	1.003	1.001	1.995	1.993	2.977	2.975	0.007
K	-	-	-	-	0.001	0.002	-
Ca	-	-	0.011	0.012	0.421	0.419	-
Ti	0.000	0.001	0.000	0.001	0.005	0.005	0.095
Cr	0.001	0.000	0.008	0.008	0.375	0.374	1.208
Mn	0.002	0.002	0.003	0.003	0.026	0.025	0.012
Fe	0.148	0.149	0.128	0.128	0.443	0.442	0.333
Ni	0.007	0.007	-	-	0.001	0.001	0.005
Fe^{3+}	-	-	-	-	-	-	*0.307
Total	**2.996**	**2.998**	**3.995**	**3.996**	**8.022**	**8.019**	**3.092**
Mg#	0.925	0.925	0.934	0.934	0.829	0.829	0.528

b.d. - below detection limit.

TANQ93-1-13

	ol core	ol rim	opx core	opx rim	cpx core	cpx rim	gt core	gt rim
Na_2O	b.d.	b.d.	0.13	0.12	1.02	1.00	b.d.	b.d.
MgO	48.75	48.60	33.96	33.78	19.51	19.03	20.17	20.06
Al_2O_3	b.d.	0.04	0.62	0.66	1.39	1.11	19.68	19.69
SiO_2	40.86	40.88	58.12	58.02	55.04	54.86	42.20	42.30
K_2O	b.d.	b.d.	b.d.	b.d.	0.08	0.09	0.04	0.03
CaO	0.053(7)	0.09	0.81	0.84	18.89	19.72	5.24	5.31
TiO_2	b.d.	b.d.	0.04	0.04	0.13	0.17	0.43	0.42
Cr_2O_3	0.03	0.01	0.24	0.20	0.89	0.98	4.54	4.68
MnO	0.11	0.12	0.12	0.11	0.10	0.11	0.33	0.33
FeO	8.89	8.91	5.41	5.42	3.03	3.03	7.89	7.89
NiO	0.36	0.35	b.d.	b.d.	b.d.	b.d.	b.d.	b.d.
Total	99.10	99.01	99.46	99.21	100.08	100.11	100.55	100.75
Na	-	-	0.009	0.008	0.071	0.070	-	-
Mg	1.790	1.786	1.746	1.741	1.046	1.024	2.149	2.135
Al	-	0.001	0.025	0.027	0.059	0.047	1.658	1.656
Si	1.007	1.008	2.005	2.006	1.980	1.980	3.017	3.020
K	-	-	-	-	0.004	0.004	0.004	0.003
Ca	0.001	0.002	0.030	0.031	0.728	0.762	0.401	0.406
Ti	-	-	0.001	0.001	0.003	0.005	0.023	0.022
Cr	0.001	0.000	0.007	0.006	0.025	0.028	0.256	0.264
Mn	0.002	0.003	0.003	0.003	0.003	0.003	0.020	0.020
Fe	0.183	0.184	0.156	0.157	0.091	0.092	0.472	0.471
Ni	0.007	0.007	-	-	-	-	-	-
Fe^{3+}	-	-	-	-	-	-	-	-
Total	**2.992**	**2.991**	**3.983**	**3.981**	**4.012**	**4.015**	**8.006**	**8.002**
Mg#	0.907	0.907	0.918	0.917	0.920	0.918	0.820	0.819

b.d. - below detection limit.

TANQ93-1-39

	ol core	ol rim	opx core	opx rim	cpx core	cpx rim	gt core	gt rim
Na_2O	b.d.	b.d.	0.14	0.16	1.21	1.19	b.d.	b.d.
MgO	48.99	49.02	34.34	34.48	19.00	18.68	19.82	19.81
Al_2O_3	b.d.	b.d.	0.61	0.62	1.31	1.21	18.70	18.90
SiO_2	40.99	41.16	58.35	58.41	55.48	54.98	41.96	42.03
K_2O	b.d.	b.d.	0.02	0.02	0.06	0.06	0.02	0.02
CaO	0.046(7)	0.06	0.73	0.74	19.06	19.61	5.79	5.83
TiO_2	b.d.	b.d.	0.06	0.08	0.16	0.19	0.27	0.21
Cr_2O_3	0.04	0.05	0.27	0.27	0.98	1.15	6.20	6.09
MnO	0.11	0.11	0.11	0.12	0.10	0.11	0.33	0.33
FeO	8.62	8.57	5.27	5.31	2.90	2.92	7.46	7.39
NiO	0.40	0.39	b.d.	b.d.	b.d.	b.d.	0.01	0.01
Total	99.22	99.37	99.90	100.22	100.27	100.10	100.59	100.64
Na	-	-	0.009	0.011	0.084	0.083	-	-
Mg	1.795	1.792	1.757	1.760	1.017	1.004	2.122	2.118
Al	-	-	0.024	0.025	0.055	0.051	1.583	1.598
Si	1.007	1.009	2.003	2.000	1.992	1.983	3.014	3.015
K	-	-	0.001	0.001	0.003	0.003	0.002	0.002
Ca	0.001	0.002	0.027	0.027	0.733	0.758	0.446	0.448
Ti	-	-	0.002	0.002	0.004	0.005	0.014	0.011
Cr	0.001	0.001	0.007	0.007	0.028	0.033	0.352	0.345
Mn	0.002	0.002	0.003	0.004	0.003	0.003	0.020	0.020
Fe	0.177	0.176	0.151	0.152	0.087	0.088	0.448	0.443
Ni	0.008	0.008	-	-	-	-	0.001	0.001
Fe^{3+}	-	-	-	-	-	-	-	-
Total	**2.992**	**2.990**	**3.985**	**3.988**	**4.006**	**4.012**	**8.007**	**8.005**
Mg#	0.910	0.911	0.921	0.920	0.921	0.919	0.826	0.827

b.d. - below detection limit.

TQY94-17-15A

	ol core	ol rim	opx core	opx rim	cpx core	cpx rim	gt core	gt rim
Na_2O	b.d.	b.d.	0.17	0.17	1.14	0.87	0.05	0.05
MgO	49.51	49.44	33.77	33.82	20.55	18.63	20.32	20.33
Al_2O_3	0.04	0.04	0.76	0.79	1.48	1.50	17.80	17.84
SiO_2	41.13	41.09	58.39	58.48	56.15	55.10	42.15	42.14
K_2O	b.d.	b.d.	0.01	0.01	0.07	0.06	0.02	0.01
CaO	0.08(1)	0.08	1.10	1.10	17.09	20.09	5.61	5.57
TiO_2	0.17	b.d.	0.08	0.09	0.10	0.21	0.55	0.55
Cr_2O_3	0.07	0.06	0.36	0.35	1.13	1.31	6.13	5.98
MnO	0.10	0.11	0.12	0.12	0.10	0.10	0.28	0.27
FeO	8.33	8.30	5.01	5.03	3.30	2.89	7.22	7.26
NiO	0.37	0.37	b.d.	b.d.	b.d.	b.d.	0.04	0.04
Total	99.63	99.50	99.78	99.96	101.10	100.75	100.15	100.05
Na	-	-	0.012	0.011	0.078	0.060	0.006	0.006
Mg	1.801	1.804	1.729	1.729	1.085	0.995	2.182	2.185
Al	0.001	0.001	0.031	0.032	0.062	0.063	1.512	1.516
Si	1.004	1.006	2.006	2.005	1.990	1.975	3.038	3.039
K	-	-	0.001	0.001	0.003	0.003	0.002	0.001
Ca	0.002	0.002	0.041	0.040	0.649	0.772	0.433	0.431
Ti	0.003	0.000	0.002	0.002	0.003	0.006	0.030	0.030
Cr	0.001	0.001	0.010	0.009	0.032	0.037	0.349	0.341
Mn	0.002	0.002	0.003	0.004	0.003	0.003	0.017	0.017
Fe	0.170	0.170	0.144	0.144	0.098	0.087	0.435	0.438
Ni	0.007	0.007	-	-	-	-	0.002	0.002
Fe^{3+}	-	-	-	-	-	-	-	-
Total	**2.992**	**2.993**	**3.978**	**3.978**	**4.002**	**4.001**	**8.006**	**8.007**
Mg#	0.914	0.914	0.923	0.923	0.917	0.920	0.834	0.833

b.d. - below detection limit.

TQY94-17-22F

	ol core	ol rim	opx core	opx rim	cpx core	cpx rim	sp core	sp rim
Na_2O	b.d.	b.d.	0.06	0.03	1.00	1.00	b.d.	b.d.
MgO	50.97	50.97	34.86	35.21	16.50	16.45	16.78	17.06
Al_2O_3	b.d.	b.d.	3.03	2.92	3.45	3.43	40.04	40.50
SiO_2	41.13	41.14	56.40	56.59	53.39	53.68	0.03	0.05
K_2O	b.d.	b.d.	b.d.	b.d.	b.d.	0.02	b.d.	b.d.
CaO	b.d.	b.d.	0.73	0.33	22.56	22.60	0.04	0.06
TiO_2	b.d.	b.d.	b.d.	b.d.	0.03	0.03	0.03	0.03
Cr_2O_3	b.d.	b.d.	0.59	0.47	1.17	1.19	28.79	28.54
MnO	0.10	0.09	0.12	0.15	0.05	0.05	0.10	0.10
FeO	7.30	7.34	4.79	4.80	1.33	1.30	12.64	12.70
NiO	0.36	0.34	0.08	0.06	0.02	0.03	0.10	0.08
Total	99.90	99.91	100.66	100.60	99.51	99.78	98.56	99.12
Na	-	-	0.004	0.002	0.071	0.071	-	-
Mg	1.844	1.844	1.773	1.789	0.893	0.888	0.710	0.717
Al	-	-	0.122	0.117	0.148	0.146	1.340	1.346
Si	0.999	0.999	1.925	1.929	1.939	1.943	0.001	0.001
K	-	-	-	-	-	0.001	-	-
Ca	-	-	0.027	0.012	0.878	0.876	0.001	0.002
Ti	-	-	-	-	0.001	0.001	0.001	0.001
Cr	-	-	0.016	0.013	0.034	0.034	0.646	0.636
Mn	0.002	0.002	0.003	0.004	0.002	0.002	0.002	0.002
Fe	0.148	0.149	0.137	0.137	0.040	0.039	0.288	0.288
Ni	0.007	0.007	0.002	0.002	0.001	0.001	0.002	0.002
Fe^{3+}	-	-	-	-	-	-	*0.013	*0.013
Total	**3.001**	**3.001**	**4.008**	**4.006**	**4.005**	**4.001**	**3.005**	**3.007**
Mg#	0.926	0.925	0.928	0.929	0.957	0.958	0.703	0.705

b.d. - below detection limit.

TANQ93-2-35A

	ol core	ol rim	opx core	opx rim	cpx core	cpx rim
Na_2O	b.d.	b.d.	b.d.	0.02	0.89	0.82
MgO	50.99	50.93	35.70	35.66	16.96	16.96
Al_2O_3	b.d.	b.d.	1.96	1.74	2.50	2.41
SiO_2	40.37	40.06	56.90	57.32	53.95	53.42
K_2O	b.d.	b.d.	b.d.	b.d.	b.d.	b.d.
CaO	b.d.	b.d.	0.23	0.16	23.46	23.31
TiO_2	b.d.	b.d.	0.06	0.07	0.20	0.22
Cr_2O_3	b.d.	0.03	0.30	0.25	0.82	0.65
MnO	0.12	0.10	0.12	0.12	0.04	0.06
FeO	7.58	7.60	5.32	5.40	1.40	1.43
NiO	0.36	0.37	0.05	0.06	0.03	0.03
Total	99.46	99.11	100.64	100.79	100.26	99.31
Na	-	-	-	0.001	0.062	0.058
Mg	1.859	1.865	1.816	1.811	0.913	0.922
Al	-	-	0.079	0.070	0.106	0.103
Si	0.988	0.984	1.943	1.953	1.949	1.948
K	-	-	-	-	-	-
Ca	-	-	0.008	0.006	0.908	0.911
Ti	-	-	0.002	0.002	0.005	0.006
Cr	-	0.001	0.008	0.007	0.024	0.019
Mn	0.002	0.002	0.003	0.004	0.001	0.002
Fe	0.155	0.156	0.152	0.154	0.042	0.044
Ni	0.007	0.007	0.001	0.002	0.001	0.001
Fe^{3+}	-	-	-	-	-	-
Total	**3.012**	**3.015**	**4.013**	**4.008**	**4.012**	**4.014**
Mg#	0.923	0.923	0.923	0.922	0.956	0.955

b.d. - below detection limit.

TANQ93-2-44B

	ol core	ol rim	opx core	opx rim	cpx core	cpx rim	sp core	sp rim
Na_2O	b.d.	b.d.	0.03	0.02	1.35	1.24	b.d.	b.d.
MgO	51.02	51.31	34.90	35.42	15.70	16.29	20.25	20.61
Al_2O_3	b.d.	b.d.	3.48	3.00	5.06	3.94	55.81	56.14
SiO_2	40.41	40.38	56.45	56.22	53.07	53.70	b.d.	b.d.
K_2O	b.d.	b.d.	b.d.	b.d.	b.d.	b.d.	b.d.	b.d.
CaO	b.d.	b.d.	0.54	0.20	22.40	22.91	b.d.	b.d.
TiO_2	b.d.	b.d.	0.03	0.04	0.18	0.20	0.03	0.03
Cr_2O_3	b.d.	b.d.	0.31	0.28	0.84	0.67	13.52	13.60
MnO	0.11	0.11	0.14	0.14	0.07	0.07	0.07	0.05
FeO	7.86	7.87	5.20	5.31	1.15	1.14	9.98	9.88
NiO	0.34	0.32	0.07	0.06	0.05	0.02	0.22	0.18
Total	99.78	100.02	101.15	100.68	99.87	100.18	99.87	100.52
Na	-	-	0.002	0.001	0.094	0.087	-	-
Mg	1.856	1.863	1.767	1.802	0.845	0.875	0.786	0.795
Al	-	-	0.139	0.121	0.215	0.167	1.714	1.712
Si	0.986	0.984	1.918	1.919	1.917	1.935	-	-
K	-	-	-	-	-	-	-	-
Ca	-	-	0.019	0.007	0.867	0.885	-	-
Ti	-	-	0.001	0.001	0.005	0.005	0.001	0.001
Cr	-	-	0.008	0.008	0.024	0.019	0.278	0.278
Mn	0.002	0.002	0.004	0.004	0.002	0.002	0.001	0.001
Fe	0.160	0.160	0.148	0.151	0.035	0.034	0.211	0.210
Ni	0.007	0.006	0.002	0.002	0.001	0.001	0.005	0.004
Fe^{3+}	-	-	-	-	-	-	*0.005	*0.005
Total	**3.013**	**3.016**	**4.009**	**4.017**	**4.006**	**4.010**	**3.003**	**3.004**
Mg#	0.920	0.921	0.923	0.922	0.961	0.962	0.783	0.788

b.d. - below detection limit.

APPENDIX 3

CALCULATED P-T SOLUTIONS

Sample #	T-ONEILL	P-BKN	T-ONEILL	P-NG85	T-HARLEY	P-BKN	T-HARLEY	P-NG85
TQ9513B core	1135	5.0	1135	5.6	1051	4.4	1072	4.8
TQ9513B rim	1153	5.0	1155	5.1	1050	4.4	1068	4.7
TQY94-17-22B1 core	1178	5.2	1182	5.3	1071	4.5	1092	4.8
TQY94-17-22B1 rim	1178	5.1	1180	5.1	1047	4.2	1067	4.5
TANQ93-2-45A	908	3.3	919	3.5	775	2.3	814	3.0
TANQ93-1-13core	1172	5.2	1173	5.2	1053	4.4	1072	4.7
TANQ93-1-13rim	1178	5.1	1180	5.1	1047	4.2	1067	4.6
TANQ93-1-39core	1106	4.7	1117	4.9	990	3.9	1022	4.5
TANQ93-1-39rim	1131	4.9	1138	5.1	1033	4.3	1057	4.7
TQY94-17-15A core	1215	5.0	1224	5.3	1092	4.3	1122	4.8
TQY94-17-15A rim	1224	5.1	1232	5.3	1113	4.5	1142	4.9
TQY94-17-11core	873	3.9	907	4.2	883	3.5	923	4.3
TQY94-17-11rim	877	3.5	911	4.2	884	3.5	924	4.3
X9501A	911	3.8	950	4.4	935	3.9	972	4.5
X9501B	1065	4.8	1083	5.2	896	3.6	934	4.3
TQY94-17-22F core	0	0	0	0	0	0	0	0
TQY94-17-22F rim	0	0	0	0	0	0	0	0
TANQ93-2-35A core	0	0	0	0	0	0	0	0
TANQ93-2-35A rim	0	0	0	0	0	0	0	0
TANQ93-2-44B core	0	0	0	0	0	0	0	0
TANQ93-2-44B rim	0	0	0	0	0	0	0	0
TQY94-17-22B2 core	0	0	0	0	0	0	0	0
TQY94-17-22B2 rim	0	0	0	0	0	0	0	0
TANQ93-2-45core	0	0	0	0	0	0	0	0
TANQ93-2-45rim	0	0	0	0	0	0	0	0

Sample #	T-BKN	P-BKN	T-BKN	P-NG85	T-KROGH	P-BKN	T-KROGH	P-NG85
TQ9513B core	1233	5.7	1231	5.6	1152	5.1	1156	5.2
TQ9513B rim	1233	5.6	1231	5.5	1140	5.0	1143	5.1
TQY94-17-22B1 core	1215	5.4	1262	5.7	1159	5.0	1165	5.2
TQY94-17-22B1 rim	1232	4.6	1230	5.4	1174	5.0	1177	5.1
TANQ93-2-45A	1038	4.3	1032	4.0	1097	4.8	1073	4.2
TANQ93-1-13core	1261	5.8	1258	5.7	1148	5.0	1152	5.1
TANQ93-1-13rim	1232	5.4	1230	5.4	1174	5.0	1177	5.1
TANQ93-1-39core	1232	5.5	1231	5.5	1152	5.0	1159	5.1
TANQ93-1-39rim	1126	4.9	1129	5.0	1167	5.1	1171	5.2
TQY94-17-15A core	1354	5.9	1230	5.4	1256	5.3	1264	5.5
TQY94-17-15A rim	932	3.4	941	3.9	1170	4.8	1184	5.1
TQY94-17-11core	0	0	0	0	0	0	0	0
TQY94-17-11rim	0	0	0	0	0	0	0	0
X9501A	0	0	0	0	0	0	0	0
X9501B	0	0	0	0	0	0	0	0
TQY94-17-22F core	0	0	0	0	0	0	0	0
TQY94-17-22F rim	0	0	0	0	0	0	0	0
TANQ93-2-35A core	0	0	0	0	0	0	0	0
TANQ93-2-35A rim	0	0	0	0	0	0	0	0
TANQ93-2-44B core	0	0	0	0	0	0	0	0
TANQ93-2-44B rim	0	0	0	0	0	0	0	0
TQY94-17-22B2 core	0	0	0	0	0	0	0	0
TQY94-17-22B2 rim	0	0	0	0	0	0	0	0
TANQ93-2-45core	0	0	0	0	0	0	0	0
TANQ93-2-45rim	0	0	0	0	0	0	0	0

Sample #	T-BKN	P-KB	T-BKN	T-ONEILL	T-KROGH	T-HARLEY	T Ca in opx
TQ9513B core	1195	3.9	*1219*	*1135*	*1147*	*1086*	*1203*
TQ9513B rim	1228	5.3	*1220*	*1151*	*1141*	*1089*	
TQY94-17-22B1 core	1210	5.2	*1206*	*1171*	*1156*	*1102*	*1158*
TQY94-17-22B1 rim	1216	4.7	*1222*	*1175*	*1172*	*1095*	
TANQ93-2-45A	921	-1.9	*1052*	*985*	*1106*	*916*	*1258*
TANQ93-1-13core	1262	5.9	*1244*	*1163*	*1146*	*1089*	*1173*
TANQ93-1-13rim	1216	4.7	*1222*	*1175*	*1172*	*1095*	
TANQ93-1-39core	1238	5.8	*1221*	*1120*	*1153*	*1053*	*1145*
TANQ93-1-39rim	1100	3.5	*1129*	*1135*	*1161*	*1077*	
TQY94-17-15A core	1358	6.1	*1334*	*1213*	*1242*	*1135*	*1261*
TQY94-17-15A rim	864	-0.61	*959*	*1219*	*1179*	*1148*	
TQY94-17-11core	0	0	*0*	*945*	*0*	*964*	*951*
TQY94-17-11rim	0	0	*0*	*949*	*0*	*966*	
X9501A	0	0	*0*	*980*	*0*	*1001*	*905*
X9501B	0	0	*0*	*1074*	*0*	*973*	*896*
TQY94-17-22F core	865	6.0	***811***	***0***	***0***	***0***	***999***
TQY94-17-22F rim	857	5.2	***814***	***0***	***0***	***0***	
TANQ93-2-35A core	664	2.7	***656***	***0***	***0***	***0***	***775***
TANQ93-2-35A rim	670	2.4	***665***	***0***	***0***	***0***	
TANQ93-2-44B core	753	3.5	***734***	***0***	***0***	***0***	***930***
TANQ93-2-44B rim	665	3.2	***651***	***0***	***0***	***0***	
TQY94-17-22B2 core	991	3.0	***975***	***0***	***0***	***0***	***810***
TQY94-17-22B2 rim	923	2.1	***921***	***0***	***0***	***0***	
TANQ93-2-45core	1041	9.3	***932***	***0***	***0***	***0***	***788***
TANQ93-2-45rim	1024	8.6	***930***	***0***	***0***	***0***	

Sample #	P-BKN	P-NG85	P-KB
TQ9513B core	*4.1*	*4.41*	*.72*
TQ9513B rim	*4.0*	*4.3.2*	*1.8*
TQY94-17-22B1 core	*4.1*	*4.4*	*1.9*
TQY94-17-22B1 rim	*3.9*	*4.2*	*1.3*
TANQ93-2-45A	*4.0*	*3.9*	*-.83*
TANQ93-1-13core	*4.1*	*4.4*	*1.6*
TANQ93-1-13rim	*3.9*	*4.2*	*1.3*
TANQ93-1-39core	*40*	*4.4*	*2.1*
TANQ93-1-39rim	*4.1*	*4.4*	*2.3*
TQY94-17-15A core	*3.8*	*4.2*	*.13*
TQY94-17-15A rim	*3.8*	*4.3*	*.95*
TQY94-17-11core	*4.3*	*4.7*	*0*
TQY94-17-11rim	*4.3*	*4.6*	*0*
X9501A	*4.3*	*4.7*	*0*
X9501B	*4.4*	*4.7*	*0*
TQY94-17-22F core	***0***	***0***	***4.9***
TQY94-17-22F rim	***0***	***0***	***4.2***
TANQ93-2-35A core	***0***	***0***	***5.1***
TANQ93-2-35A rim	***0***	***0***	***4.6***
TANQ93-2-44B core	***0***	***0***	***4.3***
TANQ93-2-44B rim	***0***	***0***	***5.7***
TQY94-17-22B2 core	***0***	***0***	***.49***
TQY94-17-22B2 rim	***0***	***0***	***.48***
TANQ93-2-45core	***0***	***0***	***5.1***
TANQ93-2-45rim	***0***	***0***	***4.8***

italics = pressures and temperatures calculated at 1000°C and 5 GPa respectively

italics = pressures and temperatures calculated at 800°C and 2 GPa respectively

VITA

Surname: MacKenzie Given Names: Jason Millard

Place of Birth: Shelburne, Nova Scotia, Canada

Educational Institutions Attended:

University of Victoria	1996 to 1998
Acadia University	1991 to 1996

Degrees Awarded:

B.Sc.	Acadia University	1996

Publications:

MacKenzie J.M., Canil D. (1997). Petrologic Nature of the Lower Crust and Upper mantle Beneath the Archean Slave Province NWT, Canada. In: Cook F. and Erdmer (compilers) Slave-Northern Cordillera Lithospheric Evolution (SNORCLE) transect and Cordillerian tectonics workshop meeting (University of Calgary 1997), LITHOPROBE Report No. **56**: 223-224

Canil D. MacKenzie J.M. (1997). Lower crust and upper mantle beneath the Archean Slave craton, NWT: A view from xenolith studies, In: Abstracts; GAC/MAC annual meeting, Ottawa 1997: A-22

MacKenzie J.M., Canil D (1998). Composition and thermal evolution of the upper mantle beneath the Archean Slave Province: Evidence from xenolith studies, In: Cook F. and Erdmer (compilers) Slave-Northern Cordillera Lithospheric Evolution (SNORCLE) transect and Cordillerian tectonics workshop meeting (Simon Fraser University 1998), LITHOPROBE Report No. **64**: 37-38

MacKenzie J.M., Canil D (1998). Thermal state of the lower crust and upper mantle of the Archean Slave Province, NWT, Canada: A xenolith study, In: Abstracts, Workshop on Continental Roots (Harvard/MIT 1997)

MacKenzie J.M, Canil D (1998). Upper mantle xenoliths from the Archean Slave craton: Composition and thermal evolution of a kimberlite province. In: Abstracts; GAC/MAC annual meeting, Quebec City 1998: A-114

MacKenzie J.M, Canil D (1998). Composition and thermal evolution of cratonic mantle beneath the central Archean Slave Province, NWT, Canada, *Contributions to Mineralogy and Petrology* (in press)

PARTIAL COPYRIGHT LICENSE

Title of Thesis:

Cratonic Upper-mantle Beneath the Central Slave Province

Author: [redacted]

Jason Millard MacKenzie

December 18, 1998